UNIVERSITY OF OSLO
Department of Physics

Thesis for the degree
Master of Science:

Modeling the Onset of Dynamic Friction: Contact Mechanics

Kjetil Thøgersen

June 1, 2011

Acknowledgments

The master's thesis was written at the University of Oslo with supervision from Professor Anders Malthe-Sørenssen, Dr. Jan Ludvig Vinningland and Dr. Julien Scheibert finishing June 2011.

The first year of my master studies, I attended a computational physics seminar where Anders presented a possible thesis project in friction, a field I knew very little about, and I was a bit surprised to see that it was such a large field of research. The project was very interesting, and after a short meeting with Anders I was sold. The last year I have worked closely with my supervisors and two fellow master students David Skålid Amundsen and Jørgen Trømborg. I would like to thank them all for valuable advice and discussions. Julien moved to Lyon in February, but we kept in touch with weekly Skype meetings. Together with David and Jørgen I visited him at CNRS Lyon in March, where he showed us the lab and we held a short presentation of our work. We also attended a very interesting seminar by Dr. Jay Fineberg. His experiments are part of what I have made numerical models for in this thesis. They also helped me verifying my code using a commercial finite element solver. A special thank you to Julien for his hospitality.

My parents and my three brothers have been a huge support for me, and have motivated me to work hard through my studies. So has my closest friends Kim, Kennet and Thomas. I could not have done this without you. I would especially like to thank Kim for spell-checking my thesis.

At last, I thank my wonderful girlfriend, Linn, for being who she is, and for reminding me that life is more than just work.

Abstract

A one-dimensional mesoscopic spring block model with Amontons-Coulomb friction is introduced in order to investigate if some features of recent friction experiments can be understood. Our results suggest that the model too simple to reproduce the main features of the experiment. A two dimensional model and a different local friction law is needed.

In order to test the latter, a two dimensional quasi-static discrete element method is developed to find the tangential loading curve of a thin surface layer. A single asperity is modeled as a semi-circle, in agreement with Hertz and Cattaneo-Mindlin theory. A scaling behavior of the shear stiffness of an asperity with the compression and the dynamic friction coefficient is found, and used to develop a theoretical model for the shear strength of a rough surface assuming elastic independence of asperities.

The discrete element method is further used to model a self affine surface and a gradient percolation surface. Our results suggest that the qualitative behavior of the shear stiffness for the self affine surface is in agreement with the theory, while the behavior of the gradient percolation surface is not.

Contents

List of symbols

β	Exponent relation compression and normal load	83
χ	Characteristic slip length	45
Δt	Time step	27
δ	Surface compression	63
δ_i	Local compression	101
ϵ_n	Unit elongation along n	53
η	Viscous damping	25
Γ	Asymmetry	92
$\gamma_{n_2 n_2}$	Shear strain along the plane n_1, n_2	53
κ	Wave number	26
λ	Wave length	26
μ_k	Dynamic friction coefficient	61
μ_s	Static friction coefficient	24
ν	Poisson's ratio	54
ω	Angular frequency	26
Φ	Elastic energy density	68
Ψ	Stress function	56
ρ	Density	77
σ_n	Normal stress parallel to n	53
τ_n	Shear stress along dimension n	53
Υ	Probability distribution	64
ε	Termination criterion	75
$\varepsilon_{\text{surf}}$	Surface termination criterion	78
ϱ	Over relaxation parameter	74
ζ	Magnification	64
A	Apparent area of contact	63
a	Real area of contact	60
a_0	Lattice spacing	24
c	Stick zone area	61
c_0	Stick region center	92
$C_2(x)$	Height correlation function	109
D	Fractal dimension	117
d	Spring equilibrium length	23
E	Young's modulus	54
E^*	Effective Young's modulus	60
f	Local force	25
f_k	Dynamic friction force	25
f_s	Static friction force	25

F_x	Force parallel to $\vec{x}$	25
G	Shear modulus	54
g	Dimensionless torque parameter	24
H	Hurst exponent	63
K	Driving spring constant	23
k	Material spring constant	23
k_{pot}	Potential surface strength	74
L	System length	23
l	Characteristic asperity size	101
M	Total mass	23
m	Local mass	23
N	Number of nodes	23
n	Number of neighbor blocks	25
P	Normal load	57
$p(x)$	Normal pressure distribution	59
Q	Tangential load	58
$q(x)$	Tangential traction distribution	59
R	Radius	59
S	Cross-sectional area	24
T	Torque	33
t	Time	25
u_n	Elongation along n	53
U_{el}	Elastic energy	63
v	Velocity	25
w_i	Local normal force	24

Part I

INTRODUCTION

Chapter 1

Introduction

Studies of friction have numerous applications ranging from cross-country skiing to earthquake prediction. At first glance it might seem that friction is easily explainable, but many aspects are not fully understood. Many of the difficulties arise due to the multiscale nature of friction, that ranges from elecromagnetic interactions to macroscopic behaviour of e.g. earthquakes. This is a huge challenge when developing models to understand the large-scale behavior of friction phenomena. It is difficult to model macroscopic systems at the atomic scale, and some sort of assumption at the mesoscale often has to be made in a macroscopic model. These assumptions arise from microscopic experiments and models. Many questions as to how this gap can be bridged are still unanswered.

Friction is of great importance to industry. It has been estimated that 6% of the gross national product in the USA is lost due to ignorance of friction phenomena such as fretting, wear, lubrication and air resistance [1]. These are all cases where energy is lost because the friction coefficient is higher than desired. In other cases a high friction coefficient is wanted. When driving a car, the friction between the tires and the road should be large, and the friction in the brake pads should be as large as possible with the wear remaining small.

In addition to industrial applications, friction is an important mechanism in geological processes. The most important one is perhaps the prediction of earthquakes, that are governed by stick slip behaviour [2]. Friction phenomena and stress profiles are believed to be largely important in order to determine when a quake is triggered and how large it will be. The behavior of earthquakes is believed to be chaotic, and it remains to be seen if there exists some information that can be used to make predictions. A different geological application where friction is an important part is the triggering of avalanches and landslides.

Friction is an open frontier with many unanswered questions. Among them are:

- Can predictions of earthquakes be made? And if yes, how accurate will these predictions be?
- How is friction related to wear processes?
- How can the microscale be related effectively to the mesoscopic and macroscopic scales?

- Can we tune the friction characteristics of materials?

Technological developement has given rise to fundamental studies of friction the last few years. New experimental techniques as well as numerical models have been developed.

1.1 The focus of this thesis

In this thesis, a numerical model will be used to investigate some of the aspects of the recent experiments. I will further focus on the properties of a thin surface layer using two different numerical models. Throughout the thesis, dry friction and purely elastic materials are used. One should note that effects like different friction laws, plasticity and temperature may be important. These effects are neglected in this study. This will prevent complicating the numerical models developed, and will make it easier to analyze the results. Implementing some of these effects is a possible future project.

In order to investigate some of the physical effects that are important to the transition from dynamic to static friction, a mesoscopic one-dimensional friction model is introduced. Prior to the slip of an object, which is called the global event, there are smaller slip events that do not propagate all the way through the material. These events are named precursors. We investigate what governs the behavior of the precursors with a one-dimensional spring block model with a simple Amontons-Coulomb friction law. This is a mesoscopic model, where the microscopic effects are implemented in the friction law. Some of the questions I wish to answer are:

- Can a simple one-dimensional mesoscopic spring block model reproduce recent experimental results?
- Can analytical predictions be made?

The insight from the mesoscopic model is used to develop a two-dimensional microscopic quasi-static discrete element method. This model is used to find the normal and shear stiffness of a single asperity in two dimensions. A theory for the behavior of a rough surface consisting of multiple asperities with a given height distribution is developed, and tested with numerical simulations for two types of surfaces. Some of the questions I wish to answer with the microscopic model are:

- What is the general behavior of the surface layer?
- How does the surface layer affect the local friction law?
- Can analytical predictions for the shear stiffness of a surface layer be made?

1.2 History of friction

To motivate our friction studies, we start with ancient history of friction, and give a introduction to the topics that have been discussed in the last few years. The main source of this section is 'History of Tribology' by Dowson [3]. The history of friction dates back to ancient times. More than 4000 years ago, the Egyptians used lubrication in order to reduce the friction when moving large objects. A painting dated to around 1880 BC found in a grotto in El-Bershed (figure (1.1)), shows the moving of the colossus. One

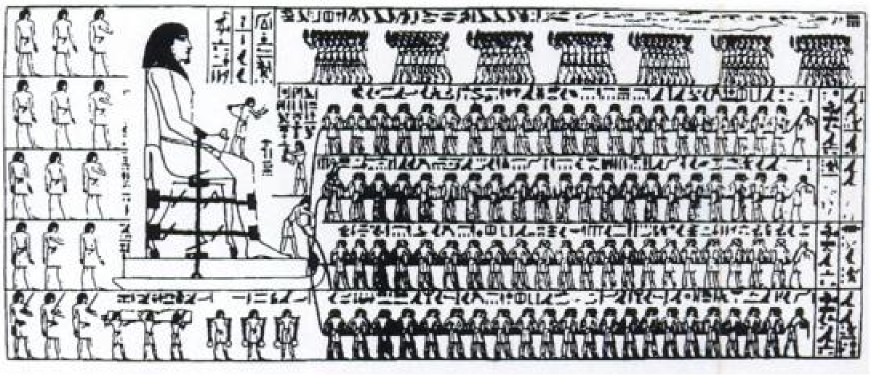

Figure 1.1: *A painting dated to around 1880 BC found in a grotto in El-Bershed. The figure is taken from [3]*

can clearly see an officer pouring lubricants directly in front of the sledge that carries the colossus. From this picture one can actually estimate the friction coefficient. If the weight of the colossus is approximately 60 tons, and each person pulls with a force of 800 Newtons (There are 172 men in the picture), the friction coefficient is $\mu = 0.23$. The value of the friction coefficient suggests that the colossus was sliding on lubricated wood.

1.2.1 The laws of dry friction

The first recorded experiments on friction, were done by Leonardo da Vinci (1452 - 1519). He found out that the friction was proportional to the normal load, and did not depend on the shape or apparent area of contact between sliding objects. He also introduced the coefficient of friction as the relation between the normal load and the friction load, and stated that μ was always equal to 1/4. Amazingly, he did this without the term 'force', which was introduced by Isaac Newton (1663 - 1705). In 1687, Newton published 'Principia', which has later been a basis of the studies of sliding friction. The first two laws of dry friction, were stated in 1699, by Guillame Amontons (1663 - 1705):

- The friction force is directly proportional to the applied normal load.
- The friction force is independent of the apparent area of contact.

Although similar to the results of Leonardo da Vinci 200 years earlier, these laws have later been known as Amontons' laws of friction. Charles Augustin Coulomb (1736 - 1806) added a third law to the laws of Amontons.

- The dynamic friction coefficient is independent of the velocity, the area of contact, and the surface roughness.

Coulomb might be most known for his contributions to the field of electromagnetism, but he also investigated numerous friction phenomena such as materials in contact and their surface coatings, the contact area, and the normal pressure. He also found that surfaces that remained in contact for a given time, experienced a logarithmic increase in the static friction threshold. The idea of asperities was widely used at the time of Coulomb, but the difference between the real and apparent area of contact was not

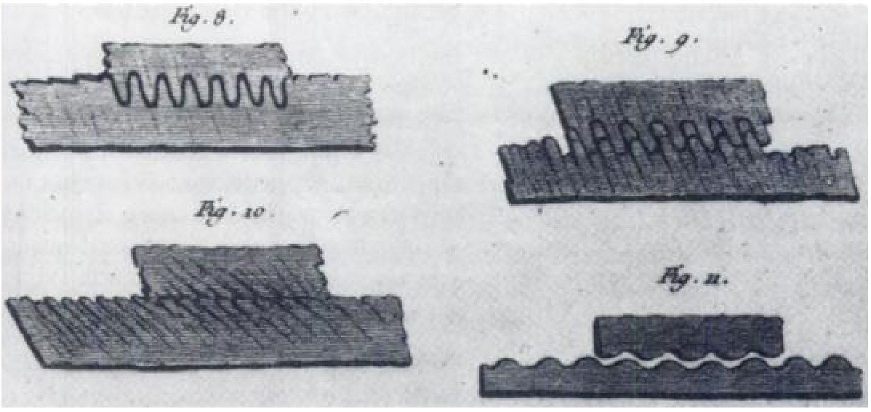

Figure 1.2: *Coulomb's visualization of rough surfaces in contact. The picture is taken from [1].*

known. This is demonstrated in figure (1.2), which is Coulomb's interpretation of rough surfaces in contact.

1.2.2 Theory of elasticity and contact mechanics

In 1882, Heinrich Hertz made a huge contribution to the field of tribology when he published 'On the contact of elastic solids'. At the time, Hertz was a research assistant at the University of Berlin, and was doing experiments on optical interference between glass lenses. He wanted to investigate the effects of contact and elastic deformation of his lenses, and developed a theory that is still widely used today. The theory is, however, restricted to normal contact of frictionless surfaces. In 1938 Cattaneo solved the problem of partial slip with a single dynamic friction coefficient when applying a tangential load in half space. Raymond D. Mindlin solved the problem independently in 1949 [4]. Partial slip during cylinder plane contact will be discussed in chapter 6.

1.2.3 The industrial revolution

During the industrial revolution, studies of tribology rose. This was primarily due to the need of a better understanding of lubrication surfaces and other industrial applications of tribology. One of the main contributions during this period was the theory of hydrodynamic lubrication developed by Euler, Bernoulli, Navier and Stoke.

1.2.4 Surface roughness and the real area of contact

In 1950 Frank Philip Bowden (1903-1968) said *'...putting two solids together is rather like turning Switzerland upside down and standing it on Austria - the area of intimate contact will be small.'* [3]. That year he had, together with David Tabor (1913-2005), published 'The friction and lubrication of solids' [6]. This difference between the real and apparent area of contact was quite different from the theories in Coulomb's time, demonstrated in figure (1.3). New technology had made it possible to measure the surface roughness, and in the 1960s Greenwood and Williamson developed a method to

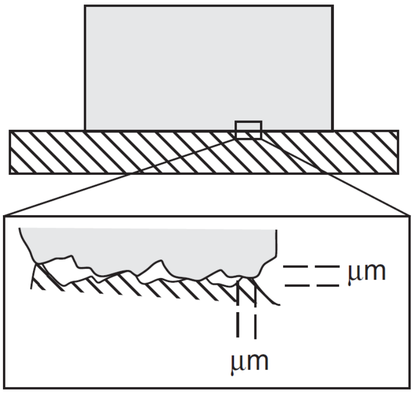

Figure 1.3: *The real area of contact is much smaller than the apparent area of contact. This was introduced by Bowden and Tabor in 1950. The figure is taken from [5].*

produce contour maps of surfaces. In 1966 they published the famous paper 'Contact of nominally flat surfaces' [7], where they introduce a surface model consisting of elastically independent asperities modeled as spheres. They proved that a purely elastic material could produce a real area of contact proportional to the applied load. In the late 20th century, little progress in fundamental studies of sliding friction was made. This was about to change due to access to new technology.

1.2.5 Rate and state friction laws

Since the introduction of the laws of dry friction, different approaches have been made [8] to include effects like melting and plastic deformation of the surfaces in contact. Among them are rate and state friction laws motivated by measurements of the friction coefficients. Experiments show that an Amontons-Coulomb friction law is a rough assumption. After an object has come to rest, there is a transition of the dynamic friction coefficient up to the static coefficient known as static aging. The static coefficient increases logarithmically in time, while the dynamic friction coefficient is velocity-weakening for small velocities.

These effects are described quantitatively with rate and state friction laws. The static aging can be described as

$$\mu_s(t) = B_1 + B_2 log(t), \tag{1.1}$$

where t is the time and B_1 and B_2 are constants. This effect is due to creep of load-bearing asperities at low melting temperatures, which leads to an increased surface area and an increased number of micro-contacts along the interface [9]. The dynamic friction coefficient depends on the sliding velocity, v, and the time-dependent state variable ϑ

$$\mu_k = \mu_{k,0} + B_3 log(\frac{v}{v_0}) + B_4 log(\frac{\vartheta}{\vartheta_0}). \tag{1.2}$$

ϑ is found from $\dot{\vartheta} = 1 - \frac{v\vartheta}{\chi}$ where χ is a characteristic length scale. It has been suggested that ϑ can be implemented as the average age of contacts. The B_3 term is known as the direct effect, and is velocity strengthening. It arises from thermally activated anelastic shear creep at the contact interface. The B_4 term comes from the logarithmic strengthening of contacts with time. In steady sliding, this term is velocity weakening [10]. The rate and state friction laws apply to a large number of different

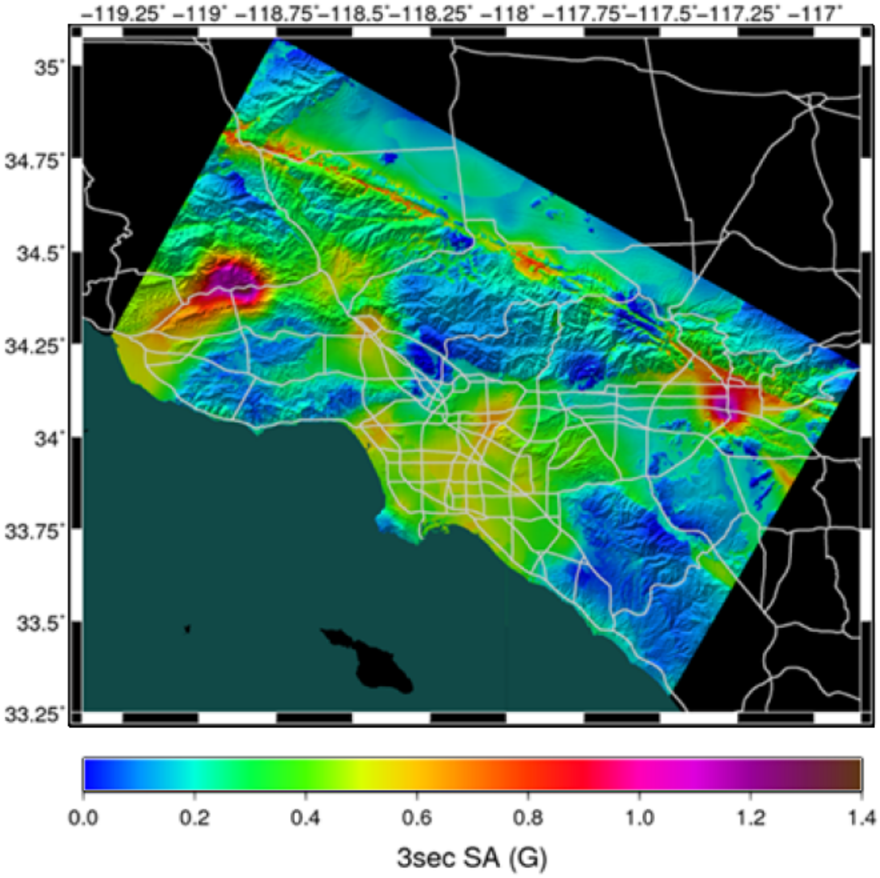

Figure 1.4: *CyberShake hazard map of Southern California. The color-map indicates the maximum force from a simulated earthquake, indicating where buildings should not be raised. The figure is taken from [13].*

materials e.g. rock, plastic and paper [8]. Geological experiments have also been used in discussions of rate and state friction laws [11].

1.3 The renaissance of friction

'The renaissance of friction', was the title of a paper published by Meyer and Urbakh in 2010 [12]. It describes the recent growing interest in studies of friction. The last years, new experimental techniques, such as the friction force microscope and the high speed camera, have been developed, and computer progress allows modeling of friction systems. These are important tools to understand the mechanisms of e.g earthquakes.

Friction is a multiscale problem, ranging from the atomic scale where quantum mechanics apply up to the large scales where the surface may seem flat. Friction is currently studied on these scales both experimentally and numerically. The studies range from the atomic scale and the modeling of single asperities, up to simulations of earthquakes in the whole region of California. Figure (1.4) shows a hazard map generated numerically from the CyberShake model that was built to simulate earthquakes in the California region [13]. Figure (1.5) shows a measurement of the surface topography of an ns-C film made with

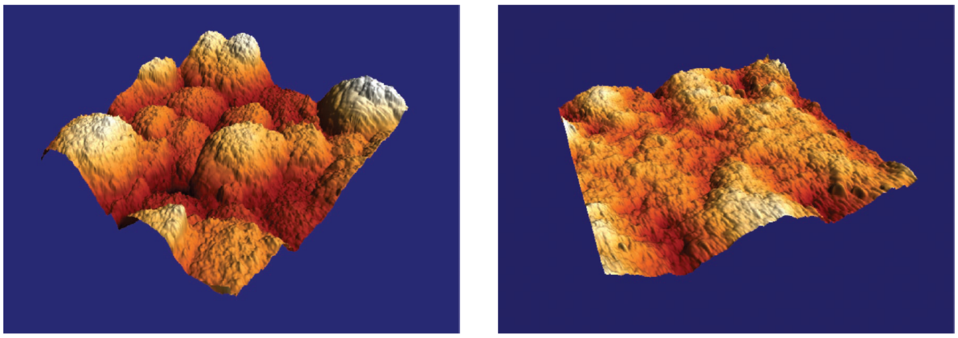

Figure 1.5: *Surface topography of a cluster assembled ns-C film (left), and a scratched ns-C film (right) measured by an atomic force microscope. The scan area is* $2.2 \times 2.2 \mu m^2$*. The figure is taken from [14].*

an atomic force microscope. These two figures demonstrate how different the scales are. One important question yet to be answered is how to bridge this gap between the small and large scales. In this thesis, two length scales are studied; the microscopic (micro-contact length scale) and the mesoscopic (limit of many micro-contacts).

1.3.1 The mesoscopic picture

The mesoscale has recently been the focus of intense experimental investigation, and considers the interplay between shear and normal stresses and crack dynamics. The mesoscale can be linked to the macroscale through integration.

A new real-time method of measuring the real surface area using PMMA (plexi-glass) on PMMA surfaces has given rise to new discussions. Friction used to be described through the motion of a rigid body, but recent experiments show that all transitions involve micro-slip and shear crack-like propagation. Micro-slip does not only appear in macroscopic stick slip, but also in localized events prior to macroscopic slip. These events are called precursors. Experimental and theoretical results suggest that these processes strongly depend on the way the system is loaded externally, which translates into the distribution of normal and shear stress at the interface.

Among the experimental contributors are Maegawa et. al [15], Rubinstein et. al [16–18], Ben-David et. al [19–22] (Ben-David belongs to the same experimental group as Rubinstein), Baumberger et. al [23] and Bennewitz et. al [24]. An introduction to some of the experimental results is given in chapter 2.

Theoretical approaches have also been made. A master equation approach has been made by Braun and Peyrard, which describes stick slip and smooth sliding regimes at the mesoscale [25, 26] and the dependence on dynamic friction on the velocity [27]. Scheibert [28] developed a quasi-static one-dimensional model describing the transistion from static friction to stick slip motion of an elastic block, where he discussed the effect of friction induced torque.

Numerical models of friction at the mesoscale have also been frequently used. One of them is the Burridge-Knopoff model [29] from 1967. Until recently most approaches have been statistical since the models often come at a high computational cost [30]. Recently, deterministic models that can describe the dynamics of the events have been used by Maegawa et. al [15] and Braun et al. [31, 32]. These ideas will be discussed further in part 2: A mesoscopic fricion model, where an introduction to relevant recent experiments is also given.

1.3.2 The microscopic picture: Surface topography

The local behavior in a mesoscopic model is governed by microscopic mechanisms. At this scale the fluctuations in the normal and shear stresses are large, and the contact between two solids is a multi-contact interface. The shear stiffness of single asperities in contact is important, as well as the distribution of asperity heights which is determined by the roughness of the surface. In general, the shear and normal stiffness of a thin surface layer is different from the shear stiffness of the bulk since the surface is effectively much softer.

The microscale has recently had important theoretical advances, where attempts of relating the surface topography to stress and strain behavior at the mesoscale are made.

The first major theoretical approach dates back to the 1960s, when Greenwood and Williamson published their famous paper 'Contact of nominally flat surfaces' [33]. They found a scaling relation between the normal load and the real area of contact, modeling a rough surface as semi-spheres individually determined by Hertz theory with a Gaussian height distribution. The result was successful, but was based on strong assumptions. The topography was not realistic, and the elastic interactions between asperities were neglected.

Different approaches have later been made to the scaling of the normal stiffness. Among them are Roux-Schmittbuhl [34] theory, and Persson theory [1, 35–37]. The real breakthrough was the theories developed by Persson, where the concept of asperities is not used. Instead, his theories describe a realistic topography coupled with elasticity theory. Among his theories is the scaling behavior of the surface compression versus the normal load and the normal pressure probability distribution. Good agreement between Persson's theory and recent numerical results by Akarapu et. al, Campana et. al. (both with Robbins) [38, 39], and by Persson himself (Almquist et. al) [37] have been found.

Akarapu et. al used molecular dynamics and continum calculations to find the normal and shear stiffness of self-affine surfaces [39]. They found that the stiffness of elastic solids is uniquely defined by the distribution of contact points, not the surface roughness or the normal load distribution. They also found that atomic scale deformations are important to the shear stiffness.

Theoretical approaches have not been made for the shear stiffness of surfaces more complex than two half planes in contact. A Greenwood Williamson type of approach was made by Boitnott in 1992 [40]. This kind of approach will be explored in part 3: A microscopic friction model.

In addition to numerical and theoretical approaches, experimental studies of rough surfaces have been made [41–43]. The most studied surfaces are the self-affine surfaces defined by the Hurst exponent H. One example of self-affine surfaces is surfaces generated from cracks [44]. They typically have a Hurst exponent of $H = 0.8$ [35]. Other examples mentioned frequently by Persson are asphalt and concrete road surfaces. Experimental results suggest that the normal stiffness depends on H [14, 45]. The second type of surfaces is fractal surfaces (gradient percolation surfaces) defined by the fractal dimension D [46]. They are typically generated through surface growth processes, and have quite complex geometries including e.g. overhangs. Few studies of contact mechanics of gradient percolation surfaces have been carried out.

1.4 Thesis structure

The thesis is divided into four parts; The introduction, the mesoscopic friction model, the microscopic friction model and the discussions. In the mesoscopic friction model, a one-dimensional model is introduced in order to describe some features of recent experiments, while the microscopic friction model is a study of the behavior of a thin surface layer.

Part II

A MESOSCOPIC FRICTION MODEL

The mesoscopic limit is the limit of a large number of micro-contacts at the contact interface between two solids. The stresses measured at this scale are results of microscopic effects. In order to develop a mesoscopic friction model, assumptions have to be made. These assumptions are often integrated in the model through a local friction law.

This part consists of two chapters. I start with a brief introduction of recent friction experiments with emphasis on experimental results that are investigated in later chapters. I further introduce a one-dimensional mesoscopic fricion model assuming a Amontons-Coulomb friction law, and compare results with recent experiments.

Chapter 2

Mesoscopic experiments and models

As mentioned in the introduction, a new real-time method of measuring the contact area of a PMMA on PMMA interface has been developed. In this chapter I will give a brief introduction to some of the details of these experiments, with emphasis on the experimental results I will compare to numerical calculations.

2.1 Experimental setup

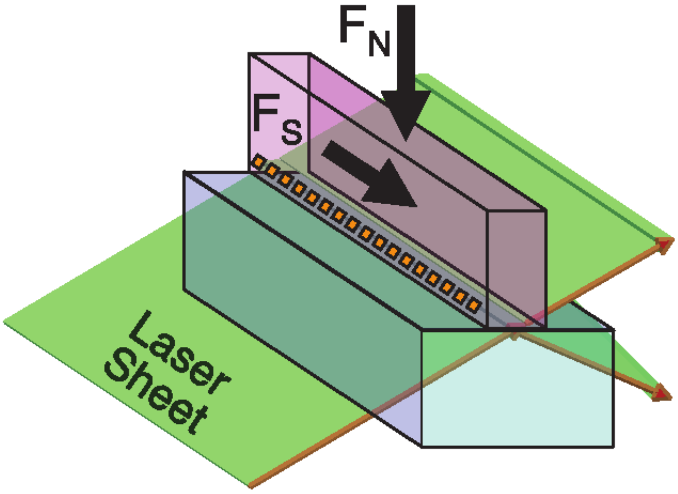

Figure 2.1: *The experimental setup of the Ben-David 2010 experiment. The slider is subjected to a normal load F_N and a tangential load F_S. The figure is taken from [21].*

Figure (2.1) shows the experimental setup of the Ben-David experiment from October 2010. Since PMMA is transparent, a laser beam can be used to measure the real area of contact. The laser is aimed so that there is no reflection when there is microscopic contact between the two PMMA surfaces. When there is no microscopic contact between the surfaces, there will be total reflection of the beam due to the contact between PMMA and air. By measuring the intensity of the transmitted light and noting that it is proportional to the contact area, a measure of the real area of contact is obtained. The experiment is recorded using a high speed camera. When the sample slips, the micro-contacts at the interface rearrange, and the light intensity changes. In this way, the length and velocities of the micro-slips can be measured.

2.1.1 Boundary conditions

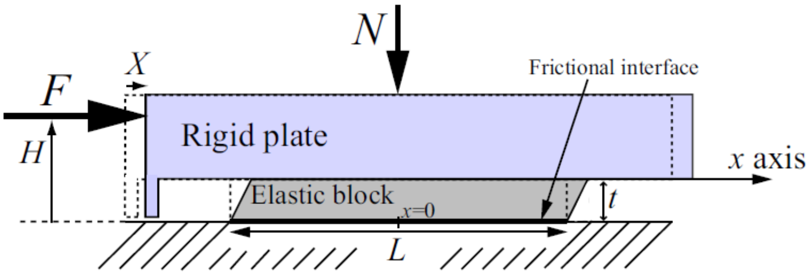

Figure 2.2: *Experimental setup of a top-driven system by Scheibert et. al. The figure is taken from [28].*

There are many ways to impose a tangential load to the system. Maegawa uses a soft spring, with a spring constant K, to drive the system from the edge with a driving velocity v. A different approach is demonstrated in figure (2.2). It shows the experimental setup of a recent experiment by Scheibert [28]. The elastic block is driven by a rigid plate attached to the top. This setup allows the external torque to be controlled by changing the position of the applied tangential load. The way the normal load is imposed is also important. Many experiments use a uniform normal loading at the top of the sample, giving a non-uniform normal load at the contact interface. A different approach made by Maegawa is to impose a non-uniform linear normal loading at the top. The different types of boundary conditions are explored in chapter 3.

2.2 Experimental results

2.2.1 Contact area and pressure profiles

A measurement of the contact area (light intensity) as a function of the applied normal load is plotted in figure (2.3). A contact area that increases linearly with the load is obtained.

In addition to contact area measurements, stress profiles at the contact interface can be found. Measurements by Ben-David et al. are plotted in figure (2.4) for a side-driven slider with a uniform normal load at the top. The shear stress profile at the contact interface depends on the Poisson ratio and the shape (the aspect ratio) of the slider.

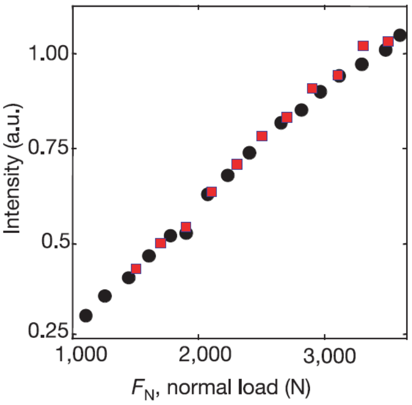

Figure 2.3: *The real area of contact of the interface between two PMMA blocks is proportional to the applied normal load. The area is measured through the intensity of the transmitted light. The different symbols show two different experiments. The figure is taken from [16].*

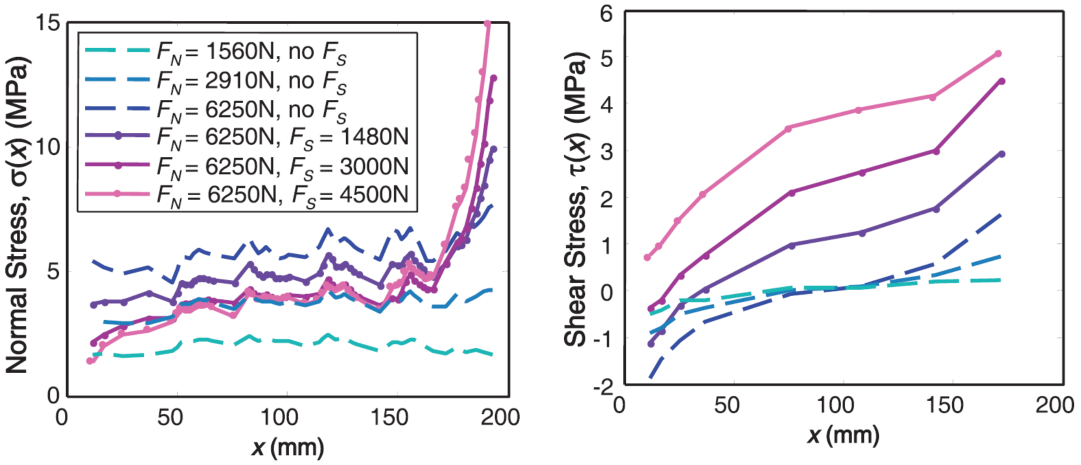

Figure 2.4: *Left: Normal stress distribution at the contact interface between two PMMA blocks.* F_N *is the total normal load and* F_S *is the total tangential load. The normal stress distribution is not constant and changes with the applied tangential load. Right: Shear stress distribution at the contact interface. The shear stress distribution is antisymmetric due to the Poisson ratio. The system is driven from the side. The normal load at the top is uniform. The figure is taken from [21].*

2.2.2 Stick slip and steady sliding

Based on the spring constant and velocity of the push, three main types of global behavior are found [1]:

- Steady sliding
- Periodic stick slip
- Chaotic stick slip

A periodic stick slip regime measured by Maegawa is plotted in figure (2.5). The elastic block comes to rest between events, and the tangential load has to increase to restart the system. An event consists of a detachment front that does not necessarily propagate all the way through the material. Events that propagates all the way through are called global events, while events prior to global events are called precursors. A sketch of the

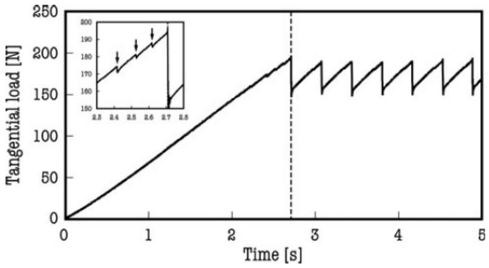

Figure 2.5: *Tangential force as a function of time. The tangential force decreases when an event is triggered. These events are called precursors. The figure is taken from [15].*

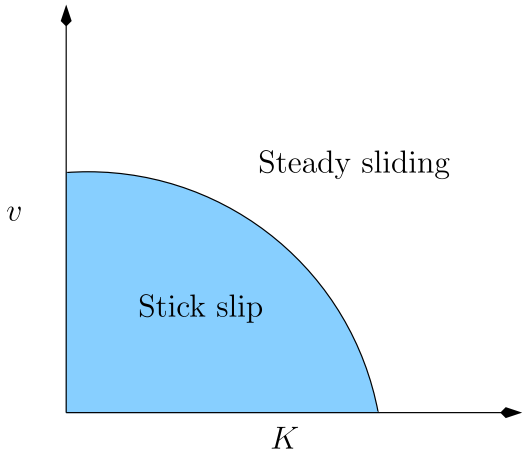

Figure 2.6: *Sketch of a dynamic phase diagram. The filled region shows values of K and v where stick slip motion occurs.*

dynamic phase diagram for stick slip behavior is plotted in figure (2.6). A combination of small K and v gives stick slip behavior, while large values of K and v result in a steady sliding regime.

2.2.3 Precursor events

The events can be recorded using a high speed camera. As the fronts propagate, the micro-contacts rearrange and become visible due to the change in light intensity. Figure (2.7) shows a front that propagates across the contact interface. The micro-slip fronts propagate at velocities different from the speed of sound [22]. Ben-David et al. divide them into three types of fronts: Slow fronts, sub-Rayleigh fronts and supersonic fronts. Experimental results suggest that the non-uniformity in the normal pressure is important. It governs the global static friction coefficient, and the type of front that is observed. A high initial shear stress gives a high rupture velocity.

The length of the micro-slip events as a function of the tangential load has been measured by Maegawa. This is shown in figure (2.8). The precursor lengths depend on the normal load at the contact interface.

2.3 Numerical models

Maegawa also suggested to use a simple spring block model with a local Amontons-Coulomb friction law to understand the behavior of the PMMA friction system [15] on the onset of sliding friction by measuring the precursor lengths. They used the same setup as Ben-David et al. Figure (2.8) shows the experimental and numerical results. The agreement between the numerical model and the experimental data is not satisfactory. This will be investigated in chapter 3. The model they used is known as the Burridge-Knopoff model from 1967 [29], named after its inventors. In 2001, Knopoff

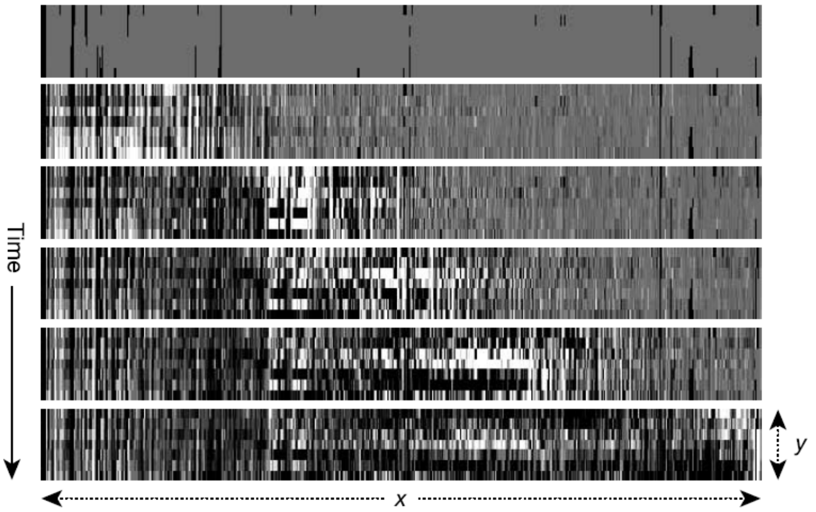

Figure 2.7: *Picture of the light intensity at the contact interface during one event of* $1.4ms$*. Light colors correspond to a large contact area. A detachment front propagates across the interface from left to right. Behind the front the micro-contacts rearrange. In this way, front velocities and lengths can be measured.The figure is taken from [16].*

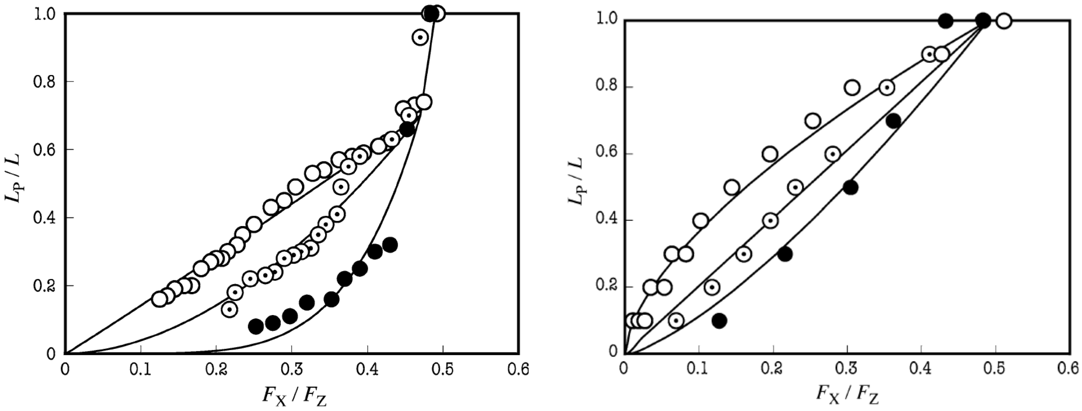

Figure 2.8: *Left: Precursor lengths of the Maegawa experiments. Right: Precursor lengths of a numerical spring block model. Precursor lengths for imposed normal loads with different angles. The numerical model assumes a linear distribution of the normal load at the bottom surface. The figure is taken from [15]*

analyzed the viscous damping of this kind of system [47]. This model has also been used by geologists to analyze faults [48].

A slightly different approach was made by Urbakh, Braun and Barel in 2009 [31]. They introduced a local friction law based on springs breaking and reforming. This approach was made to simulate contact between asperities. The focus of their studies was the different crack fronts observed in experiments. They followed up with an article in 2011 [32], where they suggest that there is a forbidden gap in the crack velocities. Slow fronts are observed in their model.

2.4 Open questions

Many aspects of the experimental results in this chapter are not fully understood. Among them are:

- How does the velocity of the detachment front depend on the inter-facial stress distributions? (This will not be investigated in this thesis)
- What determines the precursor lengths?
- What is the mechanism responsible for the slow fronts? Why are they found in the Urbakh model?
- Can predictions for the next events be found? This is relevant to the study of earthquake prediction.

In order to investigate this a one-dimensional spring block model is introduced, with focus on precursor predictions.

Chapter 3

One-dimensional friction models

Inspired by the numerical scheme by Maegawa et al. [15] we introduce the one-dimensional Burridge-Knopoff model [29]. Experimental results for the precursor lengths as a function of the applied force are not fully consistent with the experimental data. We will investigate if small changes in the model can explain some of the features of the experiments, or if a more complicated model is needed.

3.1 The 1D side-driven spring block model

The elastic block with mass M and Young's modulus E is modeled as a one-dimensional array of local blocks connected with springs. The two-dimensional Poisson effect is neglected. The frictional interface is modeled with a simple Amontons-Coulomb friction law. This is a mesoscopic friction model, where the microscopic effects are implemented through local friction law. The model is used because we want to find the simplest possible numerical model that describes this system sufficiently.

Figure (3.1) shows a simple sketch of the side-driven spring block model. N blocks are connected with linear springs with spring constants k. Each local block has a mass $m = M/N$, and an individual normal load w_i. The system is driven from the side by an artificial point, connected to the system with a spring constant K. K is chosen to be softer than k. The artificial point is driven with a constant velocity v, resulting in a force F_x on the first block. The springs have an equilibrium length d, and the total system length is L. The parameters are set to the ones of the Maegawa experiment, in

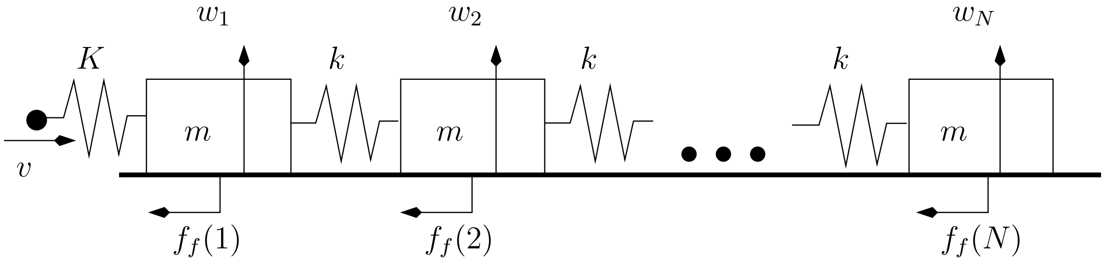

Figure 3.1: *Sketch of the spring block model used by Maegawa.*

order to mimic the results. The friction law used is a local Amontons-Coulomb friction law with a static friction coefficient μ_s and a kinetic friction coefficient μ_k.

3.1.1 Elastic properties of the system

We want to model a material with length L, mass M, normal load F_z, and a spring constant k_{total} as N blocks and N-1 springs. This means that each block has the following properties: The mass is given by

$$m = M/N \tag{3.1}$$

The normal load is

$$w_i = w_{\text{normal}} + w_{\text{torque}} = \frac{F_z}{N}\left(1 + \frac{(2i - N - 1)\theta}{N-1}\right) + \frac{gF_x}{N}\left(\frac{2N - N - 1}{N-1}\right) \tag{3.2}$$

where θ controls the distribution of the normal load, and g controls the torque. g and θ do not affect the total normal load. This equation is motivated by a linear change in the applied normal load introduced by Maegawa [15]. Experiments suggest that the normal load is important to the precursor lengths. In addition we introduce a linear torque parameter motivated by a recent quasi-static 1D model by Scheibert et. al [28]. The lattice spacing is

$$a_0 = \frac{L}{N-1}. \tag{3.3}$$

In this case the lattice spacing is equal to the equilibrium spring length $d = a_0$. The total spring constant of the connected springs is

$$k_{\text{total}} = \frac{N-1}{k}. \tag{3.4}$$

We may also derive k_{tot} using the definition of Young's modulus (the reader is referred to chapter 4 for a more detailed introduction to elasticity theory)

$$E = \frac{F_\perp L}{S \Delta L}, \tag{3.5}$$

where $F_\perp$ is the perpendicular force applied, L is the original length of the object, S is the cross-sectional area where the force is applied, and ΔL is the change in length of the object because of the applied force. This leads to

$$F_\perp = \frac{ES}{L}\Delta L, \tag{3.6}$$

and if we now let

$$k_{\text{total}} = ES/L, \tag{3.7}$$

we see that this is Hooke's law for linear springs. We can now define the local spring constant by combining equations (3.4) and (3.7).

$$k = (N-1)ES/L \approx NES/L, \quad N >> 1. \tag{3.8}$$

3.1.2 Equations of motion

The equations of motion are as follows:

$$m\ddot{x}_1 = F_x + k_1(x_2 - x_1 - d) + f_{f,1} \tag{3.9}$$

$$m\ddot{x}_i = k_{i-1}(x_{i-1} - x_i - d) + k_i(x_{i+1} - x_i - d) + f_{f,i} \tag{3.10}$$

$$m\ddot{x}_N = k_{N-1}(x_{N-1} - x_N - d) + f_{f,N}, \tag{3.11}$$

where f_f is the friction force. We can now make a variable change to the displacement $u_i = x_i - di$. This gives us the following equations:

$$m\ddot{u}_1 = F_x + k_1(u_2 - u_1) + f_{f,1} \tag{3.12}$$

$$m\ddot{u}_i = k_{i-1}(u_{i-1} - u_i) + k_i(u_{i+1} - u_i) + f_{f,i} \tag{3.13}$$

$$m\ddot{u}_N = k_{N-1}(u_{N-1} - u_N) + f_{f,N} \tag{3.14}$$

The force on the first block is given by

$$F_x = K(u_0 - u_i) = K(vt - u_1), \tag{3.15}$$

where v is the pushing speed of the artificial point, and t is the time. f denotes a local force. The friction force is given by

$$f_f = \begin{cases} f_s^i & \dot{u}_i = 0 \\ -f_k^i & \dot{u}_i > 0 \\ f_k^i & \dot{u}_i < 0 \end{cases} \tag{3.16}$$

Where f_s denotes static friction and f_k is the kinetic friction. The static friction depends on the tangential load on the block, and is in the range

$$-\mu_s w_i = -f^i_{s,max} \leq f_s^i \leq f^i_{s,max} = \mu_s w_i. \tag{3.17}$$

The kinetic friction is given by

$$f_k^i = \mu_k w_i. \tag{3.18}$$

3.1.3 Viscous damping

To avoid local oscillations, we introduce a velocity-dependent damping η, which gives an additional term to the equations of motion

$$\sum_{j=1}^{N}\sum_{l=1}^{n} \eta_{ij}(v_{l,j} - v_{l,i}), \tag{3.19}$$

where n is the number of neighbor blocks. Knopoff and Ni showed that the Burridge-Knopoff model [29] results in oscillations at the lattice cutoff frequency $2\sqrt{k/m}$ with wavelength two times the lattice spacing [47], which is also observed in our spring block model without damping. The effects of adding a damping term is illustrated in figure (3.2). To find a good value of η, we calculate the dispersion relation for the system

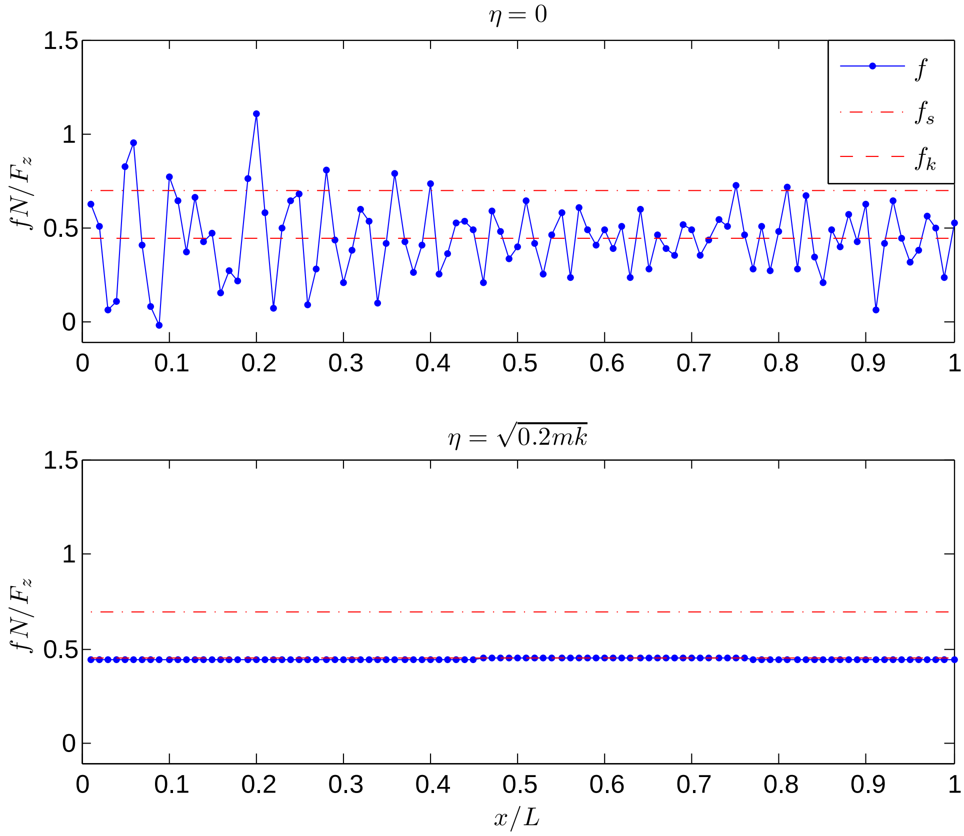

Figure 3.2: *The force distribution during steady sliding in the side-driven Burridge-Knopoff model with (bottom) and without (top) viscous damping. With no damping, traveling waves with wavelength two times the lattice spacing are dominating. A viscous damping term removes this dicretization problem.*

including the damping term. The equation of motion for a single block including the viscous damping during slip is

$$m\ddot{u}_j = k(u_{j+1} + u_{j-1} - 2u_j) + \eta(\dot{u}_{j+1} + \dot{u}_{j-1} - 2\dot{u}_j) + w_j\mu_k. \tag{3.20}$$

We look for solutions on the form

$$u_{j\pm1} = ue^{ij\kappa a_0}e^{\pm i\kappa a_0}e^{\omega t}, \tag{3.21}$$

where $\kappa = 2\pi/\lambda$ is the wave number, ω is the angular frequency of the oscillation, and a_0 is the lattice spacing. Inserting this in equation (3.20) gives

$$\omega^2 me^{ij\kappa a_0} = (k + \eta\omega)(e^{i(j+1)\kappa a_0} + e^{i(j-1)Ka_0} - 2e^{ij\kappa a_0}) - w_j\mu_k, \tag{3.22}$$

and it follows that

$$\omega^2 - \frac{2(k - \eta\omega)}{m}(\cos(\kappa a_0) - 1) + w_j\mu_k = 0. \tag{3.23}$$

Solving this equation with respect to ω gives the dispersion relation

$$\omega(\kappa) = -\frac{2\frac{\eta\omega}{m}(1 - \cos(\kappa a_0)) \pm \sqrt{4\frac{\eta^2}{m^2}(1 - \cos(\kappa a_0))^2 - 4(\frac{2k}{m}(1 - cos(\kappa a_0)) + w_j\mu_k)}}{2}. \tag{3.24}$$

When applying viscous damping to the system, we want to avoid over-damping, which occurs when the root has two real solutions. In order to avoid that, we want

$$\frac{\eta^2}{m^2}(1-\cos(\kappa a_0))^2 \leq (\frac{2k}{m}(1-\cos(\kappa a_0)) + w_j\mu_k). \tag{3.25}$$

which gives a restriction to η

$$\eta \leq \sqrt{\frac{2mk}{1-\cos(\kappa a_0)} + \frac{m^2 w_j \mu_k}{(1-\cos(\kappa a_0))^2}}. \tag{3.26}$$

If we neglect the friction term we have that

$$\eta \leq \sqrt{\frac{2mk}{1-\cos(\kappa a_0)}}. \tag{3.27}$$

The smallest possible wavelength is two times the lattice spacing a_0. That gives

$$\eta \leq \sqrt{mk}. \tag{3.28}$$

This mode is the most damped mode, and we use a damping factor $\eta = \sqrt{0.2mk}$ in order to get rid of the two node oscillations.

3.1.4 Numerical scheme

The equations above were implemented with a Runge Kutta method of fourth order. It is important to keep track of the friction type of each block. This is done with a simple test. If a block under static friction experiences a force larger than $\mu_s w_i$, it starts to slide. If the velocity of a block under dynamic friction goes to zero, we change the friction type to static.

Runge Kutta of fourth order

The equations of motion were solved using a Runge-Kutta method of fourth order [49]. We start by calculating the acceleration and velocity (the slope) of a block at the time t

$$\begin{aligned} b_{x,1} &= \Delta t f_i\left(x(t), v(t)\right)/m \\ b_{v,1} &= v_i(t)\Delta t. \end{aligned} \tag{3.29}$$

$f_i(x(t), v(t))$ is the force acting on block i at the time t. This is Euler's method. We further compute the slope at the midpoint $t + \Delta t/2$

$$\begin{aligned} b_{x,2} &= \Delta t f_i\left(x(t) + b_{x,1}/2, v(t) + b_{v,1}/2\right)/m \\ b_{v,1} &= (v_i(t) + b_{x,2})\Delta t/2. \end{aligned} \tag{3.30}$$

The step is repeated to get an improved slope at the midpoint.

$$\begin{aligned} b_{x,3} &= \Delta t f_i\left(x(t) + b_{x,2}/2, v(t) + b_{v,2}/2\right)/m \\ b_{v,3} &= (v_i(t) + b_{x,3})\Delta t/2 \end{aligned} \tag{3.31}$$

With this result we calculate the slope at the end point $t + \Delta t$

$$\begin{aligned} b_{x,4} &= \Delta t f_i \left(x(t) + b_{x,3}, v(t) + b_{v,3}/2 \right)/m \\ b_{v,4} &= (v_i(t) + b_{x,4})\Delta t \end{aligned} \tag{3.32}$$

Using Simpson's rule of integration we sum up the weighted mean and find the final values of the position and velocities at $t + \Delta t$

$$\begin{aligned} x(t + \Delta t) &= x(t) + (b_{x,1} + 2b_{x,2} + 2b_{x,3} + b_{x,4})/6 \\ v(t + \Delta t) &= v(t) + (b_{v,1} + 2b_{v,2} + 2b_{v,3} + b_{v,4})/6. \end{aligned} \tag{3.33}$$

The error term of the Runga-Kutta method of fourth order is $O(\Delta t^5)$ in the velocities and $O(\Delta t^4)$ in the positions.

Improving algorithm speed: An event-driven algorithm

The algorithm can be improved further by noting that the system is actually at rest most of the time if it is in a stick slip regime. The time steps where the system is at rest can be skipped by calculating the time until the first block will move. We wish to find the time of the next event, that will trigger when

$$f_i(t) = (w_{\text{normal}} + w_{\text{torque}})\mu_s, \tag{3.34}$$

where $f_i(t_0)$ is the total force on a block, and $t = t_0 + t_s$ is the time of the next event. Solving this for the time t_s, and taking the minimum with respect to i we find

$$t_s = min\left(\frac{1}{K_i v} \frac{\mu_s\left(\frac{(gF_x(t_0)(2i-N-1)}{N(N-1)} + w_i\right) - f_i(t_0)}{1 - N_t/N\mu_s g(2i - N - 1)/(N-1)} \right), \tag{3.35}$$

where K_i is the driving spring constant of block i, $f_i(t_0)$ is the force on block i at the time t_0 when the system is at rest and and N_t is the number of blocks that are connected to the driving of the system. For the side-driven model $N_t = 1$. We will later in this chapter introduce a top-driven model where $N_t = N$. We have assumed that the driving spring constants are equal. We further have that

$$F_x(t_0) = \sum_i K_i(vt - x_i(t_0)). \tag{3.36}$$

The minimum of the function gives the time of the next event. When implementing this in the Runge Kutta algorithm, we start calculation a few time steps before the estimated time t_s so that the events become distinguishable.

Choice of Δt

A simple analysis of the oscillation frequency of one block is performed. We look at a block of mass m that is connected to a spring with a spring constant k, which again is connected to a wall. The force on the block according to Hooke's law is

$$F = -kx = m\ddot{x}. \tag{3.37}$$

Parameter	Description	side-driven	top-driven
N	Number of blocks	100	100
K	Spring constant of push	8×10^5N/m	$\frac{8\times10^5}{N}$ N/m
v	velocity of push	1×10^{-2}m/s	1×10^{-2}m/s
Δt	Time step	1×10^{-7}s	1×10^{-7}s
F_z	Total normal load	400N	400N
θ	Angle of normal distribution	0	0
M	Total mass	0.012kg	0.012kg
E	Young's modulus	2.5×10^9N/m^2	2.5×10^9N/m^2
S	Cross-section area	1×10^{-4}m^2	1×10^{-4}m^2
L	Length	0.1m	0.1m
μ_s	static friction coefficient	0.7	0.7
μ_k	kinetic friction coefficient	0.45	0.45
g	dimensionless torque parameter	0	0

Table 3.1: *The list of parameters used in the 1D spring block model. The parameters are chosen to mimic the results of the Maegawa experiment [15].*

This is a simple harmonic oscillator with oscillation frequency

$$\omega = \sqrt{\frac{k}{m}}. \tag{3.38}$$

We need to choose Δt so that this frequency is sufficiently sampled. This means that

$$\Delta t << \frac{2\pi}{\omega} = 2\pi\sqrt{\frac{m}{k}}, \tag{3.39}$$

where k is the local spring constant. This will be a challenge when we want to simulate systems with a large number of blocks, since the local spring constant grows linearly as N increases. The local mass is given by $m = M/N$. This means that Δt will decrease as $1/N$, and the total number of floating point operations will increase as

$$\sim N^2, \tag{3.40}$$

which means that it will be difficult to simulate very large systems.

3.1.5 Numerical results

With the model well established, we move on to the numerical results. The parameters used are listed in table (3.1). If any parameter is different from this, it will be specifically stated in the figure text.

Uniform normal loading ($\theta = g = 0$)

Figure (3.3) shows the pushing force and the length of the slips as a function of time. The model produces precursor events of increasing length propagating from the trailing edge until a global slip occurs at $t = 2.68$s. This is consistent with experimental observations [15, 18]. We further identify the macroscopic stick slip behavior in the tangential

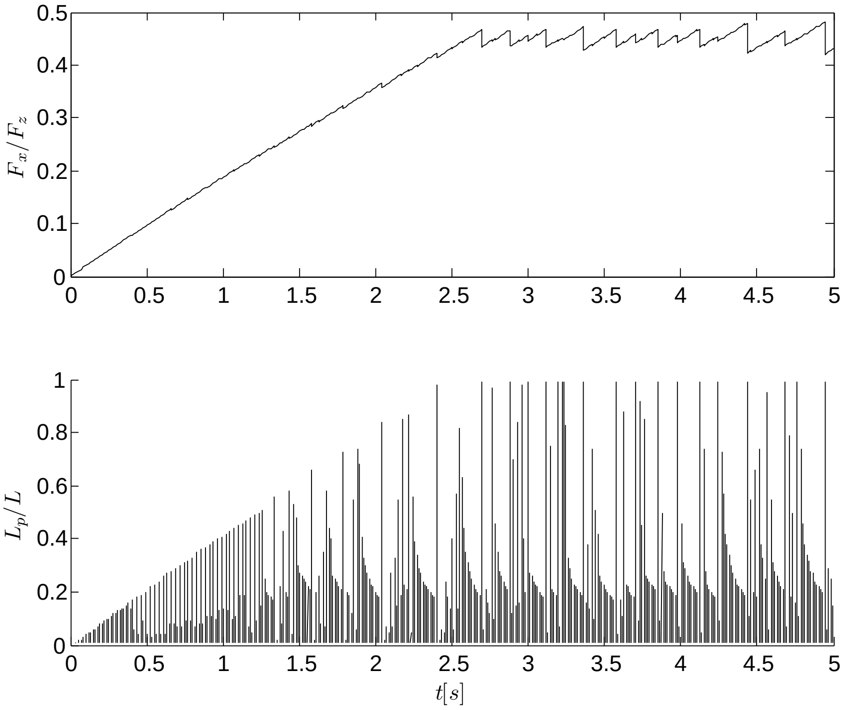

Figure 3.3: *The driving force (top) and the length of the precursors (bottom) as a function of time. The force increases until it reaches a stick slip regime with a global static friction coefficient different from the local. The length of the precursors increases steadily until this regime is reached.*

force curve (chaotic stick slip). What should be noted is that the global static friction coefficient is different from the local static friction coefficient μ_s. After the first global event, the system enters a slightly different regime. This can be understood if we have a closer look at the force distributions in the material.

Figure (3.4) shows three states where the system is at rest. The crack propagates from the trailing edge, and the force ends up approximately at the dynamic friction level. When the system comes to a rest, a spike in the force distribution appears at the crack tip. After the first global event, the shear force distribution is close to the dynamic friction level. When the system comes to rest after a global event, the spike in the shear force distribution appears at the position where the first block stopped.

The dynamics of the system

Figure (3.3) does not tell us much about the movement of local blocks inside of the material while it is sliding. We can look at these waves by plotting the velocity of each block during a slip. Each event shows quite complex dynamics. This is shown in figure (3.5), where the velocity distribution in the material is plotted as a function of the time for the first global event.

One can clearly see the reflections of the propagating waves through the material. The velocity of the crack is interpreted as the velocity of the detachment front. This is a different measure than the local block velocity. This velocity depends on the initial

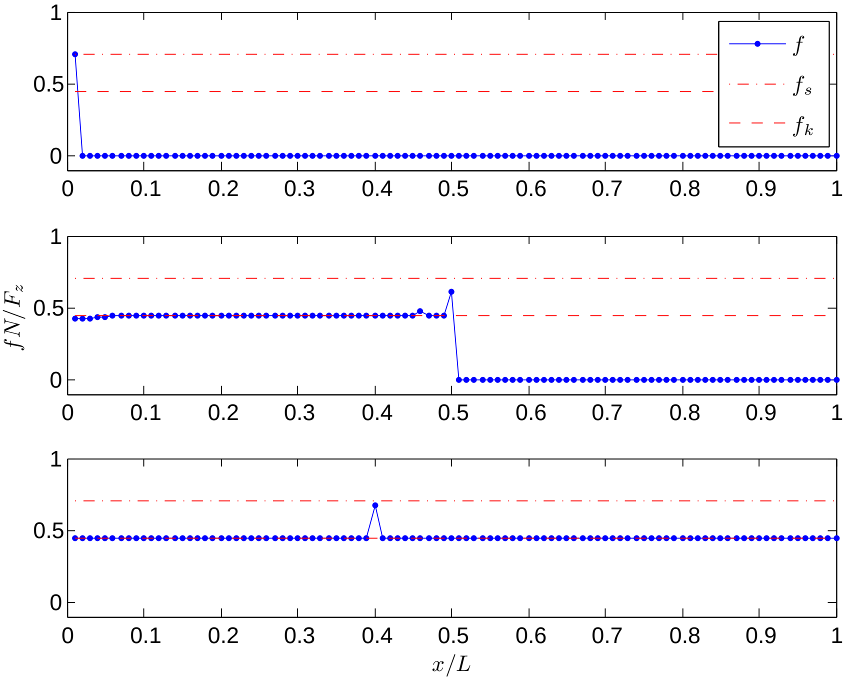

Figure 3.4: *Three different states where the system is at rest: Prior to the first precursor (top), after a few precursors (middle), after the first global event (bottom). The crack propagates from the trailing edge, and the force ends up approximately at the dynamic friction level. The whole system is close to the dynamic friction level when it stops. A spike in the force distribution appears at the crack tip. Parameters from table (3.1) side-driven.*

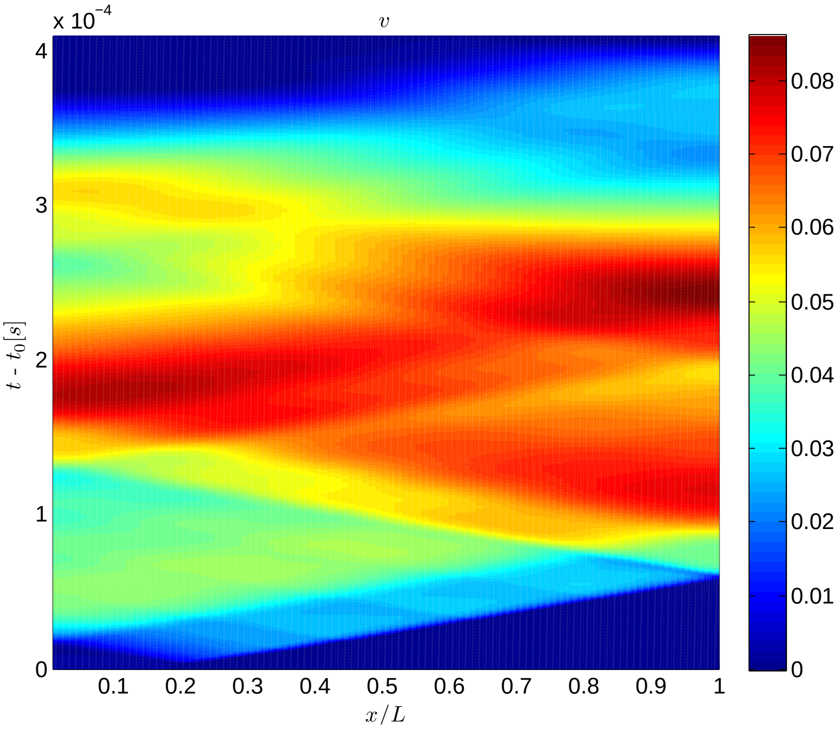

Figure 3.5: *The velocity distribution in time for the first global event in figure (3.3). Note that the velocity of a local block is a different measure than the crack velocity.*

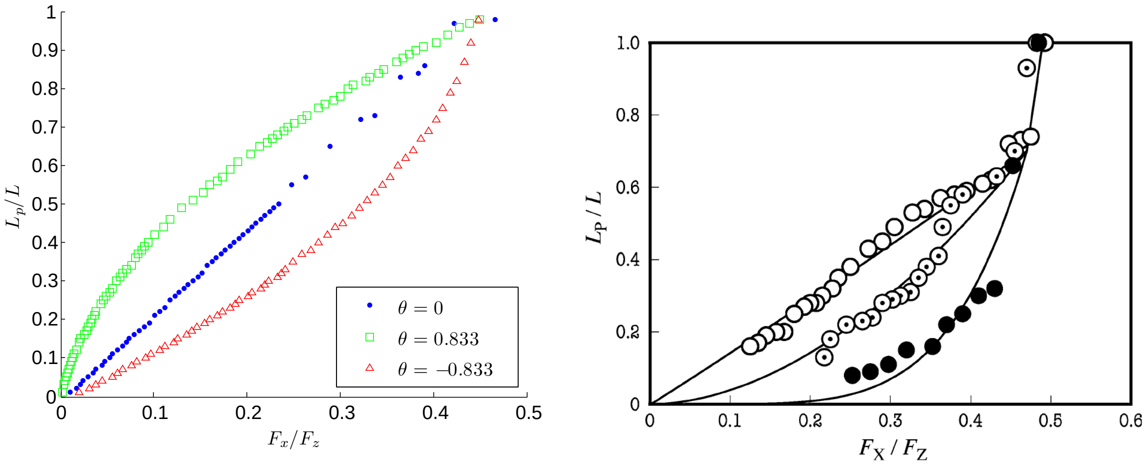

Figure 3.6: Left: The propagation length of the precursors as a function of the applied force F_x for three values of θ giving a non-uniform loading. Right: Experimental result from Maegawa et. al [15].

shear force distribution. These crack velocities have been studied in detail in the master thesis of David Skålid Amundsen [50].

Non-uniform initial loading

We add non-uniform loading by changing the variable θ from equation (3.2). $\theta > 0$ decreases the load at the trailing edge, while $\theta < 0$ increases it. The experimental result of the precursor lengths by Maegawa et al. and the measured precursor lengths in the model as a function of the applied tangential force F_x are shown in figure (3.6). We see that an increase in θ results in longer precursors at an earlier stage, while decreasing θ has the opposite effect. The precursors that are shorter than the previous one are removed in the figure. The global trend and relative position of the three curves are in agreement with experimental results. However, the detailed quantitative agreement with experimental results is not satisfactory, suggesting that some effects are missing in our model.

The effect of torque in the system

It is difficult to push a system without adding torque to it. We introduce torque in our system, and test if the precursor lengths we find are closer to experimental observations. The applied torque can only be balanced at the interface by an asymmetric distribution of normal forces. This torque is modeled as a change in the normal load through the system, that is proportional to the force F_x. We further assume that the change in normal load due to the applied torque changes linearly through the system, so that the total normal load remains constant. This assumption does not consider effects on the edges of the system that may appear because of the elasticity of the material. A linear model is used because it is the simplest possible model, and we may have to use a more complex model of torque to model the system correctly. To get a more realistic torque model, a two-dimensional spring block model should be introduced. The dimensionless parameter g models the amplitude of the torque. The normal load will now change at every time step according to equation (3.2) The largest possible value of g depends on the maximum value of F_x, N and F_z. For set 1 in table (3.1), the maximum value of g that always gives a $w_i > 0$ is approximately 2. g can be expressed as a function of the height of the push h on a $(L_x \times L_y)$ block. The part of the normal force distribution w that causes a net torque T can be written in terms of the position x as

$$w_{\text{torque}}(x) = gF_x \frac{2x - L_x}{L_x^2} dx \tag{3.41}$$

The torque due to this force on the bottom of the block is

$$T_w = 4 \int_0^{L_x/2} gF_x \frac{x^2}{L_x^2} dx = \frac{gF_x L_x}{6}. \tag{3.42}$$

The torque due to the push on a height h at a block with total height L_y is given by

$$T_p = F_x(h - \frac{L_y}{2}). \tag{3.43}$$

Because there is no movement, the net torque is zero. We can then find g as a function of H

$$T_w = T_p \tag{3.44}$$

$$g = \frac{6(h - L_y/2)}{L_x}. \tag{3.45}$$

The resulting effect on the shear force distribution is shown in figure (3.7) The friction thresholds are tilted due to the tangential force that increases over time. The shear force distribution still lies approximately at the dynamic friction threshold when the system comes to a rest, with a spike at the edge of the crack. The behavior of the system is the same, but the friction thresholds change with the applied tangential load. The effect on the precursors is illustrated in figure (3.8) Inserting the parameters of the Maegawa experiment in equation (3.45) gives a maximum possible torque parameter $g \approx 1.2$. From the figure we see that this is not a very large effect. In addition, the precursor lengths increase at an earlier stage for $g > 0$, which is the opposite of what we had hoped for. Adding torque does not give results closer to the experimental observations, the results are actually more different with torque than without.

The assumption of a linear asymmetry in pressure due to an applied torque is expected to be quite rough in the side-driven case, and due to this it is not very surprising that the results are not close to experimental observations. In a top-driven system, the assumption of a linear asymmetry can be justified.

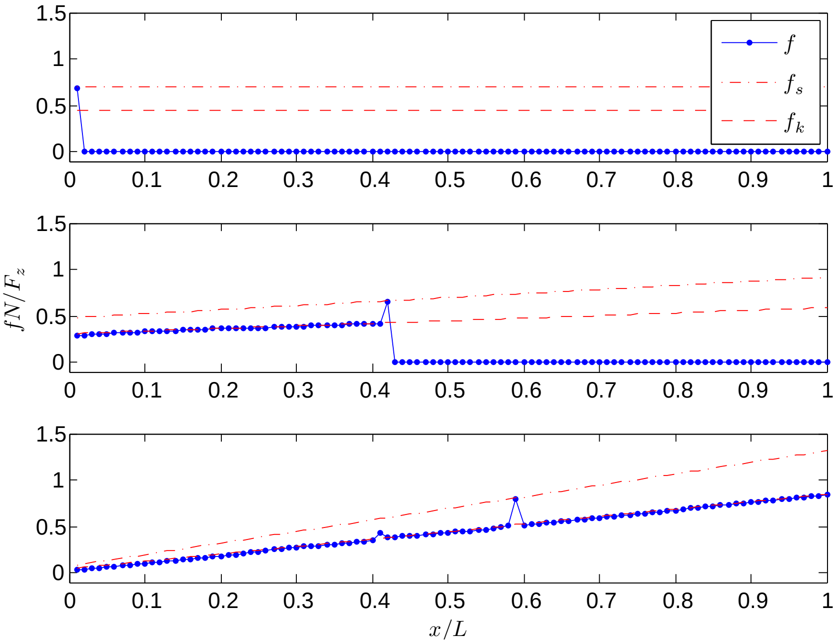

Figure 3.7: Three different states where the system is at rest: Prior to the first precursor (top), after a few precursors (middle), after the first global event (bottom). The crack propagates from the trailing edge, and the force ends up approximately at the dynamic friction level. When the stick slip regime is reached. The whole system is close to the dynamic friction level when it stops. Due to the torque, the local normal force distribution is changed, increasing the friction threshold at the leading edge, and decreasing it at the trailing edge. Parameters from table (3.1) side-driven with $g = 2$.

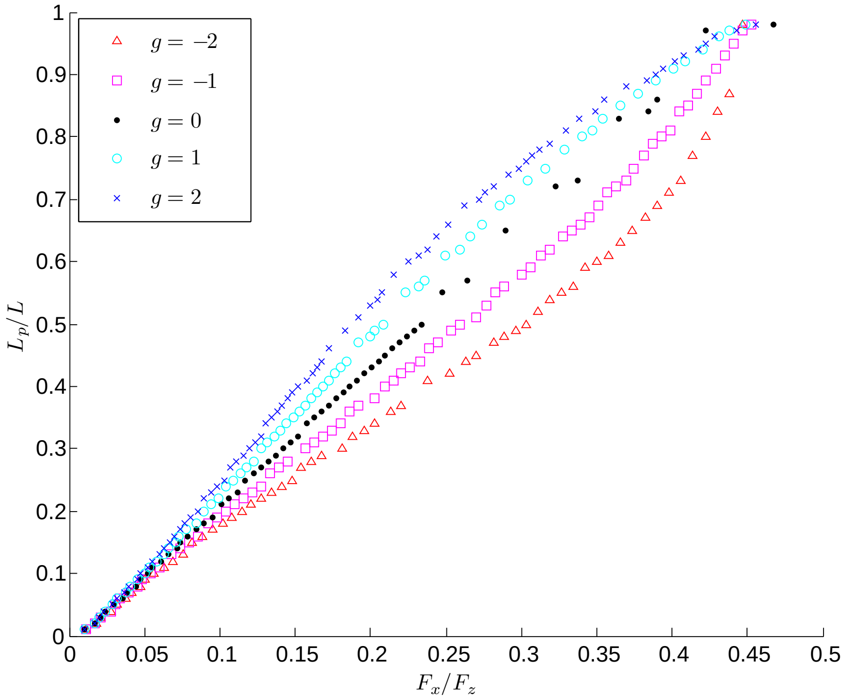

Figure 3.8: Precursor lengths L_p/L as a function of the tangential load F_x for different values of the torque parameter g.

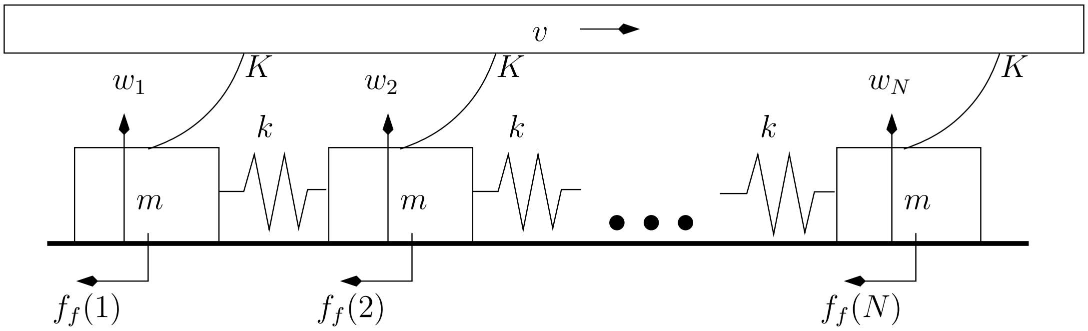

Figure 3.9: *Sketch of the top-driven one-dimensional spring block model. N blocks are connected with linear springs with spring constants k. each local block has a mass $m = M/N$, and an individual normal load w_i. The system is driven from top by a rigid plate, connected to the system with a spring constant K.*

3.2 The top-driven spring block model

We further investigate the effects of changing the driving. Figure (3.9) shows a sketch of a top-driven spring block system. This setup is similar to the classical Burridge-Knopoff model. The system setup is similar to the side-driven model, but each block is connected to a rigid top surface with a spring constant K. The top plate is driven with a constant velocity v. The equations of motion are slightly changed due to the different driving.

Equations of motion

We can find the equations of motion of the system using the change of variables $u_i = x_i - di$. A force $f_x(i)$ from the shear springs works on every block.

$$f_x(i) = K(vt - u_i), \tag{3.46}$$

where K is the shear spring constant, v it the driving speed, and x_i is the local position of block number i. The equations of motion are

$$m\ddot{u}_1 = f_x(i) + k_1(u_2 - u_1) - \eta(\dot{u}_1 - \dot{u}_2) + f_1 \tag{3.47}$$

$$m\ddot{u}_i = f_x(i) + k_{i-1}(u_{i-1} - u_i) + k_i(u_{i+1} - u_i) + \eta(\dot{u}_{i+1} + \dot{u}_{i-1} - 2\dot{u}_i) + f_i \tag{3.48}$$

$$m\ddot{u}_N = f_x(N) + k_{N-1}(u_{N-1} - u_N) - \eta(\dot{u}_{N-1} - \dot{u}_N) + f_N \tag{3.49}$$

η is equal to that of the side-driven model.

3.2.1 Numerical results

Uniform loading

As for the side-driven model we start with the uniform loading case $\theta = g = 0$. Figure (3.10) shows the resulting total tangential force $F_x = \sum_{i=1}^{N} f_i$, and the length of the micro-slip events.

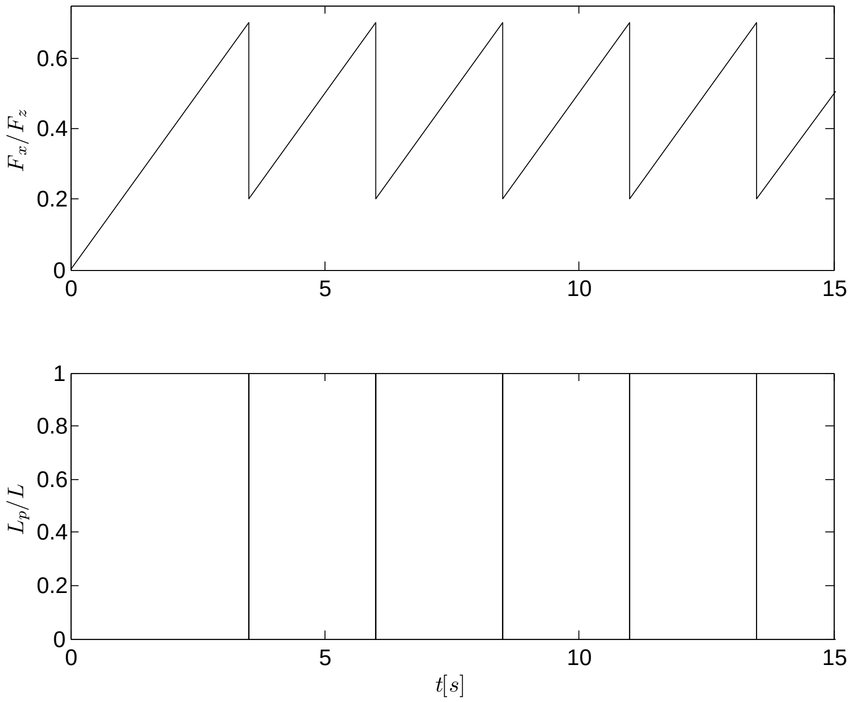

Figure 3.10: *The driving force (top) and the length of the precursors (bottom) as a function of time for the top-driven spring block model with parameters from table (3.1). Since the static friction and the driving force is equal for each block, we get a regime as if we were dealing with only one block.*

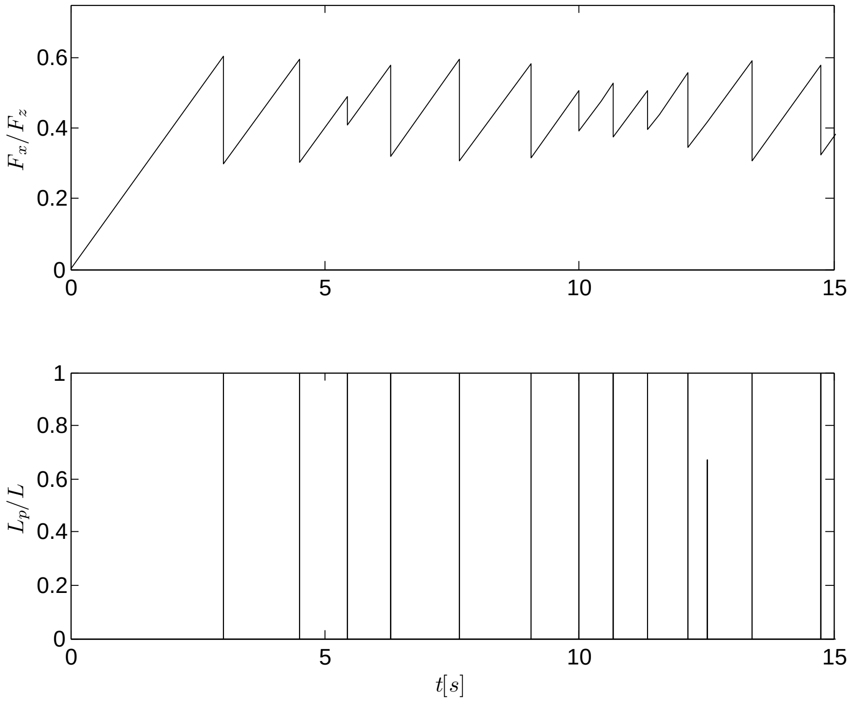

Figure 3.11: *The driving force (top) and the length of the precursors (bottom) as a function of time for the top-driven spring block model with parameters from table (3.1). A a uniform disorder in* μ_s *is introduced:* $\mu_s \in (0.6, 0.8)$.

The driving and the static friction threshold is equal for all blocks, and the material springs remain at their equilibrium length d. The system behaves as if it consisted of only one block. The system enters a state where all events are global and the time interval between events is constant. To prevent this, a disorder in the static friction coefficient is introduced. The static friction constant μ_s is chosen as a uniform distribution so that

$$\mu_s \in (\mu_{s,min}, \mu_{s,max}). \tag{3.50}$$

Figure (3.11) shows the resulting shear force and the event's lengths for $\mu_s = 0.7 \pm 0.1$. Still, there are no precursors, but the behavior of the system is no longer periodical. Because all blocks are subject to a tangential force, the events in the top-driven model tend to be larger than in the side-driven. The shear force increases uniformly, and the first crack will nucleate at lowest value of the static friction threshold. In general, the events may nucleate from anywhere in the material, based on what the stress distribution looks like at the time of the crack arrest. Spikes in the shear force distribution will trigger the next event. The global static friction coefficient is determined by the lowest local static friction coefficient $\mu_s = 0.6$. From figure (3.11) we see that this is indeed the case.

Non-uniform loading and torque

We remove the disorder, and investigate if $g \neq 0$ or $\theta \neq 0$ will give precursors. Figure (3.12) shows the tangential force and the precursor lengths for $\theta = 0.833$. Due to the non-uniform loading, precursors appear.

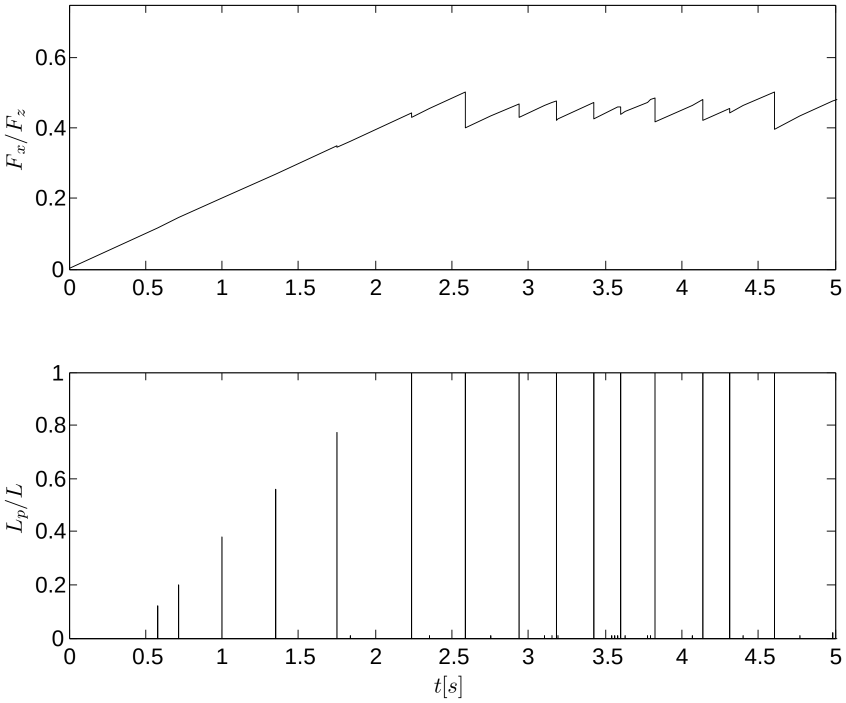

Figure 3.12: The driving force (top) and the length of the precursors (bottom) as a function of time for the top-driven spring block model with parameters from table (3.1). A non-uniform loading $\theta = 0.833$ is introduced.

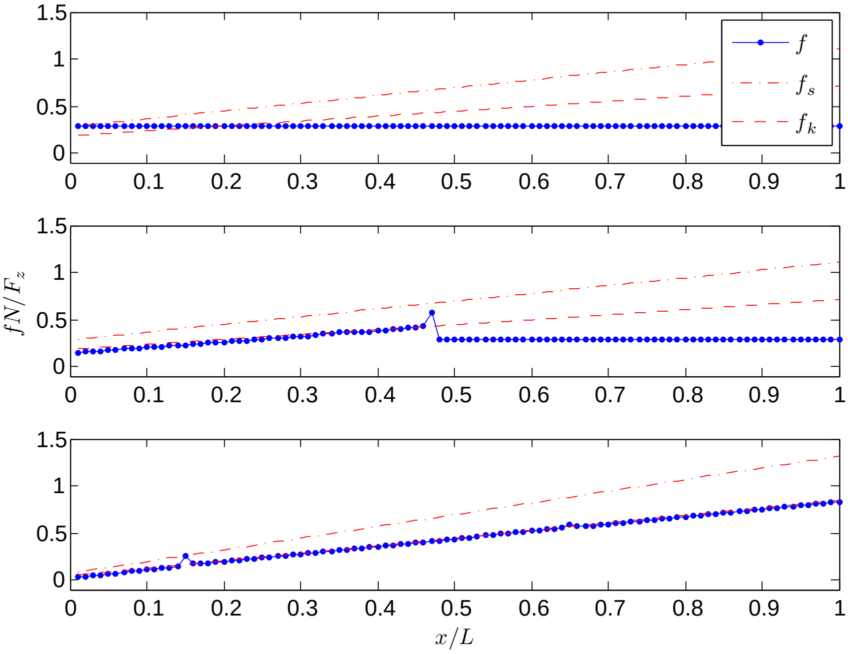

Figure 3.13: *Three different states where the system is at rest: Prior to the first precursor (top), after a few precursors (middle), after the first global event (bottom). Parameters from table (3.1) side-driven with* $\theta = 0$ *and* $g = 2$*. Due to the torque, the local normal force distribution is changed, increasing the friction threshold at the leading edge, and decreasing it at the trailing edge.*

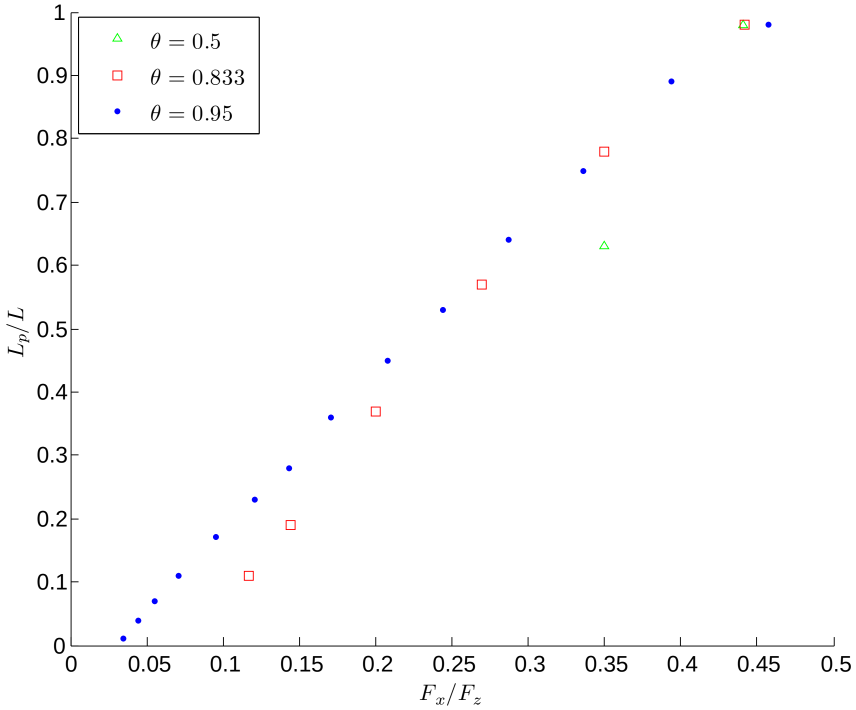

Figure 3.14: *Precursor lengths as a function of the applied tangential load for the top-driven spring block model with parameters from table (3.1). The loading is non-uniform defined by* θ*.*

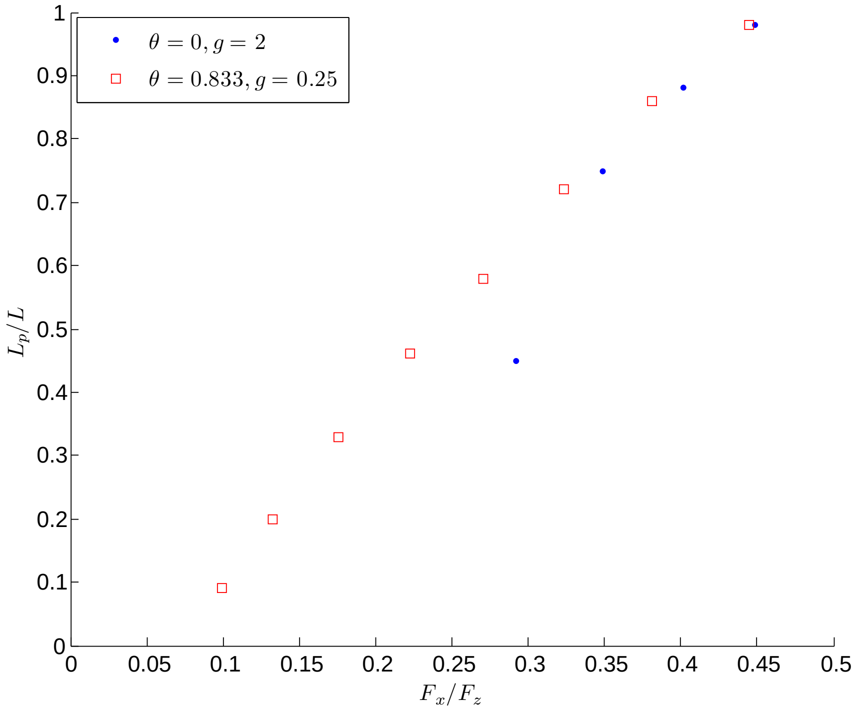

Figure 3.15: *Precursor lengths as a function of the applied tangential load for the top-driven spring block model with parameters from table (3.1). If $\theta \neq 0$ or $g \neq 0$, precursors can be found.*

Since the tangential force F_x in the top-driven model is uniformly increased, results are equal for θ and $-\theta$. The difference when $\theta < 0$, is that the precursors nucleate from the leading edge.

Figure (3.13) demonstrates how a $g \neq 0$ causes precursor events. As the shear force is increased, the friction thresholds are tilted. The built up force when the first event is triggered is not large enough to make the crack propagate all the way through the material. The precursor lengths as a function of the tangential force for various values of θ is plotted in figure (3.14). The number of precursor events increase as θ is increased. Combinations of g and θ is shown in figure (3.15). A larger g results in more precursors since the load at the trailing edge is decreased. $g < 0$ gives precursors that nucleate at the leading edge of the block. $g = 0$ gives no precursors.

A closer look at one event

As for the side-driven model, the dynamics of the events is not trivial. Figure (3.16) shows the velocity distribution in a precursor event for $g = 2$. This event is selected in particular to demonstrate that the crack velocity is not constant. The crack velocity is the slope of the nucleation front. This slope changes in time, giving a non-constant crack velocity.

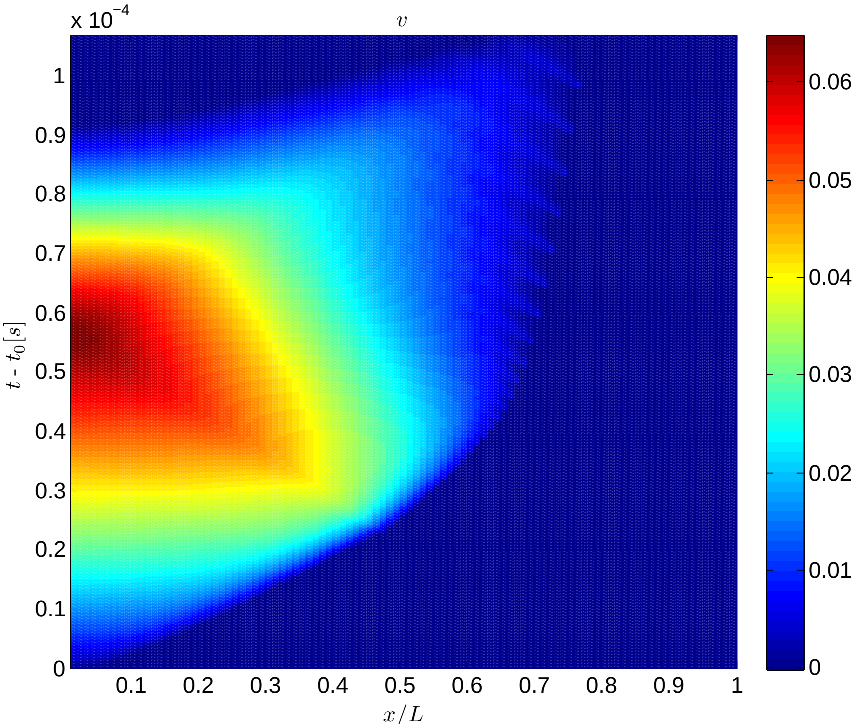

Figure 3.16: *Velocity distribution (m/s) of a precursor event in the top-driven system with parameters from table (3.1) with* $g = 2$*. The crack velocity is not constant.*

3.3 Stress initialization from two-dimensional Poisson effect

When a two-dimensional system is loaded under friction, an initial antisymmetric shear force distribution will be present due to the Poisson effect. This motivated us to add an initial distribution. This can be done by adding an initial displacement field. The results may tell if the two-dimensional effects are important.

The measurements of the shear force distribution done by the Fineberg group [21] inspired us to use the following form on the initial shear force σ_0 on each block.

$$\sigma_0(x) = \frac{\mu_k F_z}{N}\left(\frac{2x - L}{L}\right)^{\varpi}, \tag{3.51}$$

where ϖ is an odd integer. Figure (3.17) shows the resulting precursors for various ϖ. The initial shear force distribution is important to the behavior, and the precursor lengths are closer to experimental observations when an antisymmetric initial shear force distribution is implemented. The initial distribution is determined by the Poisson ratio, and is a purely two-dimensional effect. In order to reproduce experimental results [15], a two-dimensional spring block model is needed. A two-dimensional spring block model is part of the master thesis of Jørgen Trømborg [51].

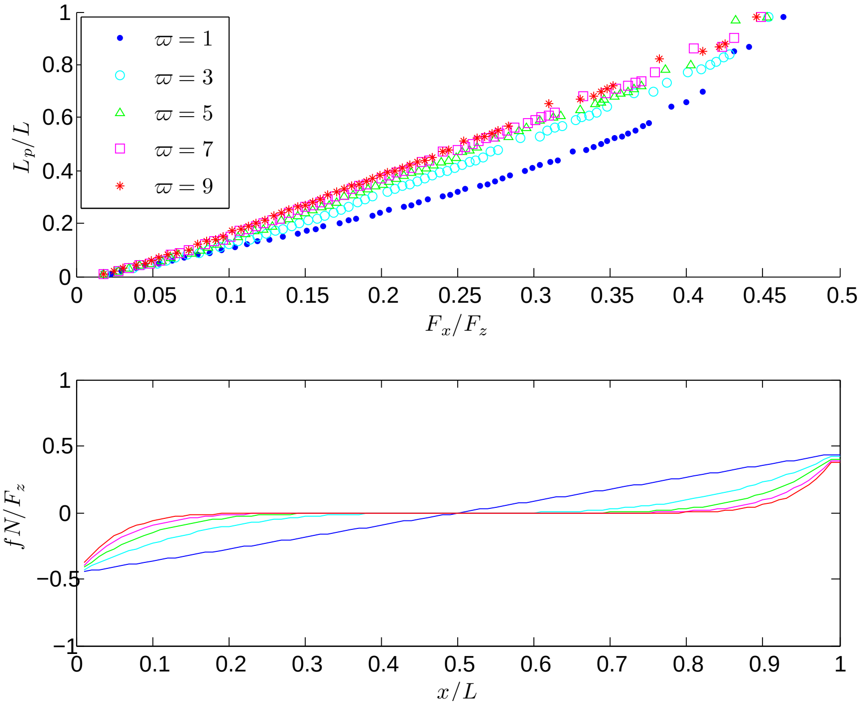

Figure 3.17: *Precursor lengths (top) for different initial shear force distributions (bottom) given by equation (3.51) for the side-driven spring block model with $\theta = g = 0$. The initial stress distribution is important to the precursor lengths.*

3.4 Analytical prediction for precursor lengths

When studying the force distribution, we find that the behavior is similar for all g and θ as long as $K \ll k$. The force on blocks that have been part of an event equals the dynamic friction force when the system is at rest, with a spike at the edge of the crack. With a simple geometrical argument, we can find an analytical solution to the precursor length in the one-dimensional spring block model.

Figure (3.18) shows the main idea of the argument for the top-driven model. It is similar to figure (3.13). When an event is triggered, the blocks involved end up at the dynamic friction threshold f_k. Assuming that the spike at the edge of the crack can be neglected, and that $K \ll k$ so that all forces on a block are transferred to its neighbors, we get the scenario in the figure. $K \ll k$ means that the driving spring only set up the force prior to an event, and does not affect the dynamics of the event. The integral over the forces above the friction threshold is conserved, and transferred to its neighbors so that the local shear force ends up at the dynamic friction level.

3.4.1 side-driven model

The argument is also valid in the side-driven model. We assume that a stress pulse is sent trough a discrete system from the edge. The system has an initial stress distribution $\sigma_0(x)$. We further assume that the crack propagates throught the material and leaves behind a local force equal to the dynamic friction force $f_k(x)$. The crack will propagate

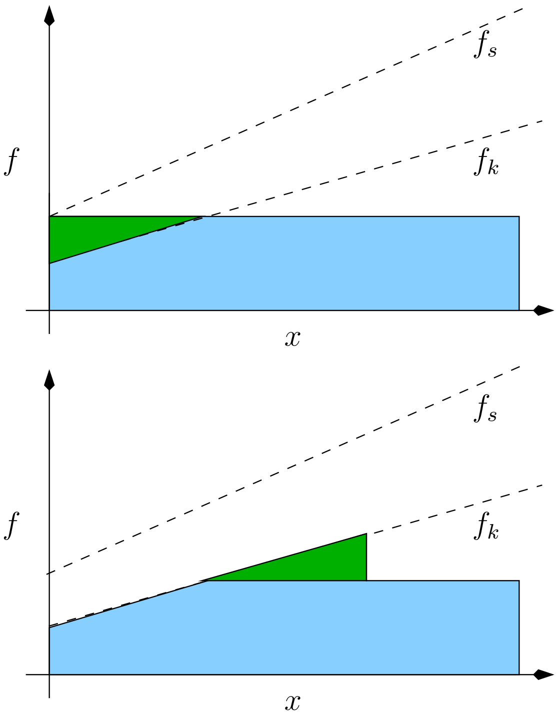

Figure 3.18: *Geometrical argument for the precursor lengths in the one-dimensional top-driven spring block model. The force distribution prior to slip (top) and the force distribution after slip (bottom). The filled areas are conserved. The prediction assumes that the spike at the edge of the crack can be neglected, and that the driving spring constant $K \ll k$.*

until the forces that are distributed at the dynamic friction level, and the next block does not reach the static friction force. A peak in the stress at the edge of the crack will be present. The tangential force as a function of the length of a precursor from is then given by

$$F_x = \mu_k \sum_{i=1}^{N} w_{\text{normal}}(i) + w_{\text{torque}}(i) - \sigma_0(i) + f_p(x_{tip}). \tag{3.52}$$

Where σ_0 is the initial force distribution, and $f_p(x_{tip}) \leq f_s(x)$ is the stress peak at the edge of the crack. If the system size is large, we can neglect this stress peak, and we find that

$$F_x = \mu_k \sum_{i=1}^{N} w_{\text{normal}}(i) + w_{\text{torque}} - \sigma_0(i), \tag{3.53}$$

where w_{torque} depends on F_x. Assuming that $K << k$ results in a torque term w_{torque} that does not change during an event, since F_x will be close constant. Solving for F_x gives

$$F_x = \frac{\mu_k \sum_{i=1}^{N} w_{\text{normal}}(i) - \sigma_0(i)}{1 - \mu_k g/N \sum_{i=1}^{N}(2i - N - 1)/(N - 1)} \tag{3.54}$$

This relation predicts the precursors in a one-dimensional system with kinetic friction force $f_k(x)$ and initial stress $\sigma_0(x)$. The static friction force does not appear. Using equation (3.35) for the time skipping, the time of the next event and its amplitude can be found. Figure (3.19) and (3.20) show analytical predictions of precursor lengths in the side-driven model.

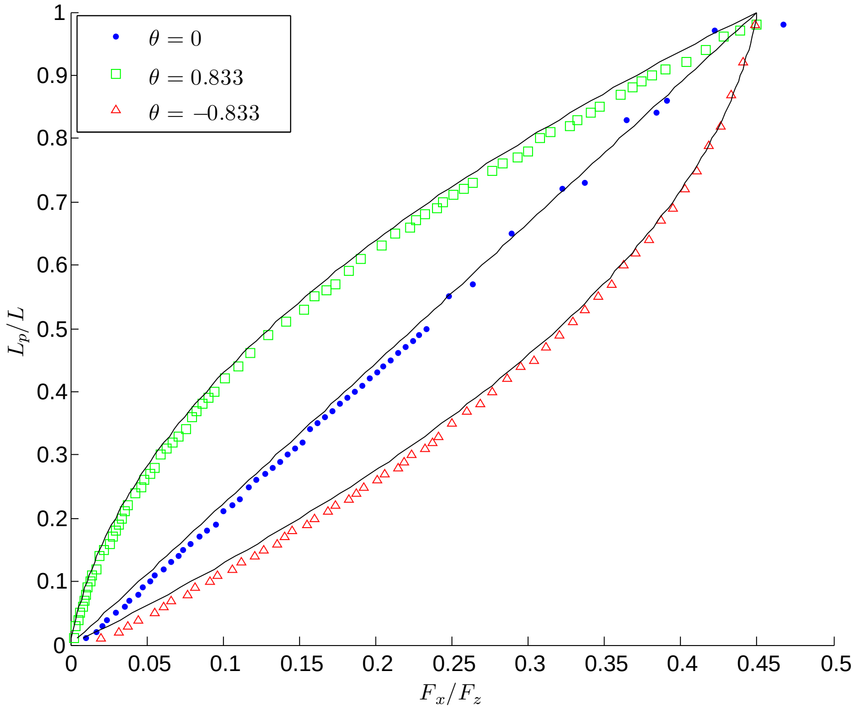

Figure 3.19: *Figure (3.6) with analytical predictions: The propagation length of the precursors as a function of the applied force F_x for three values of θ giving a non-uniform loading.*

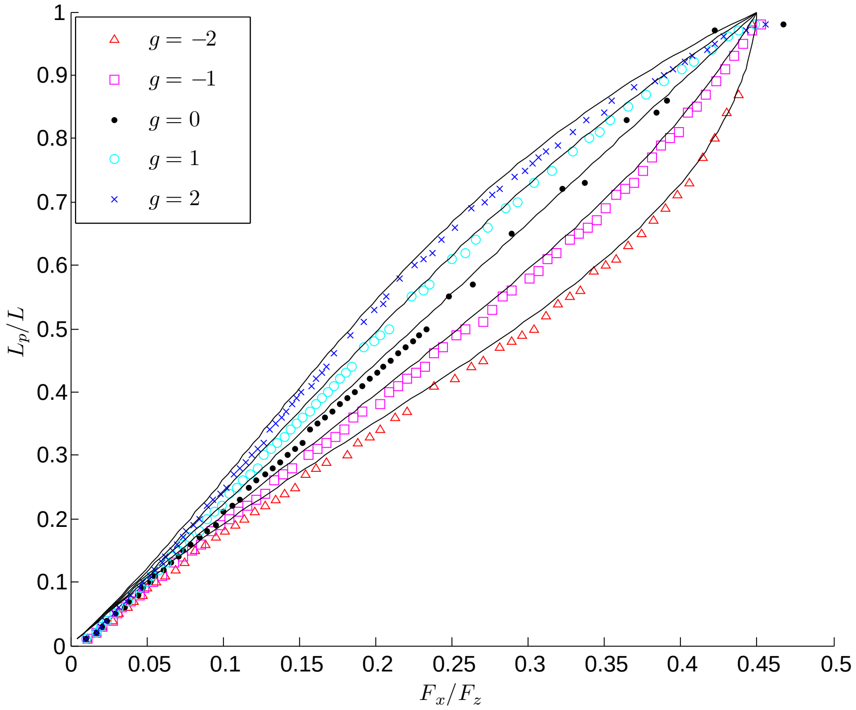

Figure 3.20: *Figure (3.8) with analytical predictions: Precursor lengths L_p/L as a function of the tangential load F_x for different values of the torque parameter g.*

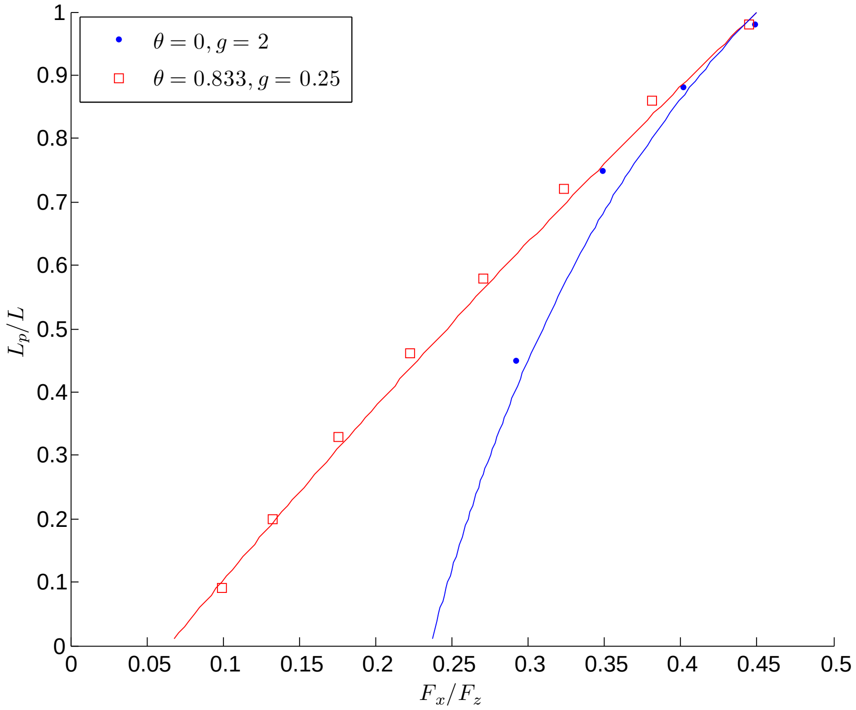

Figure 3.21: *Figure (3.21) with analytical predictions: Precursor lengths as a function of the applied tangential load for the top-driven spring block model with parameters from table (3.1). If $\theta \neq 0$ or $g \neq 0$, precursors can be found.*

3.4.2 top-driven model

We can perform the same analysis for a top-driven model. In this case, the stress will increase uniformly through the material until we get slip. We still assume that the local forces equal the dynamic friction force after an event. A force $f_x(i)$ is added to each block in the system. At the start of a slip, the shear force distribution is

$$\sigma(x) = \sigma_0(x) + f_x(x), \tag{3.55}$$

The crack will propagate until the added forces are at the dynamic friction level $f_k(x)$. If we assume that the crack propagates from the trailing edge starting with a small pulse, we have that

$$F_x = \mu_k \sum_{i=1}^{N} (w_{\text{normal}}(i) + w_{\text{torque}}(i) - \sigma_0(i)), \tag{3.56}$$

neglecting the stress peak at the edge. We then find

$$F_x = N \frac{\sum_{i=1}^{N} (w_{\text{normal}}(i) - \sigma_0(i))}{N - \mu_k g \sum_{i=1}^{N} (2i - N - 1)/(N-1)}. \tag{3.57}$$

Using equations (3.54) and (3.57) we can predict the precursor lengths of any one-dimensional system with Amontons-Coulomb friction under the assumption that $k << K$. In the top-driven system however, there are often few precursors if the loading is close to uniform and the torque effect is small. Figure(3.21) shows the analytical prediction of precursors in the top-driven model.

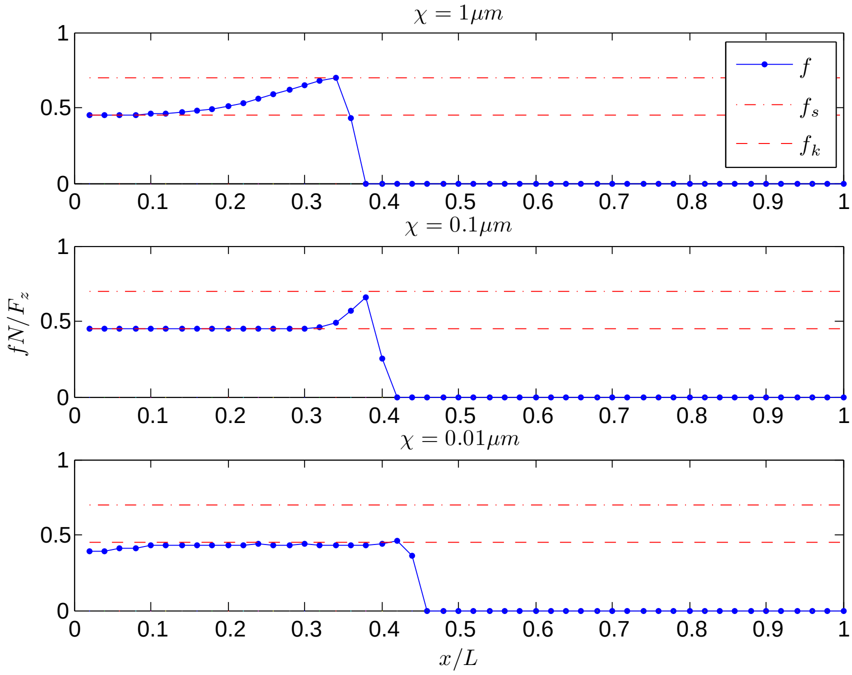

Figure 3.22: *Force distribution at* $t = 1s$ *with slip-weakening friction with parameters* $N = 50$, $dt = 1 \times 10^{-6}$ *and* $\Delta\mu = 0$ *for characteristic slip lengths* $\chi = 1\mu m$ *(top),* $\chi = 0.1\mu m$ *(middle) and* $\chi = 0.01\mu m$ *(bottom).*

3.5 Changing the local friction law: Slip-weakening friction

In order to test the robustness of the model to changes in the local friction law, we introduce a slip-dependent μ_k as suggested in [52]. This is motivated by micro-asperities in contact χ.

$$\mu_k(x) = (\mu_s - \mu_{k,0} - \Delta\mu)e^{-\Delta x_{slip}/\chi} + \mu_{k,0} \tag{3.58}$$

where χ is the tunable characteristic slip length, Δx_{slip} is the slip length during a single event of the block, and $\Delta\mu$ is a discontinuity in the friction coefficient. Figure (3.22) shows the shear force distribution at $t = 1s$ for various values of χ. When $\Delta\mu = 0$ and $\chi > 0.01\mu m$, there is only one slow global event. For small χ, the local friction law is close to Amontons-Coulomb friction. If a small discontinuity $\Delta\mu = 0.01$ is introduced, the system behavior changes. This is illustrated in figure (3.23) and (3.24). Shear force build up until a critical force is reached, where a large event occurs. The critical force depends on χ.

The analytical prediction made with Amontons-Coulomb friction do not work with a slip-weakening friction law. Instead, we make a prediction using both the dynamic friction coefficient and the static friction coefficient. At the start of an event, the force on a local block ends up close to the static friction level because the slip distance compared to χ is small, and mu_k is close to μ_s. When the system builds up enough forces a larger event occurs, where the slip distances are large compared to χ. The system then behaves as if the local friction law was that of Amontons-Coulomb, and the forces end

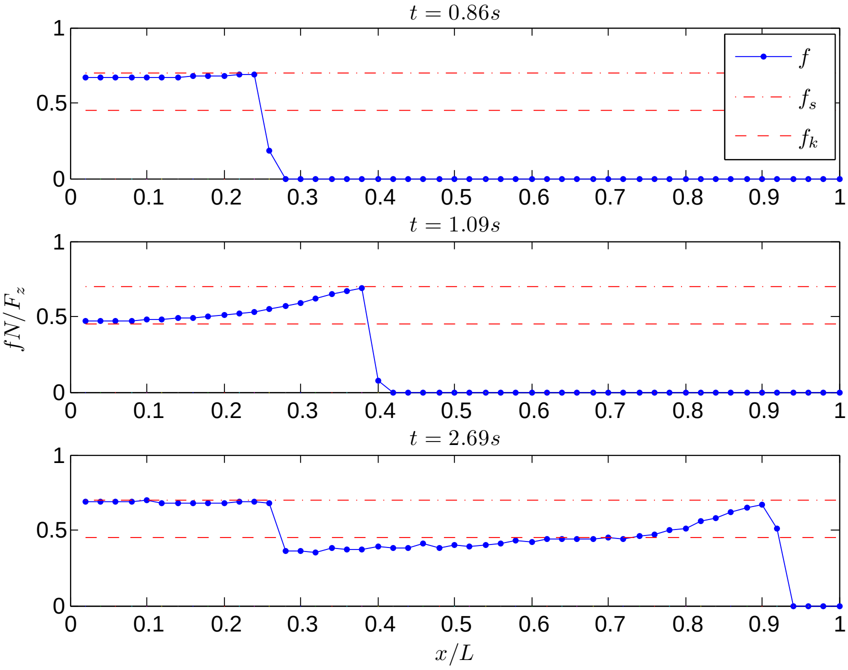

Figure 3.23: *Force distribution at* $t = 0.86s$ *(top),* $t = 1.09s$ *(middle) and* $t = 2.69s$ *(bottom) with slip-weakening friction with parameters* $\chi = 1\mu m$*,* $N = 50$*,* $dt = 1 \times 10^{-6}$ *and* $\Delta\mu = 0.01$*.*

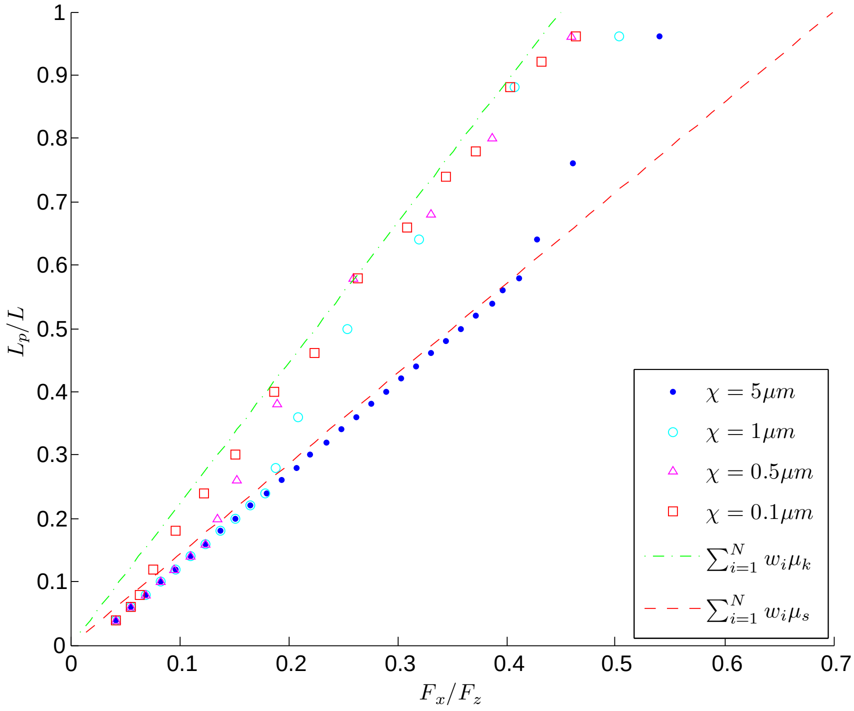

Figure 3.24: *Precursor lengths for various* χ *with parameters* $N = 50$*,* $dt = 1 \times 10^{-6}$ *and* $\Delta\mu = 0.01$*. Force builds up until a larger event at a critical point.*

up on the dynamic friction level. From figure (3.24) we see that this transition occurs at a given driving force F_x/F_z. The transition point changes with χ. Even though this behavior is somewhat different from the Amontons-Coulomb behavior, for small χ, the effect vanishes, and we get Amontons-Coulomb friction. This suggests that the local friction law is important to the overall behavior of the system.

Various rate and state dependent friction laws could also be introduced [5, 8]. The time strengthening static friction

$$\mu_s(t) = \frac{\mu_{s,0} - \mu_k}{log(t_c\beta + 1)} log(\beta \Delta t_{slip} + 1) + \mu_k, \tag{3.59}$$

where β, and t_c are tunable parameters that determine the characteristic length, the curvature of the logarithm, and the characteristic time, as well as a velocity dependent friction

$$mu_k(v) = \alpha_v + \beta_v v. \tag{3.60}$$

In the velocity dependent friction, a local block stops when its velocity is below a critical velocity v_c.

3.6 Discussion

The one-dimensional spring block model has been extensively studied in friction, but often with a statistical approach. In this chapter I have tested the model in a deterministic way using a time integration algorithm.

For an initial uniform load, the measured precursor lengths are not fully consistent with experimental data [15], and by adding a linear torque effect, the differences are increased further. An initial shear force distribution motivated by the Poisson ratio enables us to get closer to these results, and suggests that the underlying shear force distribution is important to the dynamics. This observation leads us to believe that a two-dimensional elastic model should be introduced. This is part of the thesis by Jørgen Trømborg, finishing in 2011 [51]. He found that adding a second dimension can explain some of the features in the experimental observations. One point that is interesting is the fact that the events in the one-dimensional spring block model can be predicted accurately, both in time and in space. Since the precursors can be predicted analytically given the initial force distribution, one could in fact find the initial distribution needed to reproduce experimental results if one had access to the experimental data. However, this would not be the best way to address these differences, since the introduction of the initial shear force distribution was motivated by two-dimensional effects. It remains to be seen if good predictions can be made in a two-dimensional system. Crack velocities and different local laws is further studied in the thesis of Davis Skålid Amundsen [50].

Since local forces are only transferred to the closest neighbor blocks, some two-dimensional effects will obviously vanish. The underlying shear and normal force distributions are important. This has also been suggested by Ben-David et. al [21]. In two dimensions these force distributions are not constant, and we expect some effects to arise because of this.

The work done in this thesis contributed to an article on the transistion from static to dynamic friction in two dimensions [53]. We found that by adding a second dimension to the spring block model, some of the main features of the experimental observations are actually reproduced.

We also find that the underlying friction laws change the dynamics of the system. In order to understand some of the underlying local laws of friction, a two-dimensional system is introduced.

Part III

A MICROSCOPIC FRICTION MODEL

In the mesoscopic model assumptions for the local inter-facial behavior were made. For imposed displacements, the stresses required in the mesoscale model are actually results from microscopic calculations. It is crucial for the system behavior at the mesoscale to model these inter-facial behavior laws correctly. In this part I will try to determine these laws by modeling the micro-scale topography of a thin surface layer. The shear stiffness of the surface layer is important in order to understand the global behavior of systems where friction forces apply. An important question is how the roughness and the pressure put on of a surface will affect the stiffness of the surface layer. Generally, the surface layer is a lot softer than the bulk of a material.

In order to understand the behavior of a large surface layer, a single asperity is first introduced, and the tangential loading curve is measured. Based on these results a theoretical approach to the tangential loading curve (as a measure of the stiffness) of a rough surface is made. Finally, a rough surface is modeled and compared to the theory.

Before introducing the numerical models, an introduction to theory of elasticity and contact mechanics is given, including recent theories for the normal and shear stiffness of rough surfaces.

Chapter 4

Theory of elasticity and contact mechanics

Before establishing the numerical models, a brief introduction to elasticity theory and contact mechanics is given. This chapter closely follows Timoschenko and Goodier's 'Theory of elasticity'[54], and Johnson's 'Contact mechanics'[4]. I will establish the framework used to solve problems in contact mechanics, and show some of the solutions in Hertz and Cattaneo-Mindlin theory without going into details of the calculations. The last section of this chapter is an overview of scaling theories on rough surfaces.

4.1 Theory of elasticity

We start with the theory of elasticity, and define the elastic half-space and the elastic equations.

4.1.1 The elastic half-space

When solving elastic contact mechanics, the boundary conditions are important. It is useful to introduce the elastic half-space to avoid problems that might turn up due to undefined boundary conditions. Each body is considered as a semi-infinite elastic solid bounded by a plane surface. This assumes that the contact size is much smaller than the body dimensions and radius of curvature. The result is that the stress is located close to the surface, and the solutions are not dependent on the shape of the object far from the surface.

4.1.2 The elastic equations

We define the shear component of the stress along a general direction n τ_n, the normal component of the stress parallel to n σ_n, elongations u_n, unit elongations ϵ_n, and unit shearing strain along the plane $n_1 n_2$ $\gamma_{n_1 n_2}$. The bar denotes the value at the surface interface. The strains are related to the displacements through the following equations:

$$\epsilon_x = \frac{\partial u_x}{\partial x}, \tag{4.1}$$

$$\epsilon_y = \frac{\partial u_y}{\partial y}, \tag{4.2}$$

and

$$\gamma_{xy} = \frac{\partial u_x}{\partial y} + \frac{\partial u_y}{\partial x}. \tag{4.3}$$

4.1.3 Hooke's law

Hooke's law relates the stress and the strain components. We imagine a small parallelepiped element subject to normal stress distributed uniformly at two opposite sides. The unit elongation of an element is

$$\epsilon_x = \frac{\sigma_x}{E}, \tag{4.4}$$

where E is Young's modulus of elasticity. The unit elongation in the y-direction is

$$\epsilon_y = \epsilon_z = -\nu\frac{\sigma_x}{E}, \tag{4.5}$$

where ν is the Poisson ratio. If the element is subjected to normal stress at all sides, the resulting strains are superpositions of the above result.

$$\epsilon_x = \frac{1}{E}\left(\sigma_x - \nu(\sigma_y + \sigma_z)\right). \tag{4.6}$$

$$\epsilon_y = \frac{1}{E}\left(\sigma_y - \nu(\sigma_x + \sigma_z)\right). \tag{4.7}$$

$$\epsilon_z = \frac{1}{E}\left(\sigma_z - \nu(\sigma_x + \sigma_y)\right). \tag{4.8}$$

4.1.4 Shear stress and strain

The shear stress and strain can be found in a similar manner. We define the shear modulus

$$G = \frac{E}{2(1+\nu)}, \tag{4.9}$$

and end up with the following relations:

$$\gamma_{xy} = \frac{\tau_{xy}}{G} \tag{4.10}$$

$$\gamma_{xz} = \frac{\tau_{xz}}{G} \tag{4.11}$$

$$\gamma_{yz} = \frac{\tau_{yz}}{G}. \tag{4.12}$$

4.1.5 Plane stress and plane strain

If assuming plane stress, a thin plate is loaded at the boundaries parallel to its plane, and the forces are distributed uniformly over its thickness. The conditions of plane stress are

$$\sigma_z = \tau_{xz} = \tau_{yz} = 0. \tag{4.13}$$

The stress is then determined by σ_x, σ_y and τ_{xy} only.

If assuming plane strain, the dimension in the z-direction is very large, so that there are no displacements at the edges or the midsection (due to symmetry). An example is a cylinder which is long compared to its radius. The displacement $u_z = 0$. Due to the symmetry, the result holds at every cross-section. The components of strain are independent of the coordinate z. This gives us the conditions of plane strain

$$\gamma_{xz} = \gamma_{yz} = \epsilon_z = 0. \tag{4.14}$$

The stress σ_z during plane strain is found using Hooke's law

$$\sigma_z = \nu(\sigma_x + \sigma_y). \tag{4.15}$$

This stress can be found using σ_x and σ_y. In chapter 6, we will perform calculations on a circle. Assuming plane strain this is actually a cylinder, and σ_z can be calculated using equation (4.15).

4.1.6 Equilibrium conditions

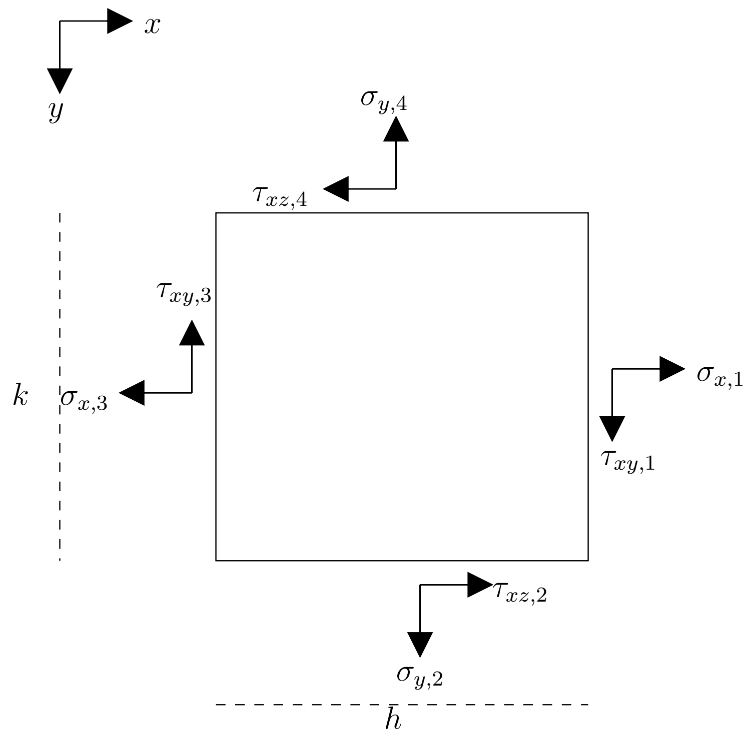

Figure 4.1: *At equilibrium, the sum of the forces at an element has to be zero.*

At equilibrium, the total forces in all directions have to be zero. That is the case if the following equation in the x-direction is satisfied

$$\frac{\sigma_{x,1} - \sigma_{x,3}}{h} + \frac{\tau_{xz,2} - \tau_{xz,4}}{k} = 0. \tag{4.16}$$

If we let h and k be infinitesimal, this is reduced to a differential equation

$$\frac{\partial \sigma_x}{\partial x} + \frac{\partial \tau_{xy}}{\partial y} = 0. \tag{4.17}$$

We find a similar expression in the y-direction

$$\frac{\partial \sigma_y}{\partial y} + \frac{\partial \tau_{xy}}{\partial x} = 0. \tag{4.18}$$

4.1.7 Compatibility conditions

The three strain components ϵ_x, ϵ_y and γ_{xz} cannot be chosen arbitrarily. Differentiating equations (4.1), (4.2) and (4.3), we find the relation

$$\frac{\partial^2 \epsilon_x}{\partial y^2} + \frac{\partial^2 \epsilon_y}{\partial x^2} = \frac{\partial^2 \gamma_{xy}}{\partial x \partial y}. \tag{4.19}$$

This is the condition of compatibility, which can be found in various forms, for example by using Hooke's law.

4.1.8 The stress function

The solution of an elastic problem is found using the equilibrium equations, the condition of compatibility and boundary conditions. This is usually done using a stress function Ψ, which is a help function that satisfies the given equations. We define the stress function

$$\sigma_x = \frac{\partial^2 \Psi}{\partial y^2}, \sigma_y = \frac{\partial^2 \Psi}{\partial x^2}, \tau_{xy} = -\frac{\partial^2 \Psi}{\partial x \partial y}, \tag{4.20}$$

where Ψ satisfies the bi-harmonic equation

$$(\frac{\partial^2}{\partial x^2} + \frac{\partial^2}{\partial y^2})(\frac{\partial^2 \Psi}{\partial x^2} + \frac{\partial^2 \Psi}{\partial y^2}) = 0. \tag{4.21}$$

4.1.9 Polar coordinates

The equations in this section may be useful in polar coordinates for some problems. In two dimensions we define the angle θ, and the radius r. We find

$$\epsilon_r = \frac{\partial u_r}{\partial r}, \tag{4.22}$$

$$\epsilon_\theta = \frac{u_r}{r} \frac{1}{r} \frac{\partial u_\theta}{\partial \theta}, \tag{4.23}$$

$$\gamma_{r\theta} = \frac{1}{r}\frac{\partial u_r}{\partial \theta} + \frac{\partial u_\theta}{\partial r} - \frac{u_\theta}{r}, \tag{4.24}$$

$$\sigma_x = \sigma_r \sin^2\theta, \tag{4.25}$$

$$\sigma_y = \sigma_r \cos^2\theta, \tag{4.26}$$

$$\tau_{xy} = \sigma_r \sin\theta\cos\theta. \tag{4.27}$$

The stress function and the bi-harmonic equation is given by

$$\sigma_r = \frac{1}{r}\frac{\partial \Psi}{\partial r} + \frac{1}{r^2}\frac{\partial^2\Psi}{\partial \theta^2}, \tag{4.28}$$

$$\sigma_\theta = \frac{\partial^2\Psi}{\partial r^2}, \tag{4.29}$$

$$\tau_{r\theta} = -\frac{\partial}{\partial r}(\frac{1}{r}\frac{\partial\Psi}{\partial\theta}). \tag{4.30}$$

$$(\frac{\partial^2}{\partial r^2} + \frac{1}{r}\frac{\partial}{\partial r} + \frac{1}{r^2}\frac{\partial^2}{\partial\theta^2})(\frac{\partial^2\Psi}{\partial r^2} + \frac{1}{r}\frac{\partial\Psi}{\partial r} + \frac{1}{r^2}\frac{\partial^2\Psi}{\partial\theta^2}) = 0. \tag{4.31}$$

4.2 Contact mechanics

4.2.1 Concentrated normal force

We start by calculating the normal stresses produced by a point-source force with magnitude P as shown in figure (4.2). The boundary conditions are zero stress at infinity.

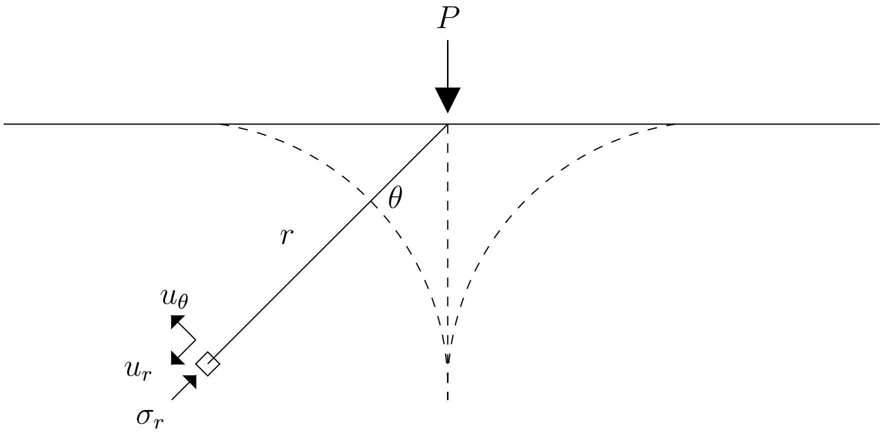

Figure 4.2: *Concentrated normal force. The dashed lines are the contours of constant stress.*

Using polar coordinates, the bi-harmonic equation has the solution

$$\Psi(r,\theta) = Br\theta\sin\theta, \tag{4.32}$$

which satisfies the boundary conditions. Using the stress components from equations (4.28), (4.29) and (4.30) we find

$$\sigma_r = \frac{2B}{r}\cos\theta \tag{4.33}$$

$$\sigma_\theta = 0 \tag{4.34}$$

$$\tau_{r\theta} = 0. \tag{4.35}$$

To find the complete solution we need the value of the constant B. We calculate the stress on a semi-circle with radius r.

$$-P = \int_{-\pi/2}^{\pi/2} r\sigma_r \cos\theta = \int_0^{\pi/2} 4B\cos^2\theta d\theta = B\pi. \tag{4.36}$$

We can now find σ_x, σ_y and τ_{xy} by substituting back to Cartesian coordinates

$$\sigma_x = -\frac{2P}{\pi}\frac{x^2 y}{(x^2+y^2)^2} \tag{4.37}$$

$$\sigma_y = -\frac{2P}{\pi}\frac{y^3}{(x^2+y^2)^2} \tag{4.38}$$

$$\tau_{xy} = -\frac{2P}{\pi}\frac{xy^2}{(x^2+y^2)^2}. \tag{4.39}$$

4.2.2 Concentrated tangential force

The distribution of stress due to a concentrated tangential force Q is similar to that of the normal force, but rotated $\pi/2$. Changing θ gives us the same integral as for P.

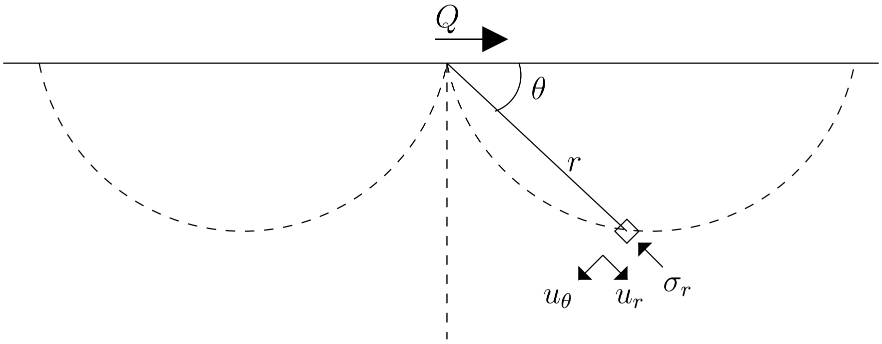

Figure 4.3: *Concentrated tangential force. The dashed lines are the contours of constant stress.*

$$-Q = \int_0^{\pi} r\sigma_r \cos\theta = B\pi. \tag{4.40}$$

We find

$$\sigma_r = -\frac{2Q}{\pi r}\cos\theta, \tag{4.41}$$

and

$$\sigma_\theta = \tau_{r\theta} = 0. \tag{4.42}$$

The Cartesian stresses are found in a similar manner as for the normal force.

$$\sigma_x = -\frac{2Q}{\pi}\frac{x^2 y}{(x^2+y^2)^2} \tag{4.43}$$

$$\sigma_y = -\frac{2Q}{\pi}\frac{y^3}{(x^2+y^2)^2} \tag{4.44}$$

$$\tau_{xy} = -\frac{2Q}{\pi}\frac{xy^2}{(x^2+y^2)^2}. \tag{4.45}$$

4.2.3 Distributed normal and tangential force

The stress due to distributions of normal and tangential force can be found by superposition. In an interval $(-a/2, a/2)$ we have a normal pressure $p(x)$, and a tangential traction distribution $q(x)$. If we change coordinate system from x to $(x-s)$ and integrate we find

$$\sigma_x = -\frac{2y}{\pi}\int_{-a/2}^{a/2}\frac{p(s)(x-s)^2ds}{((x-s)^2+y^2)^2} - \frac{2}{\pi}\int_{-a/2}^{a/2}\frac{q(s)(x-s)^3ds}{((x-s)^2+y^2)^2}, \tag{4.46}$$

$$\sigma_y = -\frac{2y^3}{\pi}\int_{-a/2}^{a/2}\frac{p(s)ds}{((x-s)^2+y^2)^2} - \frac{2y^2}{\pi}\int_{-a/2}^{a/2}\frac{q(s)(x-s)ds}{((x-s)^2+y^2)^2}, \tag{4.47}$$

$$\tau_{xy} = -\frac{2y^2}{\pi}\int_{-a/2}^{a/2}\frac{p(s)(x-s)ds}{((x-s)^2+y^2)^2} - \frac{2y}{\pi}\int_{-a/2}^{a/2}\frac{q(s)(x-s)^2ds}{((x-s)^2+y^2)^2}. \tag{4.48}$$

Solutions to the equations above are widely studied, and are divided into five different classes based on the boundary conditions. These equations can be written in terms of the displacements along the surface. We will make use of the displacement gradients given by

$$\frac{\partial \bar{u}_x}{\partial x} = -\frac{(1-2\nu)(1+\nu)}{E}p(x) - \frac{2(1-\nu^2)}{\pi E}\int_{-a/2}^{a/2}\frac{q(s)}{x-s}ds \tag{4.49}$$

and

$$\frac{\partial \bar{u}_y}{\partial x} = -\frac{2(1-\nu^2)}{\pi E}\int_{-a/2}^{a/2}\frac{p(s)}{x-s}ds + \frac{(1-2\nu)(1+\nu)}{E}q(x). \tag{4.50}$$

4.3 Two-dimensional contact of cylinders: Hertz theory of elastic contact

To solve the contact problem, Hertz defined the separation between local points on two surfaces. The separation between two points on unloaded cylinder surfaces is

$$\delta = y_1 - y_2 = \frac{1}{2}\frac{1}{R}x^2, \tag{4.51}$$

where

$$R \equiv (\frac{1}{R_1} + \frac{1}{R_2}). \tag{4.52}$$

The vertical displacements at the surface are

$$\bar{u}_{y1} + \bar{u}_{y2}\begin{cases} = \delta - \frac{1}{2}\frac{1}{R}x^2, & |x| < a/2 \\ > \delta - \frac{1}{2}\frac{1}{R}x^2, & |x| > a/2 \end{cases} \tag{4.53}$$

whereas displacement gradients are

$$\frac{\partial \bar{u}_{y_1}}{\partial x} + \frac{\partial \bar{u}_{y_2}}{\partial x} = -\frac{x}{R}. \tag{4.54}$$

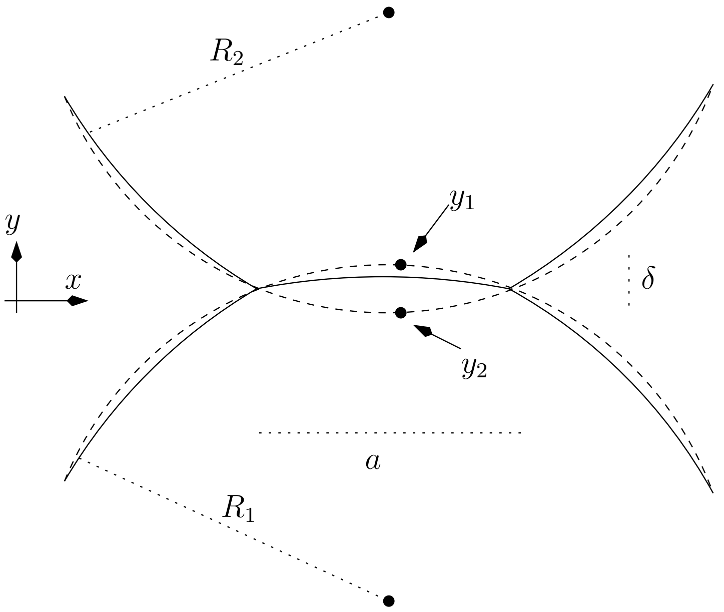

Figure 4.4: *Compression of two cylinders in elastic half-space.*

In two dimensions we need the displacement gradients because the displacement of a point depends on the displacement of a reference point that is not uniquely defined. For this reason, some calculations that can be carried out in the three-dimensional case can not be carried out in two dimensions. Using equation (4.50) with $q(x) = 0$ and solving for $p(x)$, Hertz found

$$p(x) = -\frac{\pi E^*}{2R}\frac{x^2-(a/2)^2}{\pi\sqrt{(a/2)^2-x^2}}+\frac{P}{\pi\sqrt{(a/2)^2-x^2}}, \tag{4.55}$$

where

$$E^* \equiv (\frac{1-\nu_1^2}{E_1}+\frac{1-\nu_2^2}{E_2})^{-1}. \tag{4.56}$$

Applying that the pressure has to be greater than zero, and the fact that contact does not occur outside the loaded area, we find expressions for the pressure distribution, and the surface area as functions of the total pressure applied.

$$a = \sqrt{\frac{4PR}{\pi E^*}}. \tag{4.57}$$

and

$$p(x) = \frac{2P}{\pi(a/2)^2}\sqrt{(a/2)^2-x^2} \tag{4.58}$$

4.4 Sliding of cylinders: The Cattaneo-Mindlin theory

We proceed to find the pressure distribution $p(x)$ and the traction distribution $q(x)$ when a tangential load Q is applied at the interface between two cylinders. We start with the case of infinite friction at the interface, so that the relative displacements $\bar{u}_{x_1} - u_{x_2}$ can be taken as constants in $(-a/2, a/2)$. The solution is

$$q(x) = \frac{Q}{\pi((a/2)^2 - x^2)} \tag{4.59}$$

Figure (4.5) shows a three-dimensional sphere as seen from above. When applying a tangential load Q with a finite friction coefficient, partial slip will occur at the edges of contact since the tangential traction in the full stick case diverges at the edges, and the pressure is small. A stick zone with size c is present at the center of the contact. When the cylinders are sliding

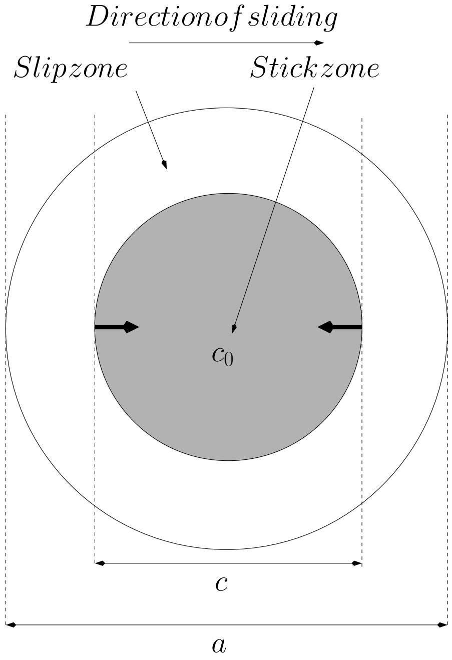

Figure 4.5: *A three-dimensional asperity as seen from above. As the shear force, Q, is increased, the size of the stick zone is reduced. An asymmetry is also produced, and is measured as the position of the center of the stick zone, c_0.*

$$q(x) = \mu_k p(x), \tag{4.60}$$

where μ_k is the dynamic friction coefficient . This gives

$$q_a(x) = \mu_k \frac{2P}{\pi(a/2)^2}\sqrt{(a/2)^2 - x^2}. \tag{4.61}$$

In the stick region $\bar{u}_{x_1} - \bar{u}_{x_2}$ is constant, giving a second term to the tangential traction

$$q_c(x) = -\frac{\mu_k 4cP}{\pi a^2}\sqrt{1 - \frac{x^2}{(c/2)^2}}. \tag{4.62}$$

The total traction is

$$q(x) = q_a(x) + q_c(x) = \frac{\mu_k 4cP}{\pi a}\sqrt{1 - x^2/(a/2)^2}. \tag{4.63}$$

The size of the stick zone c can also be calculated, yielding

$$\frac{c}{a} = \sqrt{1 - \frac{Q}{\mu_k P}}. \tag{4.64}$$

Due to the difficulties with the reference point in two dimensions, the tangential displacement cannot be related to the tangential load. A numerical approach to the Cattaneo-Mindlin theory will be discussed in chapter 6. These results will be different if friction applies during the normal loading. This will produce a large asymmetry in the stick region [55]. This is further discussed in chapter 6.

4.5 Rough surfaces

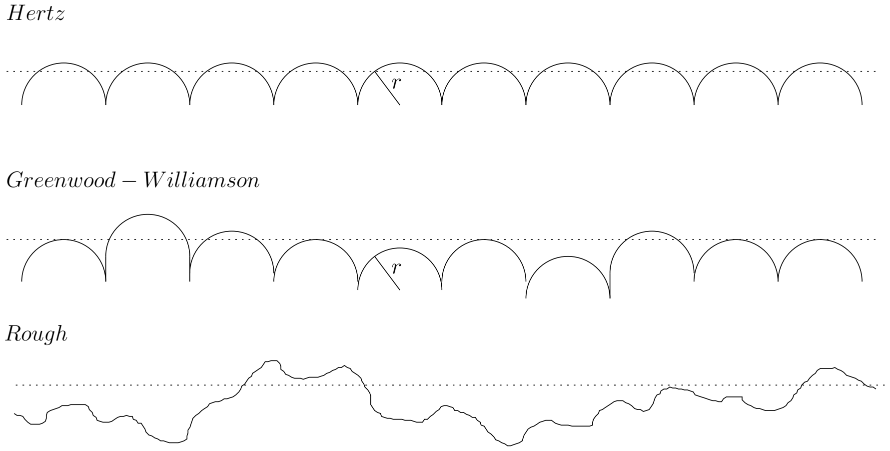

Figure 4.6: *Three different models of a surface.*

The Hertz solution predicts the behavior of a single asperity, and the results can be used to make predictions for a rough surface. Figure (4.6) shows three different realizations of a rough surface. The Hertz result where equal sized asperities at equal heights form a rough surface layer. His theory assumes frictionless indentation. This gives the scaling of the surface area a for a two-dimensional asperity

$$a \sim P^{1/2}, \tag{4.65}$$

where P is the normal load. For a sphere, this relation is

$$a \sim P^{2/3}. \tag{4.66}$$

4.5.1 Greenwood-Williamson theory

The Hertz solution can further be used to find the behavior of a rough surface consisting of contacts with a Gaussian height distribution. This is the Greenwood-Williamson theory [33]. The result is a real surface area that is independent of the apparent area of contact, and a power law behavior of the total normal load and the real surface area with an exponent almost exactly equal to 1

$$a \sim P. \tag{4.67}$$

4.5.2 Roux-Schmittbuhl theory

The normal load and surface area as a function of the compression of the surface layer has been studied by Roux and Schmittbuhl [34, 41]. They assumed that the value of the surface indentation is small, and that the solids in contact are undeformable. They found the scaling relations

$$P \sim \delta^{(H+dim-2)/H}, \tag{4.68}$$

$$a \sim \delta^{(dim-1)/H}, \tag{4.69}$$

and

$$a \sim P^{(dim-1)/(H+dim-2)}. \tag{4.70}$$

dim is the dimension of the system, H is the Hurst exponent, and δ is the surface compression. The root mean square value of the change in height dh over a surface distance x scales as a power law [56], defining the Hurst exponent.

$$dh \sim x^H. \tag{4.71}$$

4.5.3 Persson theory

Persson has developed a different scaling theory [36]. He has a different approach, and calculates the elastic energy. Figure (4.7) shows the system setup. The elastic energy U_{el} stored in the substrate must be equal to the work done by the external pressure.

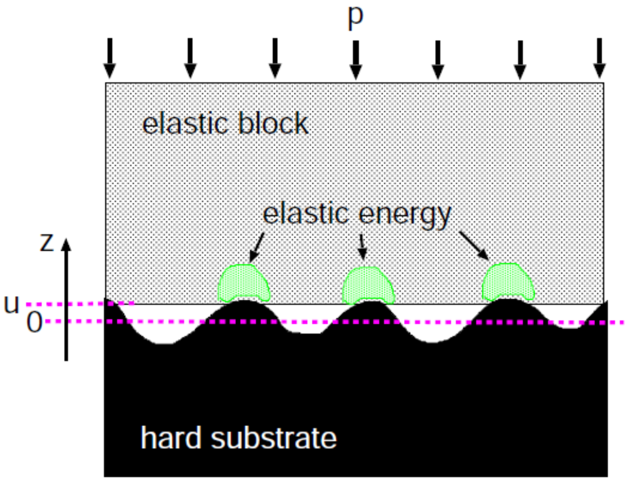

Figure 4.7: *Persson uses the elastic energy to find the relation between the compression of a rough surface and the applied normal load. The figure is taken from [36]*

$$p(u) = -\frac{1}{A}\frac{\partial U_{\mathrm{el}}}{\partial u}, \tag{4.72}$$

where A is the apparent area of contact and u is the surface height, decreasing as the normal load is increased. For small pressures, the elastic energy increases linearly with the load, giving the relation

$$U_{\mathrm{el}}(u) = u_0 A p(u), \tag{4.73}$$

where u_0 depends on the surface roughness. Equation (4.72) can then be expressed as

$$p(u) = -u_0 \frac{\partial p}{\partial u}. \tag{4.74}$$

The resulting pressure variation with u is then

$$p(u) \sim e^{-u/u_0}. \tag{4.75}$$

This theory is valid in three dimensions and with no friction. Persson recently tested his theory using various numerical techniques [37, 57], with good agreement. Robbins [39] also tested the theory using continuum calculations and molecular dynamics. His calculations were in agreement with Persson theory as well. Persson theory further predicts the asperity stress probability distribution [37] for $a \ll A$

$$\Upsilon(\sigma) = \frac{1}{2\sqrt{\pi\Xi}}(e^{-\frac{(\sigma-p)^2}{4\Xi}} - e^{-\frac{(\sigma+p)^2}{4\Xi}}). \tag{4.76}$$

Ξ is a function of the magnification ζ, and p is the squeezing pressure. He also found the compression distribution

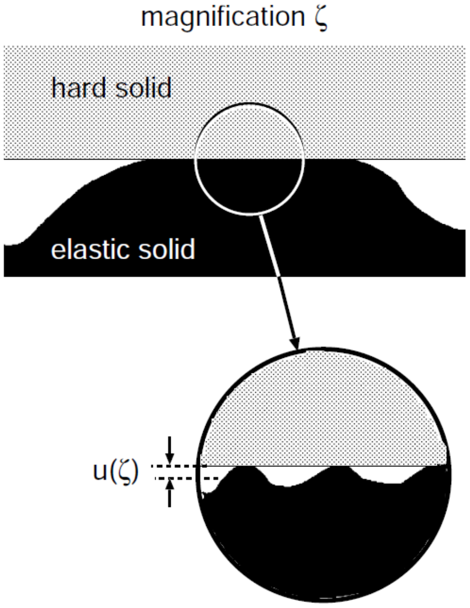

Figure 4.8: *The area of contact depends on the magnification ζ. The figure is taken from [57]*

$$\Upsilon(\delta) \sim (e^{-\frac{(\delta-\xi_1)^2}{\xi_2}} - e^{-\frac{(\delta+\xi_1)^2}{\xi_2}}), \tag{4.77}$$

where ξ_1 and ξ_2 are functions of the roughness and the magnification. Persson theory also predicts a surface area proportional to the normal load.

4.5.4 Boitnott theory

Boitnott theory is an extension of the Greenwood Williamson theory to a shear load under constant normal force [40]. Each asperity is modeled as a sphere using Hertz and Cattaneo-Mindlin theory of contact. The asperities are assumed to be elastically independent. As the shear displacement of between two surfaces in contact is increased slip occurs. Full slip is obtained at different shear displacements depending on the local normal load. The local slips determine the shear strength of the surface. This is illustrated in figure (4.9). Figure (4.10) shows the measured shear strength of Westerly granite sheared with $15MPa$ normal stress [58]. This measurement was carried out by Biegel in 1992. It also shows the asperity height probability distribution, which is consistent with recent theories by Persson [37]. A Boitnott theory in two dimensions is developed and discussed in chapter 7.

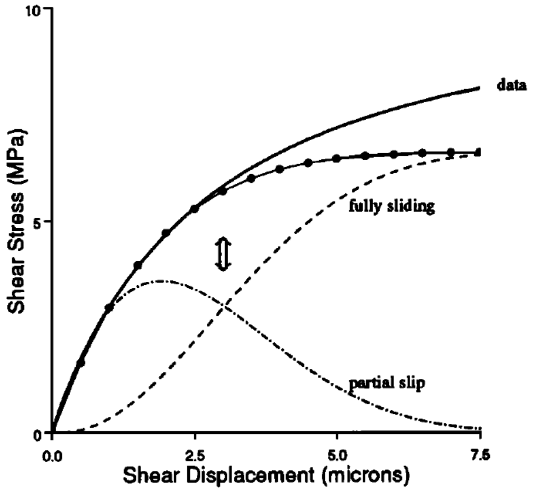

Figure 4.9: *As shear displacement is applied between two rough surfaces in contact, full slip occurs at different length depending on the local normal load. The figure shows experimental data(solid), theory (dotted), and the proportion of contacts sliding (dashed). The figure is taken from [40]*

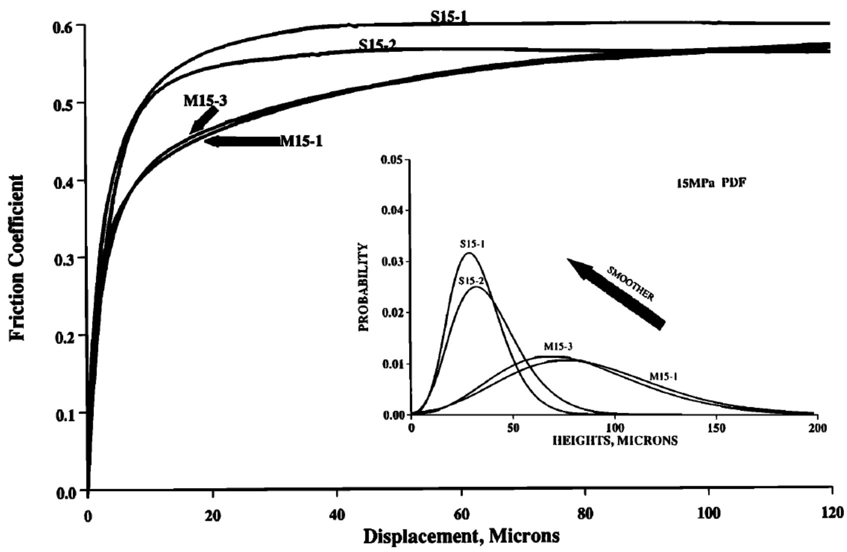

Figure 4.10: *Experimental shear strength of Westerly granite under $15MPa$ normal stress as a function of the shear displacement. Inset: Surface heigth probability distribution. The numbers correspond to different rock samples. Slip will occur for asperities at different shear displacements depending on the normal load. This results in weakening of the shear strength. The figure is taken from [58].*

Chapter 5

A two-dimensional elastic model

From the one-dimensional model we learned that the underlying friction law is important to the system behavior. In order to investigate what this underlying law might be, we introduce a second dimension. Because we wish to look at large system, the equilibrium integration scheme is introduced. It neglects momentum effects, and finds the equilibrium state where the system is at rest. By changing the integration scheme we are no longer able to look at the dynamics of the events, but we are able to model larger systems.

5.1 Elasticity in a two-dimensional material

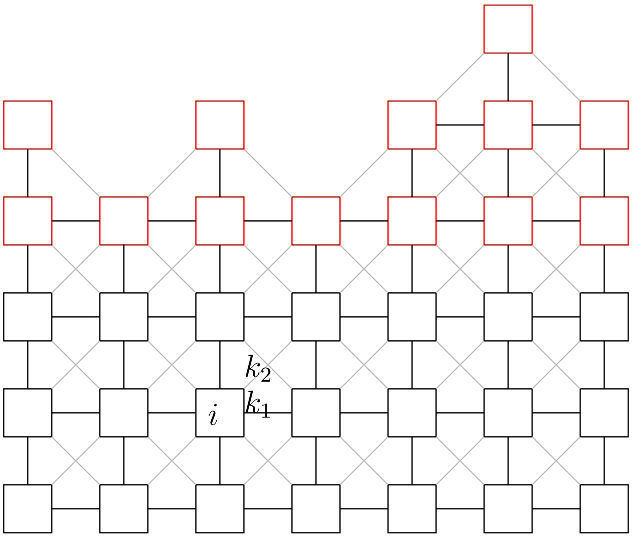

Figure 5.1: *2D model of elastic material with rough surface (red). Spring constant k_1 (black), and k_2 (gray).*

Figure(5.1) shows a two-dimensional square lattice, where a block is connected to its first four neighbors by a spring, k_1, and to its four next nearest neighbors by a spring, k_2. These springs model the elasticity of the material with Young's modulus E. The linear elastic properties can be determined from the local spring constants. There are two possible choices of lattice, the triangular and the square lattice.

5.1.1 Elasticity in a spring block system

We want to determine the spring constants so that the system models a material with Young's modulus E, and Poisson's ratio ν. We follow the work of Monette and Andersson [59] closely, supplying with Kittel's introduction to solid state physics [60].

The triangular lattice

We start with the triangular lattice. The elastic energy density in a bulk node is

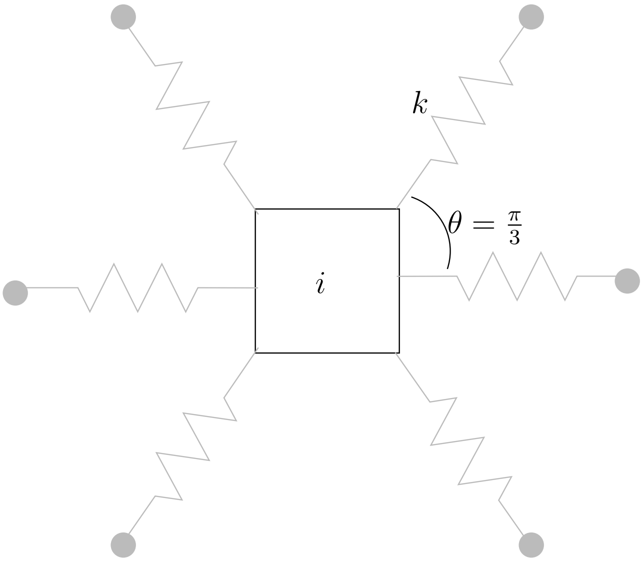

Figure 5.2: *A local node in bulk of a triangular lattice has six neighbor nodes, where the springs are separated by an angle $\theta = \pi/3$. All springs have equal length a_0 and equal spring constants k.*

$$\Phi = \frac{k}{\sqrt{3}a_0^2} \sum_{<ij>} (|r_{ij}| - |r_{ij}^0|)^2, \tag{5.1}$$

where the lattice spacing is a_0, r_{ij} is the distance between nodes i and j that initially were at a distance r_{ij}^0. The area of the hexagonal cell is $\sqrt{3}a_0^2/2$. We can perform a linearization of this expression. This linearization is performed during the discussion of the conjugate gradient method. The result is

$$\Phi = \frac{k}{\sqrt{3}a_0^4} \sum_{<ij>} (u_{ij} \cdot r_{ij}^0)^2, \tag{5.2}$$

where u_{ij} is the displacement, and r_{ij}^0 is the initial distance between nodes i and j. We further wish to write the linearized elastic energy density as a function of the strains ϵ_{ij}.

We rewrite

$$\Phi = \frac{k}{\sqrt{3}} \sum_{<ij>} (\frac{u_{ij}}{a_0} \cdot \frac{r_{ij}^0}{a_0})^2, \tag{5.3}$$

so that

$$\Phi = \frac{k}{\sqrt{3}} \sum_{<ij>} (\epsilon_{ij} \cdot \frac{r_{ij}^0}{a_0})^2. \tag{5.4}$$

This can be written in terms of the strain, and is compared to the elastic energy density of a two-dimensional isotropic elastic continuum [59].

$$\Phi = \frac{k}{\sqrt{3}} (\frac{9}{8}(\epsilon_x^2 + \epsilon_y^2) + \frac{3}{4}\epsilon_x \epsilon_y + \frac{3}{4}(\gamma_x y^2 + \gamma_y x^2)). \tag{5.5}$$

Young's modulus is then found to be

$$E = \frac{2}{\sqrt{3}} k. \tag{5.6}$$

And Poisson's ratio is

$$\nu = \frac{1}{3}, \tag{5.7}$$

The triangular lattice is rotationally invariant. We also note that this result is valid for the bulk only, which means that we have assumed that the number of blocks in the model is large in each direction.

The square lattice

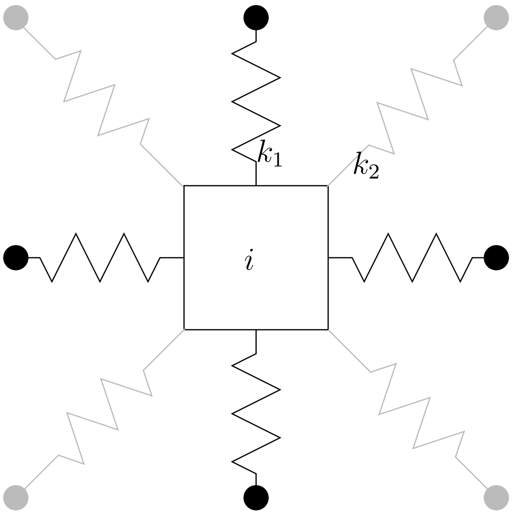

Figure 5.3: *A local node in bulk of a square lattice has eight neighbor nodes, where the springs are separated by an angle $\theta = \pi/4$. There are two different types of springs, where $k_2 = \frac{k_1}{2}$*

The elastic energy density in the square lattice is given by

$$\Phi = \frac{1}{a_0^2} \sum_{j=1}^{4} k_{ij}(|r_{ij}| - |d_{ij}|)^2 + \frac{c}{a_0^2} \sum_{j=1}^{8} (\cos(\theta_{ij}) - \frac{\sqrt{2}}{2})^2 \tag{5.8}$$

where c is the bond-bending spring constant, which in this case is set to zero. This equation can be linearized under the assumption that the local displacements in the lattice are small. We then have that

$$\Phi = \frac{1}{2a_0^2}\sum_{ij=1}^{4} k_{ij}|d_{ij}|^2\Big(\frac{\vec{u}_{ij}\cdot\vec{d}_{ij}}{|d_{ij}|^2}\Big)^2, \tag{5.9}$$

where $\vec{u}$ is the displacement vector, d is the spring equilibrium distance and a_0 is the lattice spacing. The elastic energy can again be written in terms of the strains, and we find Young's modulus to be

$$E = \frac{8}{6}k_1, \tag{5.10}$$

where we have assumed

$$k_2 = \frac{k_1}{2}. \tag{5.11}$$

Poisson's ratio is

$$\nu = \frac{1}{3}, \tag{5.12}$$

which is the same result as for the triangular lattice. Introducing a bending stiffness parameter will let you choose Poisson's ratio ν. The bending stiffness is not included in the following simulations, and the Poisson ratio is always $\nu = 1/3$.

5.2 Integration schemes

The system can be solved using two different integration schemes. The time integration, which gives us the possibility to study single events, and the equilibrium integration scheme that is much faster, and can simulate large systems over a longer time interval. We introduce two equilibrium integrators. The conjugate gradient method, and the successive over-relaxation method.

5.2.1 Equations of motion

For a block the following equations determine the motion:

$$m_i\ddot{x}_i = \sum_{j=1}^{n} k_{ij}(r_{ij} - d_{ij})\frac{x_j - x_i}{r_{ij}} \tag{5.13}$$

$$m_i\ddot{y}_i = \sum_{j=1}^{n} k_{ij}(r_{ij} - d_{ij})\frac{y_j - y_i}{r_{ij}} \tag{5.14}$$

where n is the number of neighbors r is the distance between them, and d is the equilibrium distance, a_0 or $\sqrt{2}a_0$.

$$r_{ij} = \sqrt{(x_j - x_i)^2 + (y_j - y_i)^2} \tag{5.15}$$

We want to use the model to simulate large systems and use the equilibrium integration scheme where the equations of motion are not solved, but equilibrium states where the energy is minimized.

5.2.2 Conjugate gradient method

In general we wish to find the minimum of a function $U(\vec{x})$, and approximate with a Taylor expansion around $\tilde{\vec{x}}$

$$U(\vec{x}) \approx U(\vec{\tilde{x}}) + \sum_i \frac{\partial U}{\partial x_i} x_i + \frac{1}{2} \sum_{i,j} \frac{\partial^2 U}{\partial x_i \partial x_j} x_i x_j. \tag{5.16}$$

This can be rewritten as

$$U(\vec{x}) \approx c - \vec{b} \cdot \vec{x} + \frac{1}{2} \vec{x} \cdot \underline{A} \cdot \vec{x}, \tag{5.17}$$

where

$$c = U(\vec{\tilde{x}}), \tag{5.18}$$

$$\vec{b} = -\nabla U|_{\vec{\tilde{x}}}, \tag{5.19}$$

and $\underline{A}$ is the Hessian matrix at the point $\vec{\tilde{x}}$

$$[\underline{A}]_{ij} = \frac{\partial^2 U}{\partial x_i \partial x_j} |_{\vec{\tilde{x}}}, \tag{5.20}$$

The gradient of f is given by

$$\nabla U = \underline{A} \cdot \vec{x} - \vec{b}. \tag{5.21}$$

U is minimized when $\nabla U = 0$, so that the problem reduces to solving the linear system

$$\underline{A} \vec{x} = \vec{b}. \tag{5.22}$$

From the positions of the nodes the forces are known. In other words we know $\vec{x}$ and $\nabla^2 \vec{x}$. This linear system can be solved even if $\underline{A}$ is not known. This system of linear equations can be solved using the following equations with an initial guess of the equilibrium states $\vec{g}_0$ and a start vector and $\vec{h}_0 = g_0$.

$$\vec{g}_{i+1} = \vec{g}_i - \lambda_i \underline{A} \cdot \vec{h}_i \tag{5.23}$$

If we know the gradient of U at a point $\tilde{\vec{x}}$, we have that

$$\vec{g}_{i+1} = -\nabla U(\vec{\tilde{x}}_{i+1}). \tag{5.24}$$

$$\vec{h}_{i+1} = g_{i+1} + \gamma_i \vec{h}_i \tag{5.25}$$

where the coefficients λ and γ are given by

$$\lambda_i = \frac{\vec{g}_i \cdot \vec{g}_i}{\vec{h}_i \underline{A} \vec{h}_i} = \frac{\vec{g}_i \cdot \vec{h}_i}{\vec{h}_i \underline{A} \vec{h}_i} \tag{5.26}$$

$$\gamma_i = \frac{\vec{g}_{i+1} \cdot \vec{g}_{i+1}}{\vec{g}_i \cdot \vec{g}_i}. \tag{5.27}$$

The function $U(\vec{x})$ we wish to minimize is the elastic energy in the system. The potential energy in a spring is given by

$$U_{ij} = \frac{1}{2} k \Delta x_{ij}^2 \tag{5.28}$$

The function we wish to minimize is the elastic energy in the system, including the energy introduced by the potential surfaces. The total energy U is given by

$$U(\tilde{x}) = \sum_{i=1}^{N}\sum_{j=1}^{n}\frac{1}{2}k_{i,j}(\sqrt{(x_i - x_j)^2 + (y_i - y_j)^2} - d_{i,j})^2 \tag{5.29}$$

where N is the total number of nodes, and n is the number of neighbor nodes. The potential surfaces are included as neighbors in the sum over j. To use the linear biconjugate gradient method from Numerical Recipes [49], we need to be able to calculate the positions using ∇U. We define

$$U(\tilde{x}) = \sum_{i=1}^{N}\sum_{j=1}^{n}\frac{1}{2}k_{i,j}(\sqrt{|\vec{r}_i - \vec{r}_j|} - d_{i,j})^2, \tag{5.30}$$

and rewrite the square root as a small change in position of the nodes $\Delta\vec{r}_i$ from the initial position $\vec{r}_{i,0}$.

$$\vec{r}_i - \vec{r}_j = (\vec{r}_{i,0} + \Delta\vec{r}_i) - (\vec{r}_{j,0} + \Delta\vec{r}_j). \tag{5.31}$$

This leads to

$$U(\tilde{x}) = \sum_{i=1}^{N}\sum_{j=1}^{n}\frac{1}{2}k_{i,j}(\sqrt{((\vec{r}_{i,0} - \vec{r}_{j,0}) + (\Delta\vec{r}_i - \Delta\vec{r}_j))^2} - d_{i,j})^2. \tag{5.32}$$

This expression can be linearized.

$$U(\tilde{x}) = \sum_{i=1}^{N}\sum_{j=1}^{n}\frac{1}{2}k_{i,j}(\sqrt{(\vec{r}_{i,0} - \vec{r}_{j,0})^2 + 2(\vec{r}_{i,0} - \vec{r}_{j,0})\cdot(\Delta\vec{r}_i - \Delta\vec{r}_j) + (\Delta\vec{r}_i - \Delta\vec{r}_j)^2} - d_{i,j})^2. \tag{5.33}$$

We rewrite this as

$$U(\tilde{x}) = \sum_{i=1}^{N}\sum_{j=1}^{n}\frac{1}{2}k_{i,j}(|\vec{r}_{i,0} - \vec{r}_{j,0}|\sqrt{1 + 2\frac{(\vec{r}_{i,0} - \vec{r}_{j,0})\cdot(\Delta\vec{r}_i - \Delta\vec{r}_j)}{|\vec{r}_{i,0} - \vec{r}_{j,0}|^2} + \frac{(\Delta\vec{r}_i - \Delta\vec{r}_j)^2}{|\vec{r}_{i,0} - \vec{r}_{j,0}|^2}} - d_{i,j})^2. \tag{5.34}$$

Since the system initially is at equilibrium, we have that

$$d_{i,j} = |\vec{r}_{i,0} - \vec{r}_{j,0}|. \tag{5.35}$$

Inserting this we find

$$U(\tilde{x}) = \sum_{i=1}^{N}\sum_{j=1}^{n}\frac{1}{2}k_{i,j}(d_{i,j}\sqrt{1 + 2\frac{(\vec{r}_{i,0} - \vec{r}_{j,0})\cdot(\Delta\vec{r}_i - \Delta\vec{r}_j)}{d_{i,j}^2}\frac{(\Delta\vec{r}_i - \Delta\vec{r}_j)^2}{d_{i,j^2}}} - d_{i,j})^2. \tag{5.36}$$

We further assume that the displacements $\Delta\vec{r}_i$ are small so that

$$\frac{(\Delta\vec{r}_i - \Delta\vec{r}_j)^2}{d_{i,j^2}} << 1, \tag{5.37}$$

and can be neglected. Approximating

$$\sqrt{1+x} \simeq 1 + \frac{1}{2}x, \tag{5.38}$$

we find

$$U(\tilde{x}) \simeq \sum_{i=1}^{N}\sum_{j=1}^{n} \frac{k_{i,j}}{2d_{i,j}^2}\big((\Delta\vec{r}_i - \Delta\vec{r}_j)\cdot(\vec{r}_{i,0} - \vec{r_{j,0}})\big)^2. \tag{5.39}$$

We can now calculate

$$\frac{\partial U(\tilde{x})}{\partial \Delta x_i} = \sum_{j=1}^{n} \frac{k_{i,j}}{d_{i,j}^2}\big((\Delta\vec{r}_i - \Delta\vec{r}_j)\cdot(\vec{r}_{i,0} - \vec{r_{j,0}})\big)\cdot(\vec{r}_{i,0} - \vec{r}_{j,0})\cdot\vec{e}_x, \tag{5.40}$$

where $\vec{e}_x$ is the unit vector. If we assume that $\frac{\partial U(\tilde{x})}{\partial \Delta x_i}$ only results in a displacement in the x-direction, we can rewrite this as

$$\frac{\partial U(\tilde{x})}{\partial \Delta x_i} = \sum_{j=1}^{n} \frac{k_{i,j}}{d_{i,j}^2}(x_{i,0} - x_{j,0})^2\Delta x, \tag{5.41}$$

and

$$\frac{\partial U(\tilde{x})}{\partial \Delta y_i} = \sum_{j=1}^{n} \frac{k_{i,j}}{d_{i,j}^2}(y_{i,0} - y_{j,0})^2\Delta y. \tag{5.42}$$

Using equations (5.41) and (5.41) allows us to use the conjugate gradient method to minimize the energy in the system. The conjugate gradient method was implemented using a linear bi-conjugate gradient method [49].

5.2.3 Successive over-relaxation (SOR)

When applying shear forces to the block spring system, we wish to implement a friction law. If we are to do this, we need to make sure that the relaxation algorithm is forward in time (Convergence towards the equilibrium state follows a physical path). Linearizing the conjugate gradient scheme, we found that we can move a node to its equilibrium position if we know the derivative of the energy, the force. We start by calculating the force on a node i

$$f_i = \sum_{j=1}^{n} k_{i,j}(\Delta r - d_{i,j}) = \sum_{j=1}^{n} k_{i,j}\left(\sqrt{(x_i - x_j)^2 + (y_i - y_j)^2} - d_{i,j}\right) + F_{ext,i}. \tag{5.43}$$

We then estimate the equilibrium position to be

$$\Delta x_i = \frac{f_{x,i}}{\sum_{j=1}^{n} k(x_{i,0} - x_{j,0})^2 d_{i,j}^2} d_{i,j}^2 \tag{5.44}$$

and

$$\Delta y_i = \frac{f_{y,i}}{\sum_{j=1}^{n} k(y_{i,0} - y_{j,0})^2} d_{i,j}^2 \tag{5.45}$$

using successive over-relaxation we over-relax the system by a factor $\varrho > 1$ [61].

$$\Delta x_i = \varrho\frac{f_{x,i}}{\sum_{j=1}^{n} k(x_{i,0} - x_{j,0})^2} d_{i,j}^2 \tag{5.46}$$

and

$$\Delta y_i = \varrho\frac{f_{y,i}}{\sum_{j=1}^{n} k(y_{i,0} - y_{j,0})^2} d_{i,j}^2 \tag{5.47}$$

where ϱ is a constant that can be chosen. Implementing the algorithm, ϱ is allowed to wary to ensure fast convergence and to ensure that the system will reach equilibrium. When a node is in contact with a potential surface, ϱ is reduced to achieve an algorithm that is forward in time.

5.3 Details of the numerical model

5.3.1 External forces

External forces are applied through potential surfaces. The force from a potential surface on a node is

$$F_i(y) = k_{\text{pot}}\Delta y, \tag{5.48}$$

where Δy is the overlap between node i and the potential surface, and k_{pot} is the strength of the potential surface.

5.3.2 Interactions between nodes initially not in contact

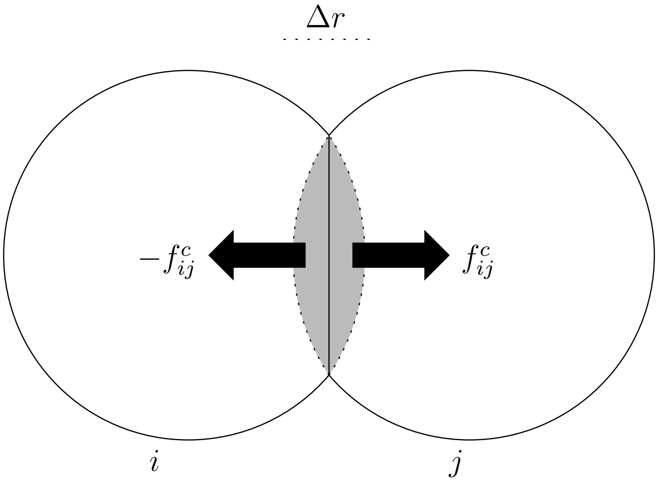

Figure 5.4: *Modeling the elastic force from blocks that are not initially neighbor blocks.*

The nodes are modeled as circles with radius $r = \frac{a_0}{2}$. When contact between nodes that intially are not in contact occur, a repelling force

$$f_{ij}^c = k\Delta r \tag{5.49}$$

where k equals the lattice spring constant and Δr is the overlap of the nodes. Figure (5.4) shows how this force is modeled.

5.3.3 Choice of integration scheme

The SOR-algorithm is not as fast as the conjugate gradient method, but it can be applied on systems that are subject to friction forces. The systems that will be investigated are systems where a friction force applies. For this reason, we use the successive over relaxation in the rest of the thesis. A termination criterion

$$\varepsilon = \frac{F_{max}}{ka_0} \tag{5.50}$$

is introduced. This means that the maximum displacement in the next iteration step would be εa_0. $\varepsilon = 10^{-4}$ is used in all simulations in this thesis.

5.3.4 Choice of lattice

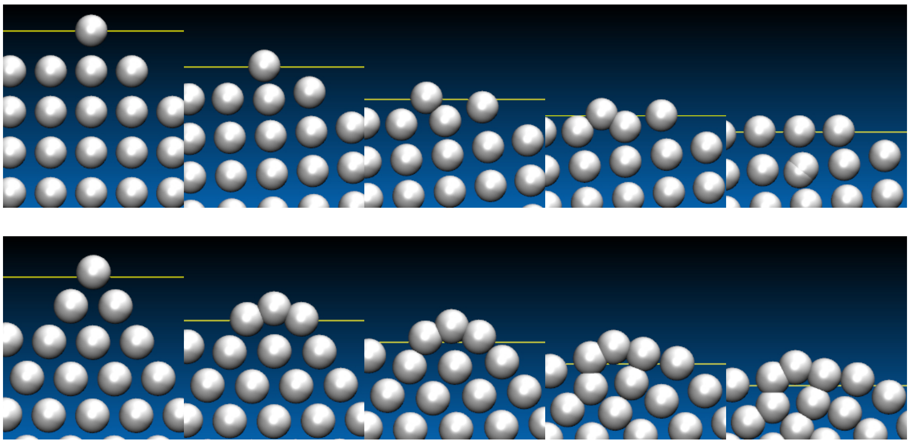

Figure 5.5: *A test of the implementation using a square lattice (top) and a triangular lattice (bottom). The external force acting on the system is introduced through a potential surface (yellow line).*

The integration scheme is tested using both the square and the triangular lattice. A rough surface is generated using strict lattice positions. The bottom layer is stuck and a potential surface acts on the top layer. Figure (5.5) shows how the two systems evolve as the potential surface is moved. In the square lattice calculation nodes at the contact interface may find an equilibrium state that is unphysical. When the potential surface is removed, the system initialized with a triangular lattice will return to its initial state. This is not necesseraly the case for a square lattice.

In addition, a different method of initialization can be used assuming a triangular lattice. In the rest of the thesis, a triangular lattice is used.

5.3.5 Scaling

The variables we will measure are the contact area, the force, and the pressure distributions. Since $E = 2/\sqrt{3}k$, we have that the force on a node is given by

$$f_i = \frac{\sqrt{3}}{2} E \sum_j \Delta r_{ij} - d_{ij}. \tag{5.51}$$

And the pressure is

$$p_i = \frac{\sqrt{3}E}{4\pi a_0} \sum_j |\Delta r_{ij} - d_{ij}|. \tag{5.52}$$

In a system of length L we find the dimensionless displacement u/L, the dimensionless load $P/(LE)$, and the dimensionless area a/L. If we measure the surface area as a fraction of the system size, we find that the Young's modulus of the system, and the system resolution a_0 is not important. The system will not experience different behavior based on E. It only gives a different scale to the forces and the pressure.

5.4 Initialization

The discretization effects when using a strictly triangular lattice can be very large. To avoid some of these problems we introduce a method of initialization using the random sequential absorption method [62]. We name the method the random drop method.

5.4.1 The random drop method

The random drop method, is an initialization method that will prevent some of the difficulties due to discretization effects. With a strict lattice initialization the nodes can only be placed at specific lattice points (as in figure (5.5)). This will be a problem when initializing complicated structures. The solution is to use the random drop method and a triangular lattice. The lattice spacing is set to $a_0 = \frac{L}{N_x - 1}$, and the nodes are given a radius $r = a_0/2$. Nodes are placed along the boundary with a distance equal to the chosen lattice spacing, with no other constraints. These nodes are not allowed to move during the iteration process. The rest of the nodes are assigned a radius

$$r_s < r. \tag{5.53}$$

These nodes are dropped at random positions in the bulk until the maximum density of the triangular lattice is reached. They are not allowed to overlap. The radius r_s is then increased to

$$r_s = r, \tag{5.54}$$

and an SOR integration algorithm with $\varepsilon = 10^{-2}$ is started. When the SOR integration is done, the system consists of large areas of nodes in a triangular lattice, and some boundary zones in between. This is set to be the systems equilibrium state. Springs are then placed in the system. The spring constant k is the same for all springs, but the equilibrium distance d_{ij} is allowed to change. If we use the fact that the triangular lattice is invariant under rotation [59], we have initialized a material with the elasticity uniquely defined by the spring constant k, and have minimized discretization effects.

5.4.2 Maximum density of the triangular lattice

The area of the triangle is

$$A_t = \frac{a_0 h}{2}, \tag{5.55}$$

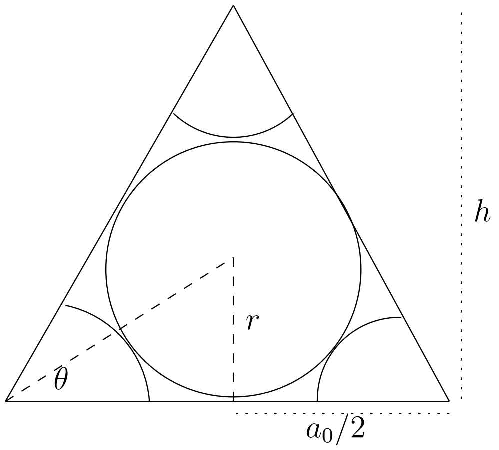

Figure 5.6: *The minimum porosity of the triangular lattice with circular nodes.*

where

$$h = \frac{L\tan(\pi/3)}{2} = \frac{a_0\sqrt{3}}{2}. \tag{5.56}$$

The area of the circle is

$$A_c = \pi r^2, \tag{5.57}$$

where

$$r = \frac{a_0\tan(\pi/6)}{2} = \frac{a_0\sqrt{3}}{6}. \tag{5.58}$$

We then have that

$$h - 2r = 3, \tag{5.59}$$

so that the circles in the corners of the triangle give us the area of half a circle. The maximum density of a triangular lattice filled with circles is then given by

$$\rho_m = \frac{3/2\pi r^2}{3a_0/2r} = \frac{\pi\sqrt{3}}{6}. \tag{5.60}$$

The maximum density determines how many blocks are dropped into the geometry that is initialized.

5.5 Calculating the contact area

One aim of the calculations with the potential surface is to be able to calculate the contact area as a function of applied force. To be able to do that we need an algorithm that calculates the surface area of the contact between the material and the potential surface. Again we model the blocks as circles with radius $\frac{a_0}{2}$. When a node is in contact with a potential surface, an area of a_0 is added to the total area. The overlap of area contributions from nodes is removed in order to get an accurate value of the total area A.

Note that the contact area in two dimensions is actually a contact length. The term contact area will still be used in the following chapters.

5.6 Introducing friction in the 2D equilibrium model

When there is contact between two bodies, friction applies along the contact interface. These forces have to be implemented in the model. A problem arises because there is no momentum in the quasi-static model, and in order to introduce a local friction law in the equilibrium integration scheme, assumptions have to be made.

First we need to verify that the calculations are forward in time. This can only be done using the SOR algorithm. We introduce a second accuracy parameter $\varepsilon_{\mathrm{surf}} = 10^{-4}$. If a local node is in contact with a potential surface, it is only allowed to move $\varepsilon_{\mathrm{surf}} a_0$ during a single iteration. This will prevent large oscillations of the tangential force which can make the blocks reach static friction earlier than expected. The iterations proceed until an accuracy ε in the bulk and $\varepsilon_{\mathrm{surf}}$ along the surface is reached.

The local friction law can now be defined. We calculate the normal load at the contact interface and define the dynamic friction coefficient μ_k. During steady sliding, the friction force equals the dynamic friction force. This is implemented in the equilibrium integration scheme by stopping the blocks when the local tangential force is within ϵ_{surf} of the dynamic friction force

$$f_{k,i} = \mu_k p_i. \tag{5.61}$$

In addition, a static friction coefficient μ_s is defined. The static friction force is

$$f_{s,i} = \mu_s p_i \tag{5.62}$$

where p_i is the local normal force from the potential surface. The static friction treshold has to be exceeded in order for a local node to move.

Using this Amontons-Coulomb friction law dry friction is assumed. Other friction laws could have been used as well. An example is the spring to track friction model similar to the one used by Braun [31].

Chapter 6

Cylinder on plane contact and the semi-circle

In chapter 4, the Hertz solution for frictionless indentation of a cylinder was obtained using the following boundary conditions.

- The surfaces are continuous and non-conforming: $a \ll 2R$
- The strains are small
- The solids can be considered as elastic half-spaces
- The surfaces are frictionless

In this chapter, the Hertz theory will be used to used to validate the two-dimensional quasi-static model by comparison with known results for small deformations.

Further, a single asperity is modeled in two dimensions as a semi-circle glued to a rigid body. The asperity is subjected to a tangential load Q and results are compared to those of Cattaneo and Mindlin. A scaling theory for the shear stiffness of the asperity involving the friction coefficient μ_k, the surface compression, δ, and the tangential displacement u_x is found. To avoid references to equations in a different chapter, the relevant equations are restated here. The parameters used are listed in table (6.1). If simulations use different parameters it will be specifically stated in the figure text. Note that the same friction coefficients are not used during the normal and tangential loading.

6.1 Frictionless contact

The analytical solution of this problem is well known from the Hertz theory of elasticity. The surface area between two cylinders in elastic contact in two dimensions is given by [4]

$$a = 2\left(\frac{3PR}{4E^*}\right)^{1/2}, \tag{6.1}$$

where

$$R \equiv \left(\frac{1}{R_1} + \frac{1}{R_2}\right)^{-1} \tag{6.2}$$

Parameter	Description	Indentation	Shear
N_x	Resolution in x-direction	150	150
k_{pot}	Potential surface strength	10^3k	10^3k
du_y	Displacement step	a_0	0
du_x	Displacement step	0	$0.1a_0$
δ	Compression	0.1	0.1
μ_s	static friction coefficient	0	0.5
μ_k	kinetic friction coefficient	0	0.5
ε	Accuracy	10^{-4}	10^{-4}
$\varepsilon_{\text{surf}}$	Surface accuracy	10^{-4}	10^{-4}
	Bottom boundary	Glued to rigid body	Glued to rigid body
	Top boundary	Potential surface	Potential surface
	Number of runs	50	50

Table 6.1: *The list of parameters used in indentation and shear of a cylinder. If simulations use different parameters it will be specifically stated. Note that the boundary conditions during normal loading are different from the boundary conditions during tangential loading.*

and

$$E^* \equiv \left(\frac{1-\nu_1^2}{E_1} + \frac{1-\nu_2^2}{E_2} \right)^{-1}. \tag{6.3}$$

If we let one of the surfaces be a flat rigid body, we find that

$$R = R_1, \tag{6.4}$$

and

$$E^* = \frac{E_1}{1-\nu_1^2}. \tag{6.5}$$

The system size is $L = 2R$.

6.1.1 Contact area and discretization effects

We want to obtain the contact area as a function of the applied normal load for a circle. The normal load is applied through a displacement of two potential surfaces. The resulting contact area is plotted in figure (6.1.1) for $N_x = 50$ and $\mu_s = \mu_k = 0$, and the discretization effects are quite large. There are three solutions to such discretization problems:

- Increase the resolution
- Increase the number of samples and average (ensamble average)
- Intriduce a variyng node size and increase the number of nodes along the inderface

The first two solutions are implemented and presented later in this chapter, while the latter is not carried out in this thesis. Increasing the number of nodes will decrease the pressure experienced by the individual nodes along the contact surface. At the same time, averaging over many samples will make sure that the discretization effects become negligible, as is demonstrated in figure (6.2). Good agreement between numerical results and theory for the surface area is found using a system consisting of 2000 nodes.

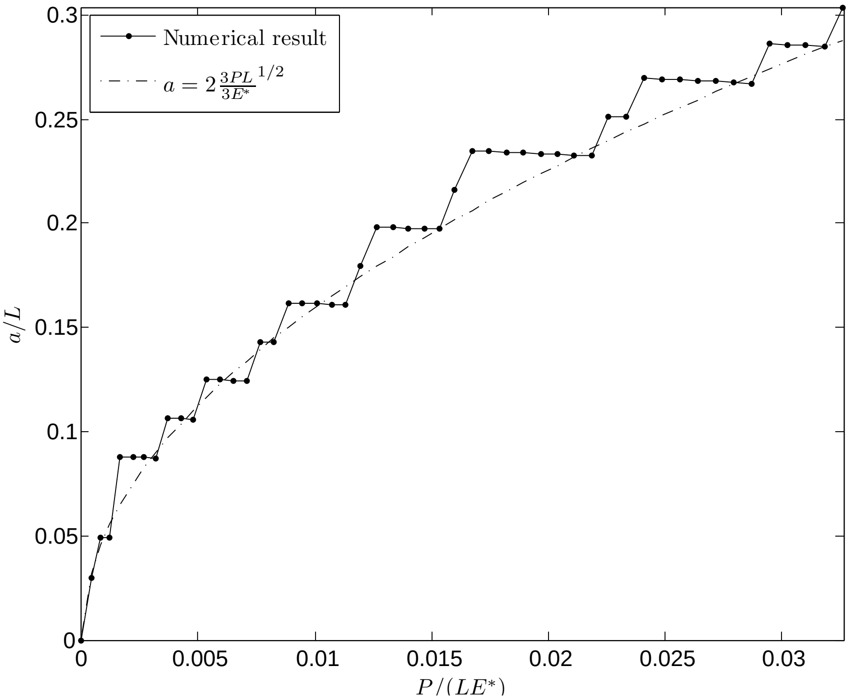

Figure 6.1: *The contact area as a function of the applied normal load P applied through a rigid surface. Only one simulation is used, and the discretization effects are quite large. Parameters from table (6.1) with $N_x = 50$.*

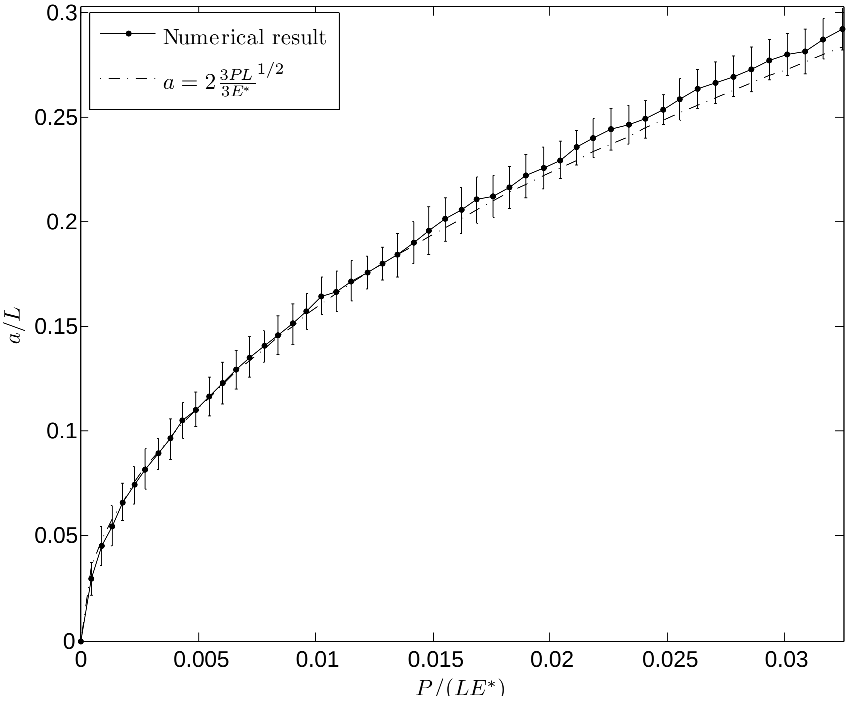

Figure 6.2: *The contact area as a function of the applied normal load P applied through a rigid surface. The results are found by using 50 simulations with circles consisting of approximately 2000 nodes ($N_x = 50$). The bars show the standard deviation of the surface area calculations.*

6.1.2 Modeling a single asperity

Simulations of a cylinder on a plane contact are used to gain insight in how a single asperity behaves. A rough surface consists of multiple contact points (asperities). A single asperity is modeled as a semi-circle. The boundary conditions are changed so that, the bottom layer is glued to a rigid body, while $\mu_s = \mu_k = 0$ at the contact interface. The resolution is increased to $N_x = 150$. Results are averaged over 50 simulations to avoid discretization effects. The resulting surface area is plotted in figure 6.3. The result is close to the analytical prediction made by Hertz even for a large normal load P.

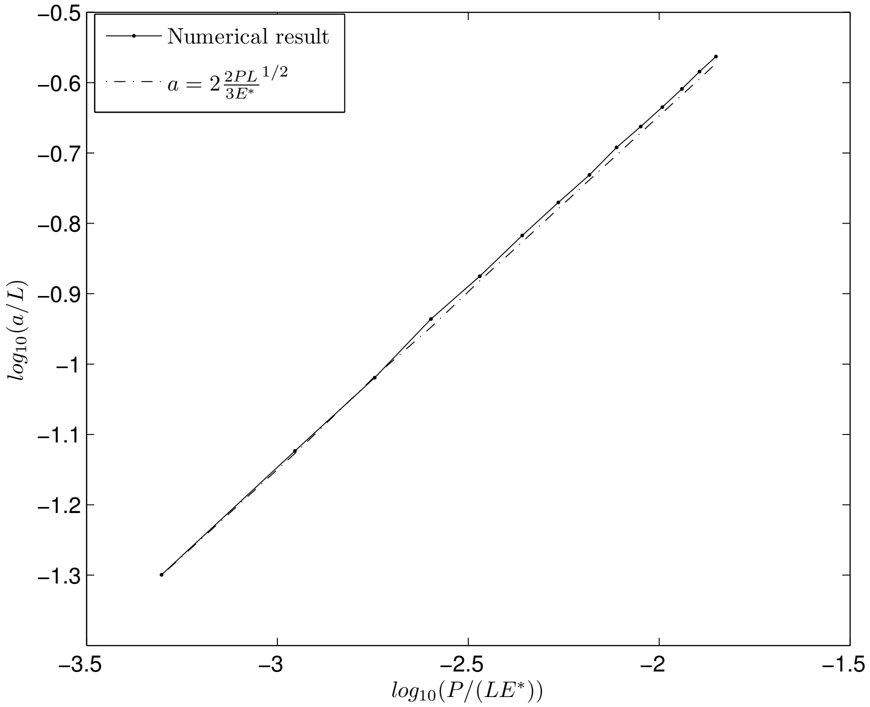

Figure 6.3: *The contact area of a semi-circle as a function of the applied normal load P. The bottom layer is glued to a rigid body, whereas the top layer is interacting with a potential surface.*

6.1.3 Distribution of pressure

Predictions also exist for the normal pressure distribution in a circle. We define the compression

$$\delta = \frac{h_0 - h}{h_0}, \tag{6.6}$$

where h_0 is the initial height of the system, and h is the height after a normal load is applied. Figure(6.4) shows the pressure distribution at the interface between the semi-circle and the potential surface with $\delta = 0.1$. There are some deviations to the analytical prediction that arise due to the way the system is initialized. When using the random drop initialization algorithm, defects in the material in form of missing nodes may appear. This changes the pressure distribution locally. The effect decreases with

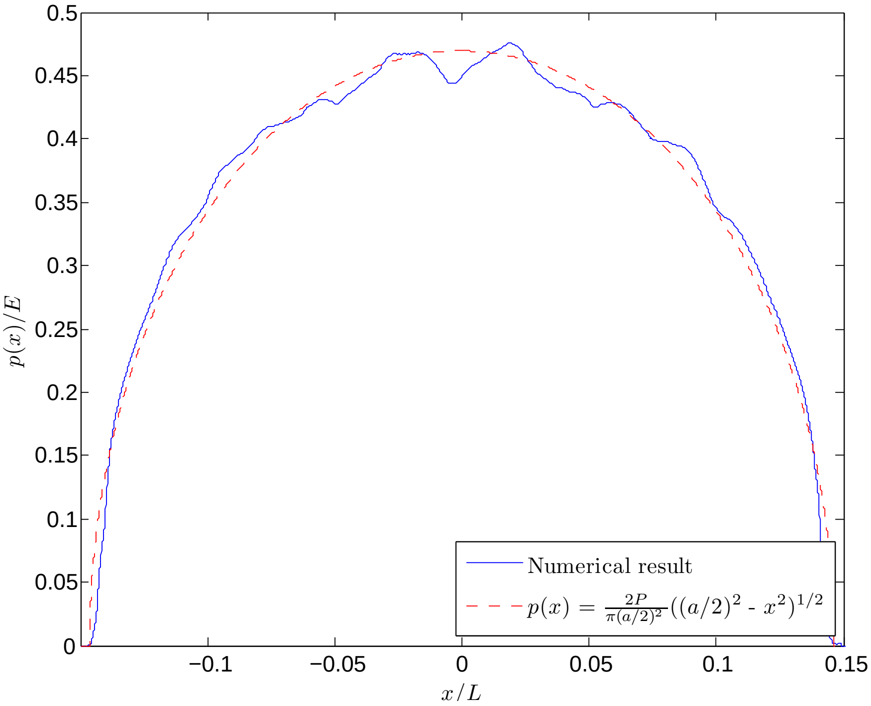

Figure 6.4: *The pressure distribution $p(x)$ at the contact interface between the semi-circle and the potential surface. The dotted line is the analytical prediction. Parameters are taken from table (6.1).*

an increase in the number of simulations used to calculate the average distribution. The pressure distribution in the bulk is also calculated in figure(6.6).

A different measure of interest is the total normal load P as a function of the compression. This is plotted in figure(6.5). The relation between the compression and the total normal load is a power law. A linear fit gives the scaling relation

$$P \sim \delta^{\beta}, \tag{6.7}$$

with $\beta = 1.3$. Since $a \sim P^{1/2}$, we also get the scaling relation

$$a \sim \delta^{\beta/2}. \tag{6.8}$$

A simple geometrical argument would give

$$a \sim \delta^{1/2}, \tag{6.9}$$

resulting in $\beta = 1$. However, due to elastic deformation of the contact and the Poisson ratio, the surface area will be slightly larger, and the exponent larger than $1/2$. The result is $\beta > 1$.

6.2 The Cattaneo-Mindlin approach

Having verified that the code works for frictionless normal indentation, we move on to the case where we apply a tangential load Q imposed by a displacement u_x of the potential

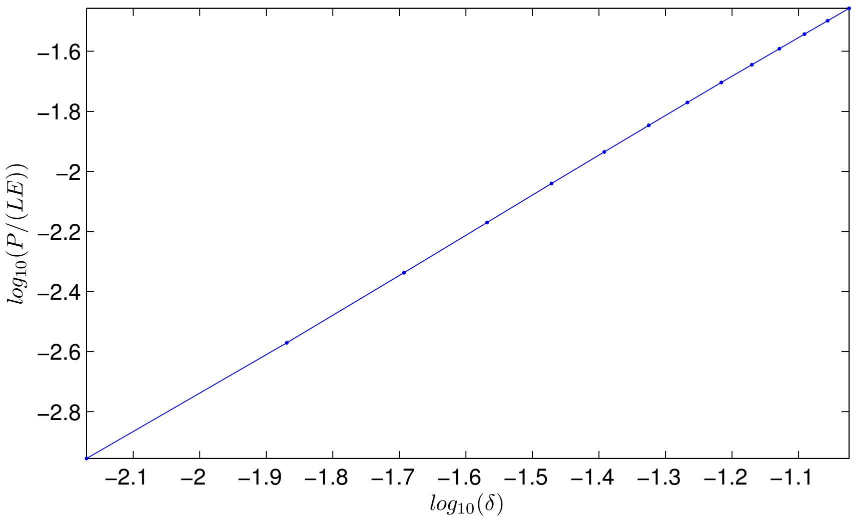

Figure 6.5: *The total normal load P as a function of the compression δ averaged over 50 simulations.*

surface in the negative x-direction. The normal load is applied with $\mu_s = \mu_k = 0$ (assumption in the Cattaneo-Mindlin theory), while friction is introduced during the tangential loading. The resulting pressure distribution when $\mu_s = \mu_k \to \infty$ is shown in figure (6.6). The semi-circle is compressed by $\delta = 0.1$, and the displacement u_x/L is 0.01. The trailing edge of the semi-circle is at its left side. The applied tangential load

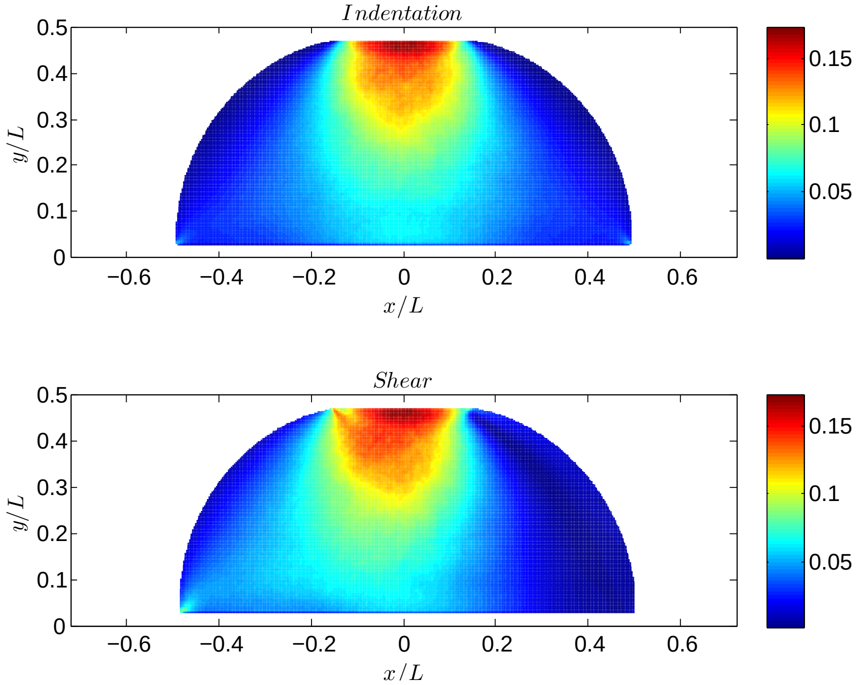

Figure 6.6: *The pressure distribution $p(x)/E$ in the semi-circle during frictionless indentation ($\mu_s = \mu_k = 0$) (top) and shear during full stick ($\mu_s = \mu_k \to \infty$) (bottom). $\delta = 0.1$ and $u_x/L = 0.01$.*

Q results in a high pressure zone below the trailing edge, and a low pressure zone below the leading edge.

In chapter 4, we saw that the normal and shear pressure distributions at the contact interface is predicted by Cattaneo-Mindlin theory. Initially the contact interface is stuck. As a tangential load Q is applied, slip occurs at the edges of contact, and the size of the stick region c decreases. $c(Q)$ is also predicted in the theory. We investigate if agreement with these predictions is obtained in our model.

6.2.1 Full stick

We start with the full stick case. The nodes at the contact interface are stuck, and a tangential displacement u_x is applied. The resulting traction distribution $q(x)$ is predicted by Cattaneo-Mindlin theory [4] to be

$$q(x) = \frac{Q}{\pi\sqrt{(a/2)^2 - x^2}}, \tag{6.10}$$

where Q is the total tangential load

$$Q = \int q(x)dx, \tag{6.11}$$

and a is the contact area. The semi-circle is further subjected to a shear displacement u_x, and the resulting normal pressure and traction distributions are measured. When measuring $q(x)$ we encounter some problems at the edges of contact when the results are averaged over multiple simulations. The pressure distributions are obtained by a sum over linear interpolations for each sample, and due to discretization effects the pressure is not well defined at the edges for all samples. This makes it difficult to compare the numerical results with the analytical predictions. The solution is to estimate Q using only the interval (b_1, b_2) where the pressure distribution is well defined in all samples. We find

$$\int_{b_1}^{b_2} \frac{Q}{\pi\sqrt{a^2 - x^2}} = \frac{Q}{\pi}(\arcsin(\frac{b_2}{a}) - \arcsin(\frac{b_1}{a})), \tag{6.12}$$

and if we let B be the total shear force in the interval $[b_1, b_2]$, we find that

$$Q = \frac{\pi B}{\arcsin(\frac{b_2}{a}) - \arcsin(\frac{b_1}{a})}. \tag{6.13}$$

The analytical solution diverges at the edges of contact, see figure (6.7) (bottom). We find that $q(x)$ does not increase in the same way as the analytical solution the edges of contact. This is expected because an infinite pressure at the edges is unphysical. The results are found for $\delta = 0.1$. The compression is chosen so that the number of nodes along the contact interface is sufficiently large to measure the pressure distributions. Figure (6.7) shows a plot of $q(x)$ in the full stick case for $\delta = 0.1$ $u_x/L = 0.01$. The results are quite close to the analytical expression, but with a small asymmetry not predicted by Cattaneo-Mindlin theory.

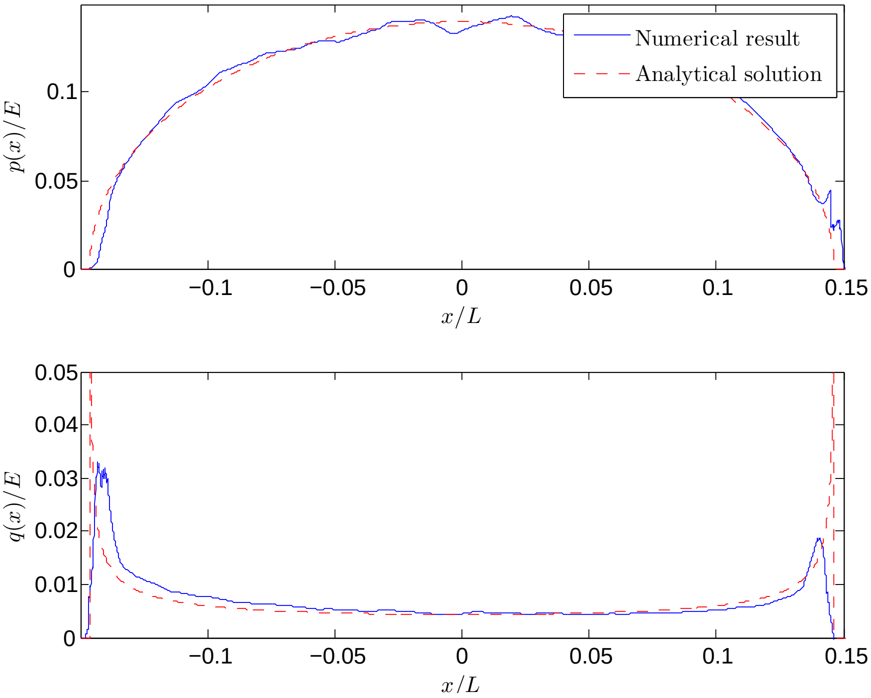

Figure 6.7: *The normal pressure (top) and traction distribution (bottom) at the contact interface of the semi-circle and the plane assuming full stick conditions. The compression is $\delta = 0.1$, while the tangential displacement is $u_x/L = 0.01$. Dashed lines are analytical predictions by Cattaneo-Mindlin and Hertz theory. The shear force is applied in the negative x-direction, so that the trailing edge of the semi-circle is at the left side of the figure.*

6.2.2 One friction coefficient $\mu_k = \mu_s$

Analytical predictions are also found if $\mu_s = \mu_k = 0.5$. Cattaneo-Mindlin theory gives [4]

$$q(x) = \mu_k \frac{2P}{\pi(a/2)^2}\left(\sqrt{(a/2)^2 - x^2} - \sqrt{(a/2)^2(1 - \frac{Q}{\mu_k P}) - x^2}\right) \tag{6.14}$$

Figure (6.8) shows the pressure distributions at the contact interface of a semi-circle and a plane for $\delta = 0.1$, $u_x/L = 0.01$ and $\mu_s = \mu_k = 0.5$. The agreement with Hertz and Cattaneo-Mindlin theory is good, but as in the full stick case, an asymmetry is observed.

In addition to the pressure distributions, the size of the stick region c as a function of the tangential load Q can be measured. The Cattaneo-Mindlin solution is

$$\frac{c}{a} = \sqrt{1 - \frac{Q}{\mu_k P}}. \tag{6.15}$$

This is plotted in figure (6.9). The agreement with Cattaneo-Mindlin theory is good, but the discretization effects are large.

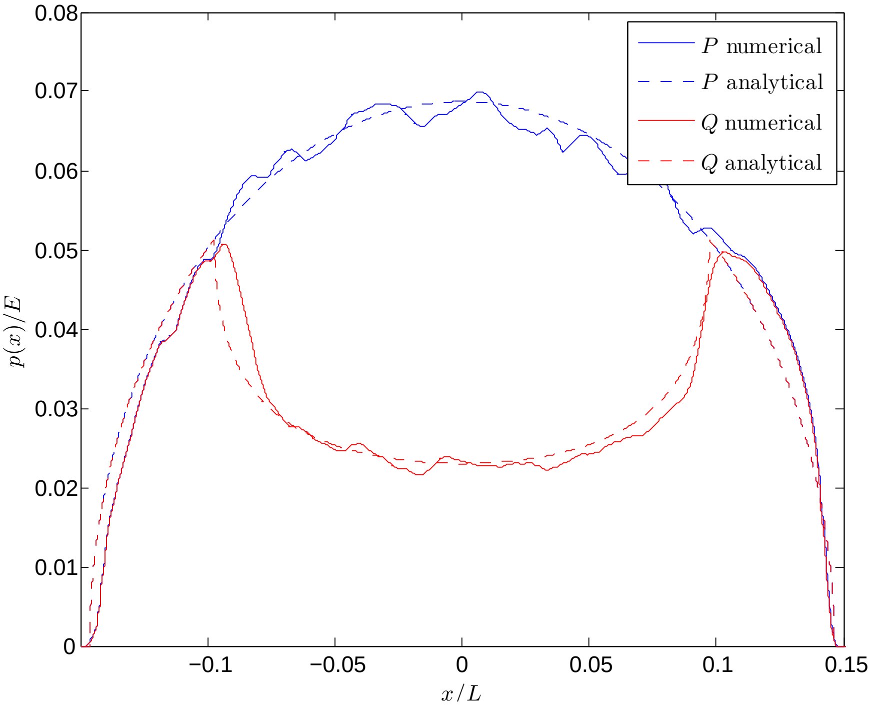

Figure 6.8: *The normal pressure and traction distribution at the contact interface of the semi-circle and the plane assuming* $\mu_s = \mu_k = 0.5$. *The compression is* $\delta = 0.1$, *while the tangential displacement is* $u_x/L = 0.01$. *Dashed lines are analytical predictions by Cattaneo-Mindlin and Hertz theory. The shear force is applied in the negative x-direction, so that the trailing edge of the semi-circle is at the left side of the figure.*

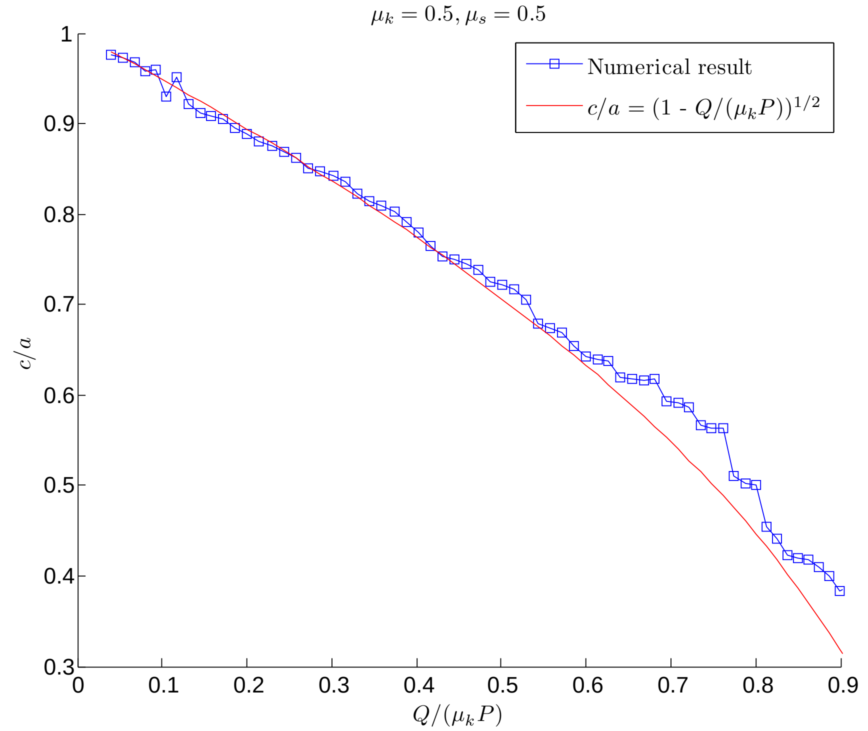

Figure 6.9: *The size of the stick region c as a function of the applied tangential load* Q. *The results are averaged over* 50 *simulations.*

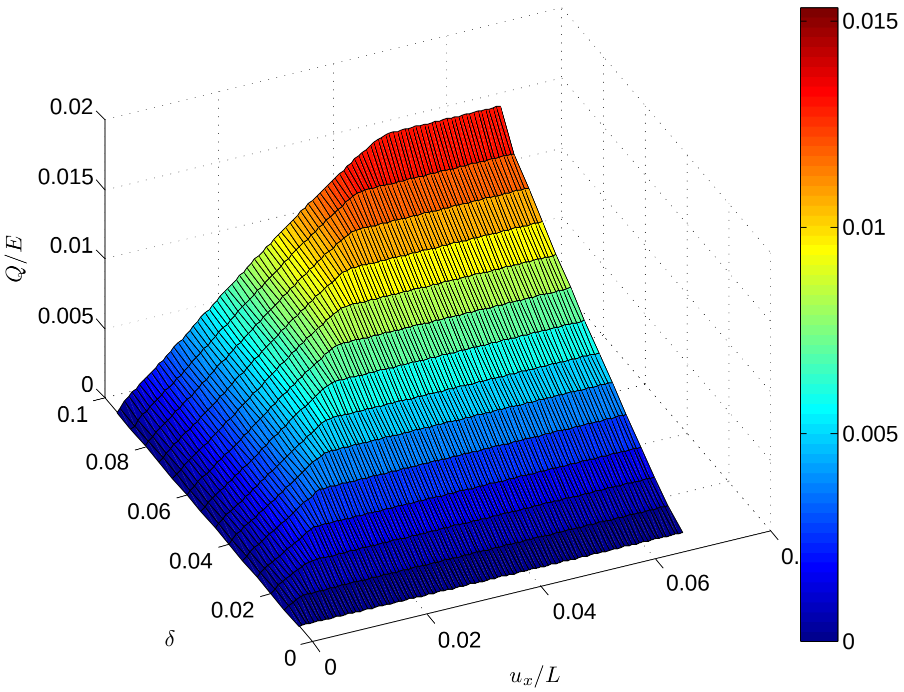

Figure 6.10: *The tangential loading curve of an asperity with applied tangential load Q/E imposed by a displacement u_x/L for different compressions δ. The friction coefficients are $\mu_k = \mu_s = 0.5$*

6.3 Shear stiffness

The shear stiffness is a measure of the opposing force from a material given by a shear displacement. In the following we measure the total shear force Q versus the tangential displacement u_x (the tangential loading curve) and find a scaling relation.

6.3.1 Scaling with δ

The tangential loading curve of the contact will vary with the applied normal load. This is investigated by shearing a single sample at different compressions. An ensemble average is not performed for these simulations since each series of simulation involves many different compressions and is very time consuming. (Simulations show that the total normal load P, and the total tangential load Q do not vary much due to the discretization effects.) The unscaled plot is shown in figure (6.10) for equal friction coefficients $\mu_k = \mu_s = 0.5$. Full slip will occur when the tangential load is equal to the dynamic friction threshold $\mu_k P$. This gives the scaling for the Q-axis with $\mu_k P$. We further suggest that the displacement axis scales with the dimensionless normal load $P/(EL)$. This is shown in figure (6.11). The scaling behavior is quite good, but not perfect. Motivated by this we attempt to scale the displacement axis with the compression δ. This is shown in figure (6.12), and this scaling relation gives a much better data collapse. The only curve that does not fit the collapse is the curve with the

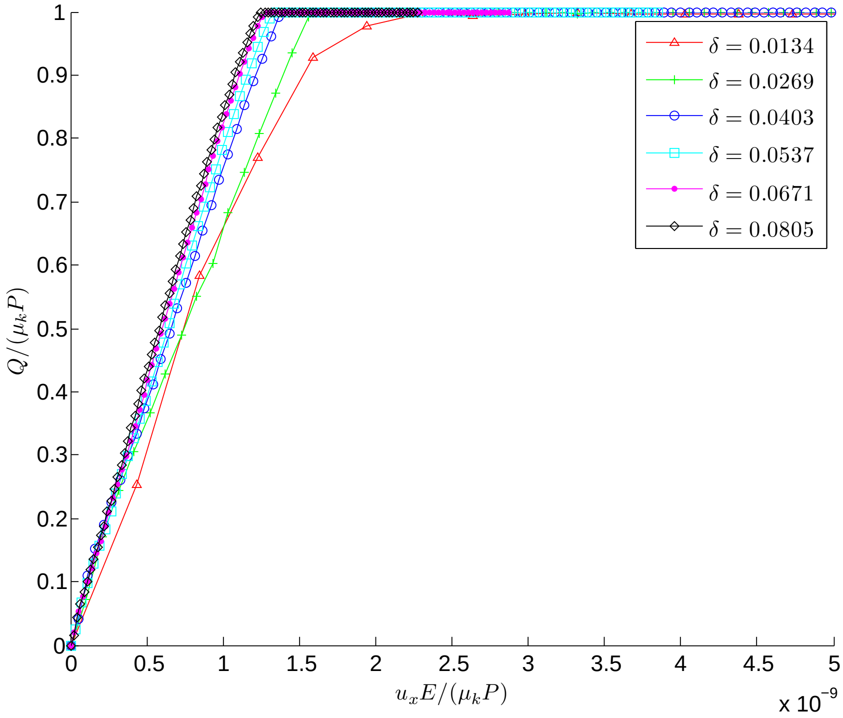

Figure 6.11: *The total tangential load Q as a function of the displacement u_x/L for different compressions. The total tangential load scales with $\mu_k P$, and the scaling attempt at the displacement axis is equal.*

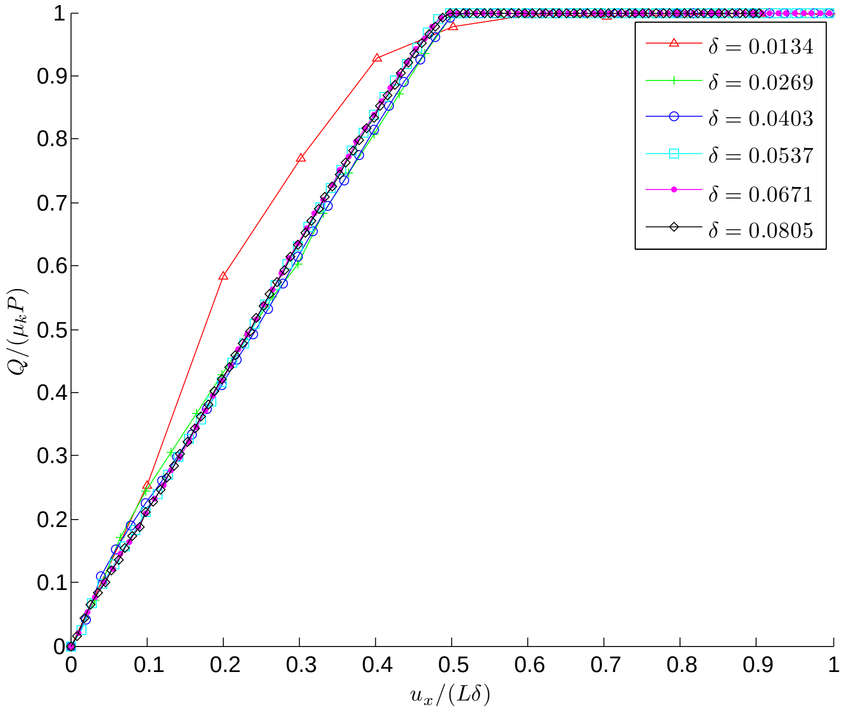

Figure 6.12: *The total tangential load Q as a function of the displacement u_x/L for different compressions. The total tangential load scales with $\mu_k P$, and the displacement axis scales with the compression δ. The slope is $1/\mu_k$*

smallest compression. A probable cause for the discrepancy is that the number of nodes at the contact interface is very small. Cattaneo-Mindlin theory gives an analytical expression for the shear stiffness of spheres, but there is currently no theory on the stiffness of cylinders [4]. We have, however, been able to identify some scaling relations for the stiffness as a function of compression and pressure.

6.3.2 Scaling with μ_k

The tangential loading curve of a contact is measured for different values of μ_k, with the aim of finding a scaling behavior with the friction coefficient. Q/P is measured for three different sets of friction coefficients, and the result is plotted in figure (6.13). We note that we measure the value of the dynamic friction coefficient along the x-axis. A scaling relation using this friction coefficinet would give a crossover at

$$\frac{Q}{\mu_k P} = \frac{u_x}{\mu_k \delta L} \approx 1. \tag{6.16}$$

The scaling of the stiffness with different friction coefficients is linear in μ_k. The Q axis simply scales by $\mu_k P$, and the displacement axis by μ_k. This is shown in figure (6.14). We now have the complete scaling behavior for both δ and μ_k when $\mu_s = \mu_k$ (the scaling with L comes from the introduction of dimensionless variables).

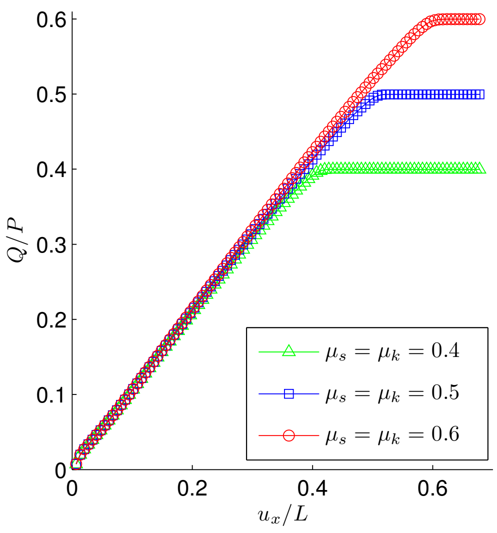

Figure 6.13: *The total tangential load Q as a function of the displacement u_x for three sets of friction coefficients at the same compression. The plot is an average of 50 simulations.*

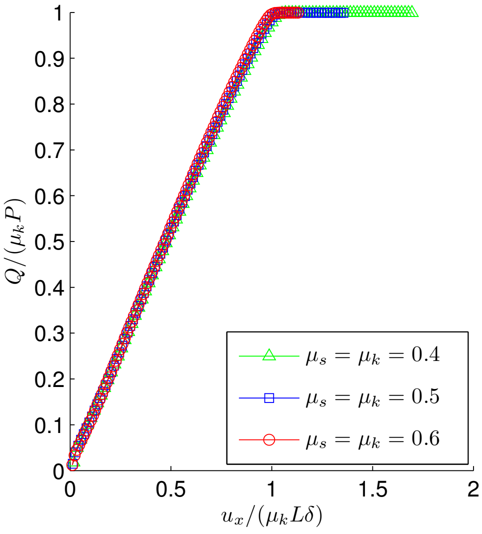

Figure 6.14: *The total tangential load Q as a function of the displacement u_x for three sets of friction coefficients at the same compression. The have a simple scaling behavior with the dynamic friction coefficient μ_k.*

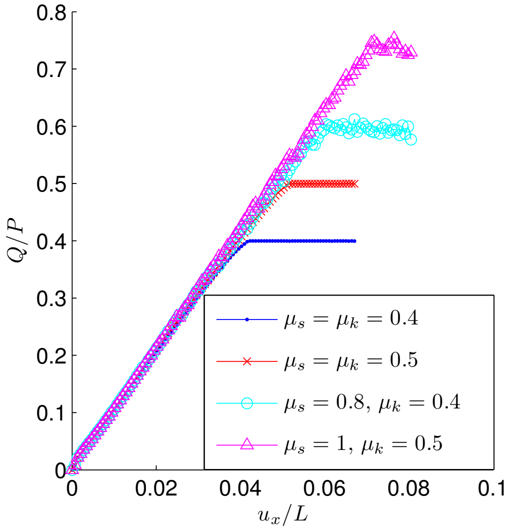

Figure 6.15: *The tangential load Q as a function of displacement u_x for different μ_s and μ_k. In order to highlight the differences between equal and different friction coefficients the curves are not averaged over multiple simulations.*

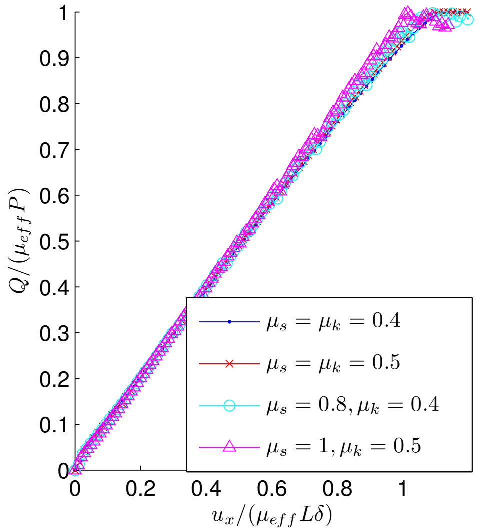

Figure 6.16: *The tangential load Q as a function of displacement u_x for different μ_s and μ_k. In order to highlight the differences between equal and different friction coefficients the curves are not averaged over multiple simulations. The system is scaled with the global static friction coefficient μ_{eff}.*

6.4 Deviations from Cattaneo-Mindlin theory

6.4.1 The role of the static friction coefficient μ_s

Cattaneo-Mindlin theory assumes $\mu_s = \mu_k$, and predicts that $q(x)$ is independent of the static friction coefficient. We investigate the effects of introducing a static friction coefficient $\mu_s \neq \mu_k$. Figure (6.15) shows the tangential loading curve of the semi-circle with sets of friction coefficients. The tangential load does not drop to the dynamic friction level after reaching the global static friction threshold. This is due to the infinitely slow driving. One important question to raise is if it is meaningful to investigate effects of a static friction coefficient in this case, since the system is actually at rest at the end of every iteration. In addition, the normal pressure at the edges of contact is very small. The system would probably not come to rest if the driving was not infinitely slow.

The case with equal friction coefficients is fundamentally different from the case with two different friction coefficients. In that particular case the effects of the infinitely slow driving are small because the traction distribution equals the dynamic friction threshold when the system comes to rest. If the friction coefficients are equal, the static and dynamic thresholds are equal, and the force required to restart the system is negligible. Using two different friction coefficients, the system will be largely affected by the driving because it comes to rest at every iteration step. In order to restart the system, a large amount of force is needed. We proceed with this in mind.

Figure (6.15) motivates a scaling relation using the global static friction coefficient μ_{eff}. In this case

$$\mu_{\text{eff}} \simeq \frac{\mu_s + \mu_k}{2}, \tag{6.17}$$

which might not be the case in general. The scaling relation is plotted in figure (6.16). To highlight the differences between the two cases, results are not averaged over many simulations. We find that systems with the same ratio between the static and dynamic friction coefficient scale equally with μ_k, and it is indeed possible to scale the stiffness with the global static friction coefficient μ_{eff}. Increasing μ_s increases the amount of stress that can be held by the friction force. It also results in a larger stick zone. We attempt the same scaling with μ_{eff} for c/a. Figure (6.17) shows that the stick zone indeed scales with the global static friction coefficient. An explanation for this has not been found.

6.4.2 Asymmetry

Cattaneo-Mindlin theory does not predict the numerically observed asymmetry in the traction distribution $q(x)$ (see figure(6.18)), due to the amplitude and direction of the tangential load Q. The asymmetry is quantified as the displacement of the center of the stick region with respect to the center of the contact interface. We define

$$\Gamma = \frac{1}{a}\left(\frac{c_{\text{left}} + c_{\text{right}}}{2} - \frac{a_{\text{left}} - a_{\text{right}}}{2}\right), \tag{6.18}$$

where left and right denote the edges of the stick region, c, and the contact area, a, respectively. Figure (6.18) shows the asymmetry as a function of the applied tangential load. There is no clear difference between the different sets of friction coefficients. It is also difficult to make precise measurements because it involves both the contact area and the stick zone, which both have large discretization effects. In addition, the asymmetry is small, so these discretization effects are dominating.

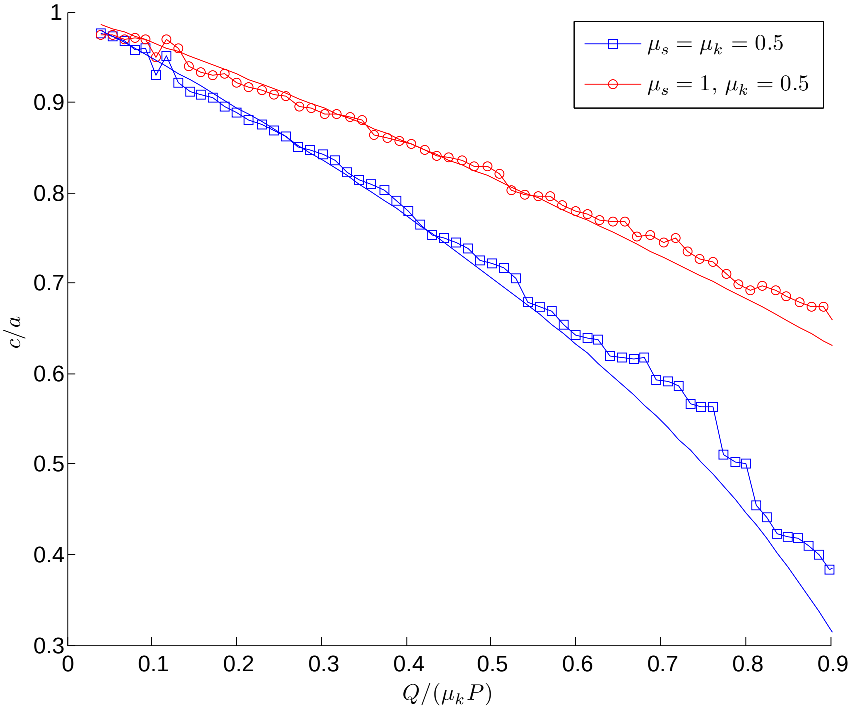

Figure 6.17: *The length of the stick zone as a function of applied tangential load. Analytical predictions were made with μ_{eff}. The results are averaged over 50 simulations.*

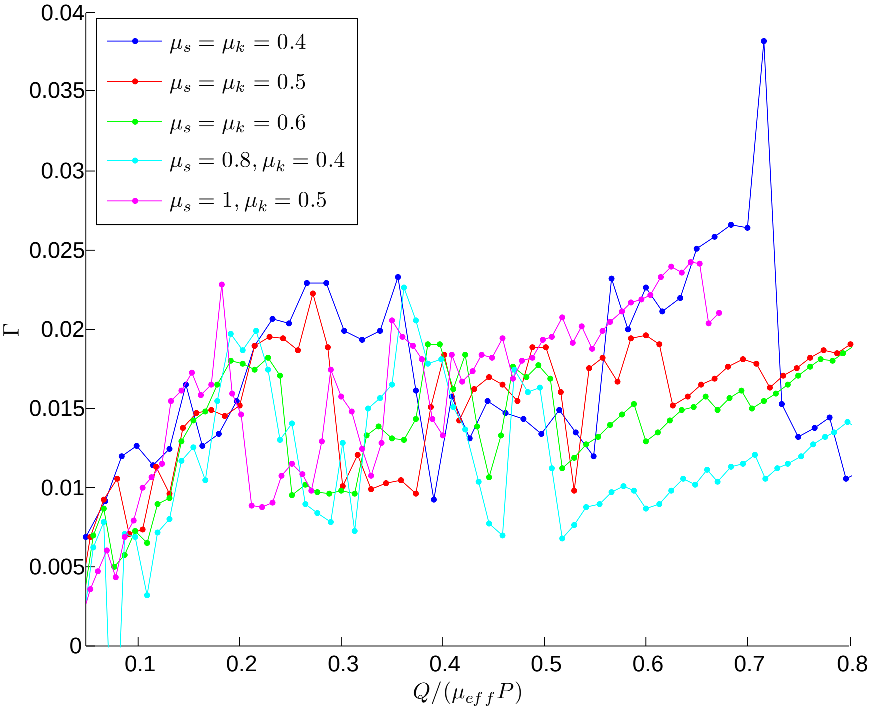

Figure 6.18: *The asymmetry Γ as a function of applied tangential load Q. The discretization effects in the discrete element method are dominating.*

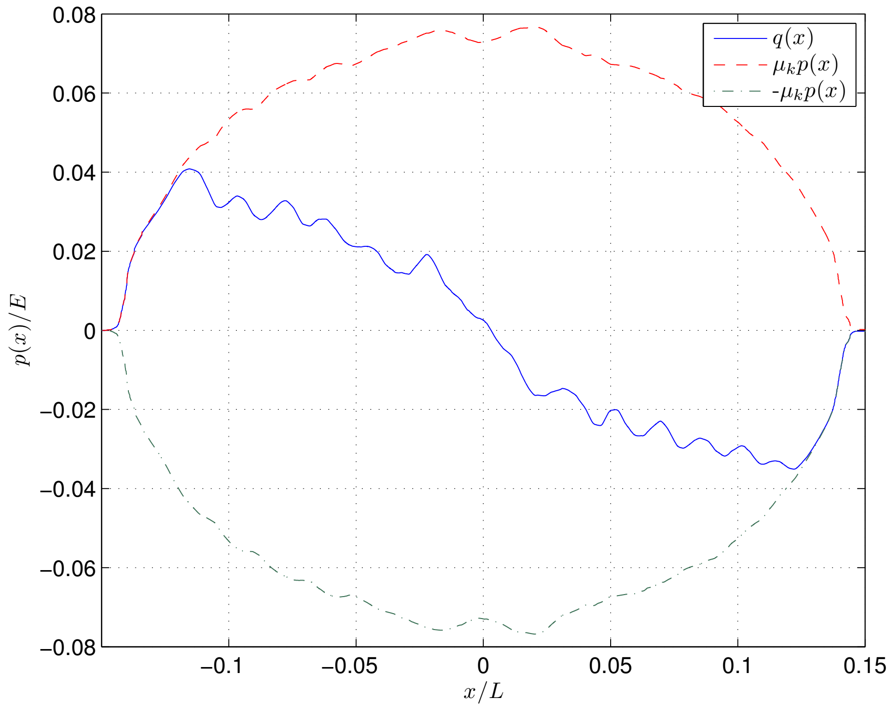

Figure 6.19: *The traction distribution $q(x)$ after a compression $\delta = 0.1$ of a semi-circle with friction coefficients $\mu_s = \mu_k = 0.5$. The distribution is antisymmetric due to the friction force.*

6.4.3 Effects of $\mu_s = \mu_k \neq 0$ during normal loading

The results above were found for a system using frictionless normal loading conditions. This was done to compare the results to the Cattaneo-Mindlin theory. This setup is however unphysical. In a real system, friction will apply during the loading phase as well. In this section we look at different normal loading conditions and how the system responds.

Traction distribution after normal loading

Applying normal pressure to a semi-circle with a friction law will result in an initial shear force distribution. This distribution is plotted in figure (6.19) for $\delta = 0.1$. For the frictionless indentation we had slip at the whole interface during the indentation. With friction there is slip at the edges of contact in opposite directions. This causes the stick region and the asymmetry of the stick region to change significantly. Figure (6.20) illustrates three different friction cases for the semi-circle at $\delta = 0.1$.

- Frictionless normal loading and shear loading with full stick conditions.
- Frictionless normal loading and shear loading with equal friction coefficients $\mu_s = \mu_k$.
- Both normal and shear loading with equal friction coefficients $\mu_s = \mu_k$.

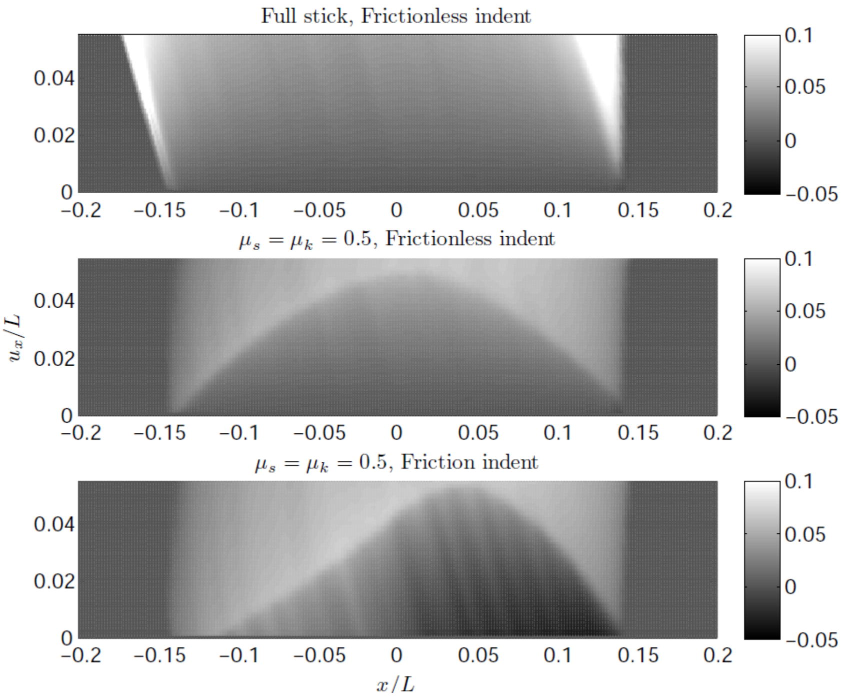

Figure 6.20: *The tangential loading $q(x)/E$ for three different cases of normal loading: Frictionless indent with full stick (top) and equal friction coefficients (middle) during shear, and friction indent with equal friction coefficients (bottom). In the full stick case the contact area is not constant. This is because new contacts form at the leading edge, while no contacts are lost at the trailing edge even though the pressure is vanishing.*

This demonstrates the differences due to the initial loading. The asymmetry and size of the stick region is significantly changed if friction applies during the normal loading phase. The stick region can be seen in figure (6.20) as the darker area with a sharp boundary that decreases as u_x is increased. The increased asymmetry due to friction during the normal loading becomes obvious. As soon as a tangential load is applied, instant slip occurs at the trailing edge. The initial traction distribution is important for the subsequent behavior of the system, a behavior also observed in the one-dimensional spring block model.

Shear stiffness

The shear stiffness is affected by the initial traction distribution. Figure (6.21) shows the tangential load for $\mu_s = \mu_k = 0.5$ after frictional and frictionless normal loading. The stiffness is slightly decreased due to the initial traction distribution. Figure (6.22) shows that the compression scaling behavior found in the frictionless case is still valid.

Stick region

The stick region for a frictional indent behaves quite differently from the frictionless indent due to the applied friction force. During the normal loading there are micro-slips at the edges of the contact moving in opposite directions. When a tangential load is

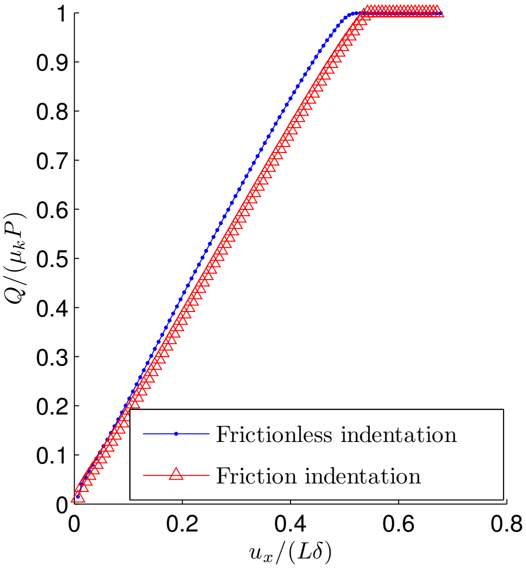

Figure 6.21: *Tangential as a function of the displacement for frictionless loading and with equal friction coefficients $\mu_s = \mu_k = 0.5$.*

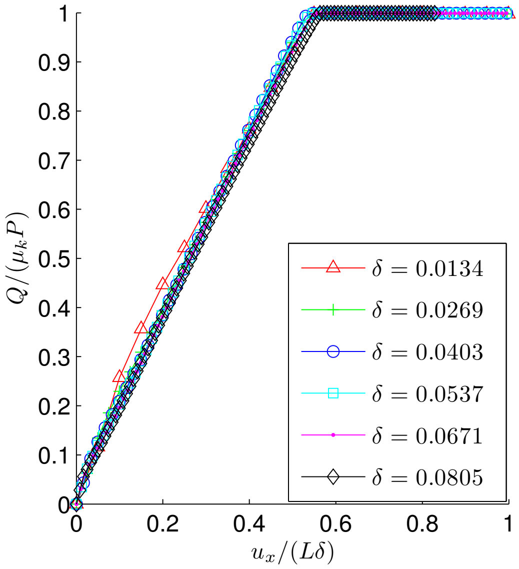

Figure 6.22: *Scaling of the tangential with the compression δ is still valid when the system is loaded with friction.*

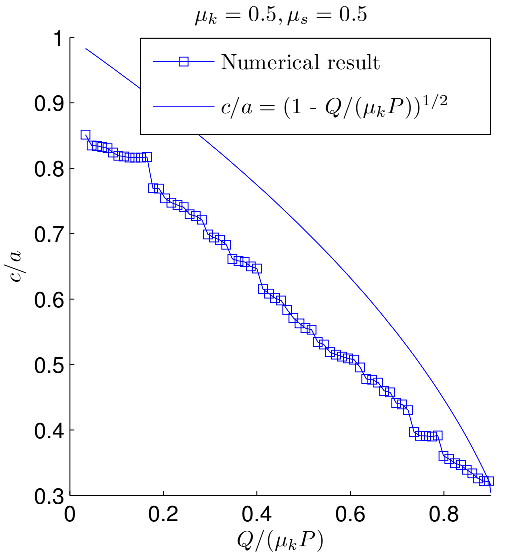

Figure 6.23: *The length of the stick region as a function of the tangential load with equal friction coefficients $\mu_s = \mu_k = 0.5$ during the normal loading.*

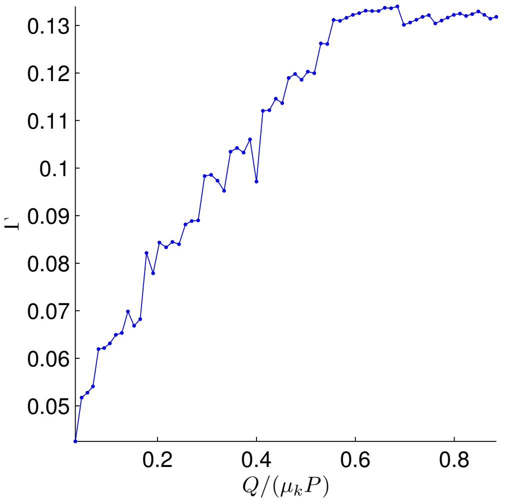

Figure 6.24: *The asymmetry in the stick region after the system is loaded with equak friction coefficients $\mu_s = \mu_k = 0.5$.*

later applied, instant slip occurs at the trailing edge and results in a stick region that is shorter than the Cattaneo-Mindlin prediction. This is plotted in figure (6.23). It demonstrates that the initial traction distribution is important to the behavior of the system, which was also the case in the one-dimensional spring block model.

Asymmetry

Due to the antisymmetric initial traction distribution, the asymmetry in the stick region is very large. This is demonstrated in figure (6.24). The asymmetry increases as the tangential load increases, and is as large as 13%. Results with friction during the normal loading suggest that the Cattaneo-Mindlin theory is not suifficient to describe the changes in the stick region of cylinder on plane contact during tangential loading. This is previously discussed by Nowell [55].

6.5 Stop fronts and the final shear force distribution

Introducing a static friction coefficient in a system where the driving is infinitely slow is somewhat artificial. It might be that the static friction coefficient has an important role, but the traction distribution will have a stronger dependence on the dynamics of the system if two friction coefficients are used. Since a quasi-static model is used it may be that the results with two different friction coefficients are unphysical and cannot be trusted. In order to test this further we measure the stop fronts in the system with two different friction coefficients. The friction coefficients are set to $\mu_s = 0.2$ and $\mu_k = 0.1$ with $\delta = 0.1$. Due to the low friction coefficients, full slip is obtained with $u_x/L = 0.1$. As seen in figures (6.25) and (6.26), the stop fronts tend to propagate from the middle where the normal pressure is high, and hence also the friction force is largest. The final tangential load Q is measured as a function of the nucleation point of the stop front, and as a function of the extent in time of the event $(t - t_0)$ in number of iterations. There is no clear trend as to how the system ends up due to the duration of the event. For stop fronts nucleating from the center the tangential load has a small tendency to increase.

6.6 The semi-circle in the 1D friction model

One can insert the expressions for the normal pressure distribution and the traction distribution in the 1D top driven friction model. Discretizing the Hertz and Cattaneo-Mindlin result we find

$$w_i = p_0\sqrt{1 - \frac{(2ai/(N-1) - a)^2}{a^2}}, \tag{6.19}$$

and

$$\sigma_i = \frac{Q}{\pi\sqrt{a^2 - (2ai/(N-1) - a)^2}}. \tag{6.20}$$

Figure(6.27) shows the behavior in time for a system with an initial shear force distribution set to that of full stick. Even though the systems are not directly comparable due to the momentum and the missing second dimension, we see that the the two models

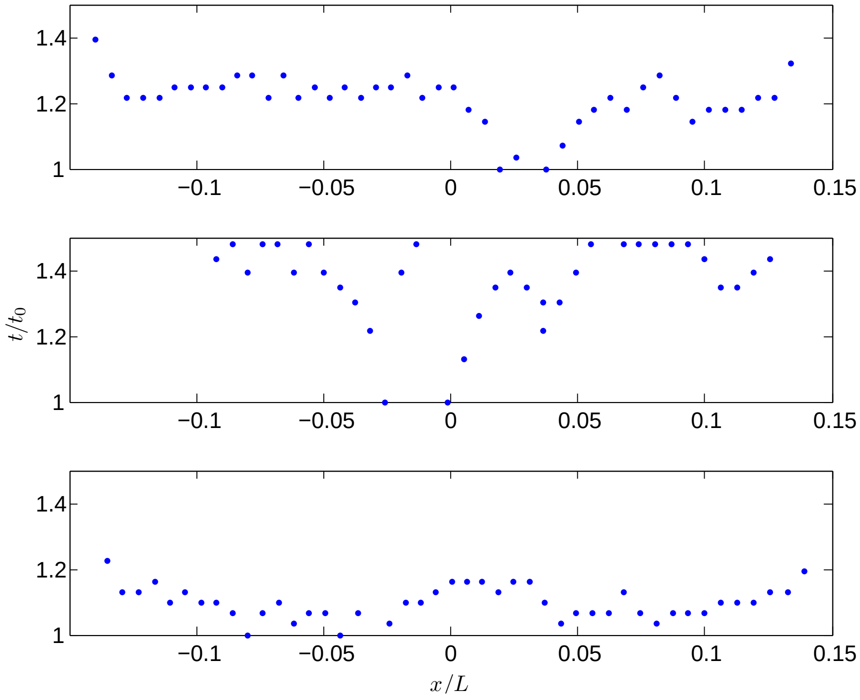

Figure 6.25: *Three stop fronts as functions of time in case of a the semi-circle compressedion $\delta = 0.1$ after full slip has occurred. The stop fronts tend to nucleate from the middle of the sample.*

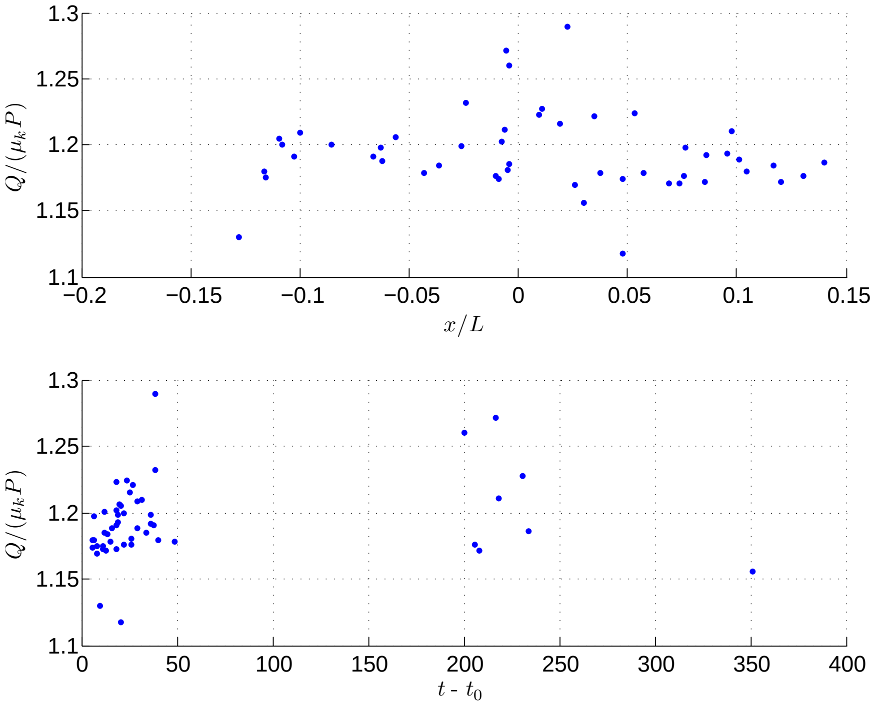

Figure 6.26: *The final tangential load Q as a function of the nucleation point of the stop front (top). The dots show the starting point of the stop front along the contact interface and the total shear force after the system has come to rest. The final tangential load Q as a function of the length of the stop event (bottom). The dots show the total time of the stop event and the total shear force after the system has come to rest.*

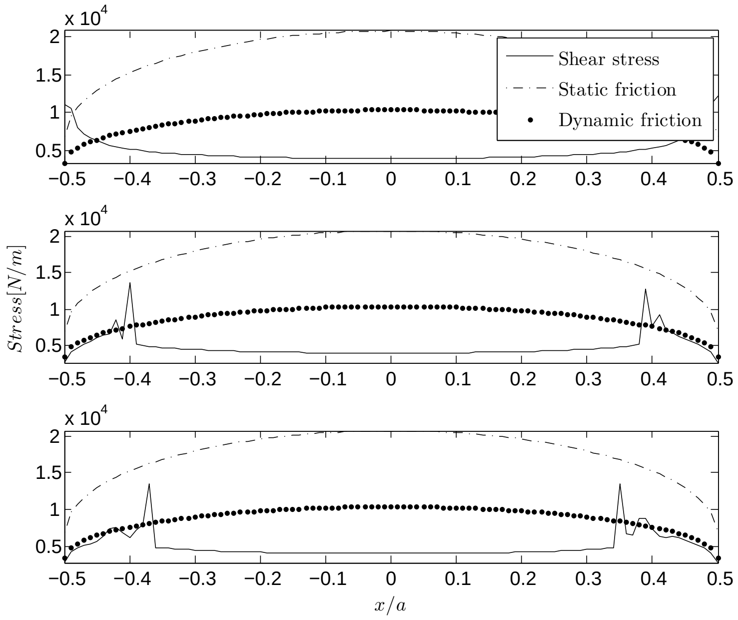

Figure 6.27: The circle friction problem inserted in the Burridge-Knopoff model. The initial state (top), during slip (middle) and when the system is at rest (bottom). The spikes are caused by discretization effects, and the fact that one block has to move in order to transfer stress to its neighbor. The friction coefficients are $\mu_s = 1$, and $\mu_k = 0.5$. $m = 1$, and $N = 101$. The cross-sectional area $S = 10^{-4}$. This figure compares to figure (6.6).

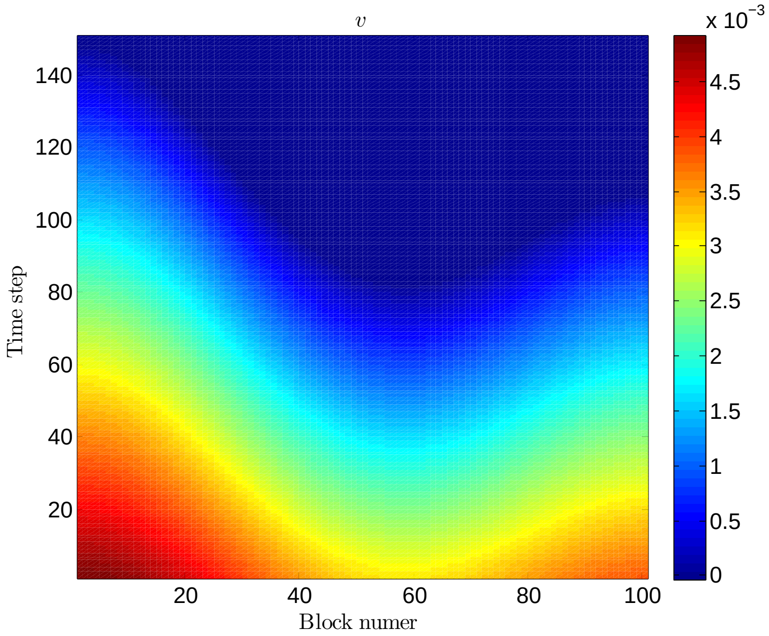

Figure 6.28: The stop front in the 1D top driven Burridge Knopoff model with a low viscous damping coefficient ($\nu = \sqrt{0.01mk}$). The system is initialized with the analytical expressions for the shear and normal force distributions for the semi-circle. The color indicates the local block velocity.

behave similarily. The dynamics in this system is explicitly solved, and the result is used as a method to test the dynamics of the stop fronts in the quasi-static model.

6.6.1 Stop fronts in the 1D model

In order to verify the stop fronts found in the two-dimensional model, they can be compared to the one-dimensional top driven spring block model. The system is initialized with the shear force distribution from the full stick case so that full slip is obtained. Figure (6.28) shows that a stop front that nucleates at the center of the contact is found in both models, suggesting that the introduction of a static friction coefficient in the two-dimensional equilibrium model may be valid.

6.7 Discussion

One aim of this chapter is to find the tangential loading curve of a single asperity. We have found the scaling relation for a single contact with the friction coefficient μ_k and the surface compression δ. This can be used to estimate the tangential loading curve of a rough surface assuming that the asperities are semi-circles and that they are elastically independent. Further, the effect of the static friction coefficient μ_s is investigated. The system scale with the global static friction coefficient μ_{eff}, but this might be an effect of the infinitely slow driving, and should be further investigated using a time integration algorithm. The stop fronts with two different friction coefficients are reproducible in the one-dimensional spring block model.

The results in this chapter show that Cattaneo-Mindlin theory is not sufficient to describe a system when friction applies during the normal loading. It does, however, give useful insight to the general behavior of the tangential loading of a micro-contact. The asymmetries due to the initial loading are far too large to be neglected. One of the problems with the Cattaneo-Mindlin theory is that it does not explain junction growth. There is a small increase in the contact area if the system was loaded with friction conditions, but it is not large enough to explain the junction growth found experimentally [63]. This suggests that there is some mechanism not included in this model that is responsible for the experimentally observed junction growth. A different numerical approach may be needed to explain this, e.g. a molecular dynamics approach [64].

Some of the calculations in this chapter were also carried out using a commercial finite element solver. The results are discussed in appendix C. A semi-circle connected with a large rectangular block with a higher Young's modulus was used to compare results with frictionless indentation and equal friction coefficients during shear loading. Similar results are found, and the discretization effects are small.

The scaling behavior obtained for the loading curve of an asperity will be used in the next chapter to develop a theory for the loading curve of a rough surface in two dimensions.

Chapter 7

Rough surfaces

In chapter 6 we studied the behavior of a single contact. In this chapter, we use the one-contact results to find a general behavior of a larger rough surface assuming the roughness occurs at a single length scale, and that the contacts are elastically independent. We further use the discrete element code to model rough surfaces in order to test the validity of this theory for two different kinds of surfaces: The self-affine, and the gradient percolation surface. The model works for well for the self-affine surface, while the results for the gradient percolation surface are not very conclusive. The results are included to show that some systems exhibit non-trivial behavior. In this chapter $\mu_s = \mu_k$.

7.1 A Boitnott approach to the scaling of the shear stiffness of a rough surface

The scaling relations for the tangential loading curve of a single asperity found in chapter 6 can be used to estimate the tangential loading curve of a rough surface. We assume that the rough surface consists of elastically independent semi-circles of equal radius at different compressions given by the height distribution of the surface. The same approach has been used by Boitnott in three dimensions with spheres [40]. We estimate a general solution of the tangential load for a single contact i, Q_i, by the compression δ_i, its size l, and the friction coefficient μ_k. In chapter 6 We saw that Q_i increased almost linearly with u_x until a sharp transition at a critical displacement (figure (6.12)). We define the critical displacement of asperity i as $u_{c,i}$. This gives

$$Q_i = \begin{cases} \frac{u_x}{\mu_k \delta_i l} P_i & u_x < u_{c,i} \\ \mu_k P_i & u_x \geq u_{c,i}. \end{cases} \tag{7.1}$$

l The critical displacement is a function of the compression

$$\frac{u_{c,i}}{\mu_k \delta_i l} = 1, \tag{7.2}$$

so that

$$u_{c,i} = \mu_k l \delta_i. \tag{7.3}$$

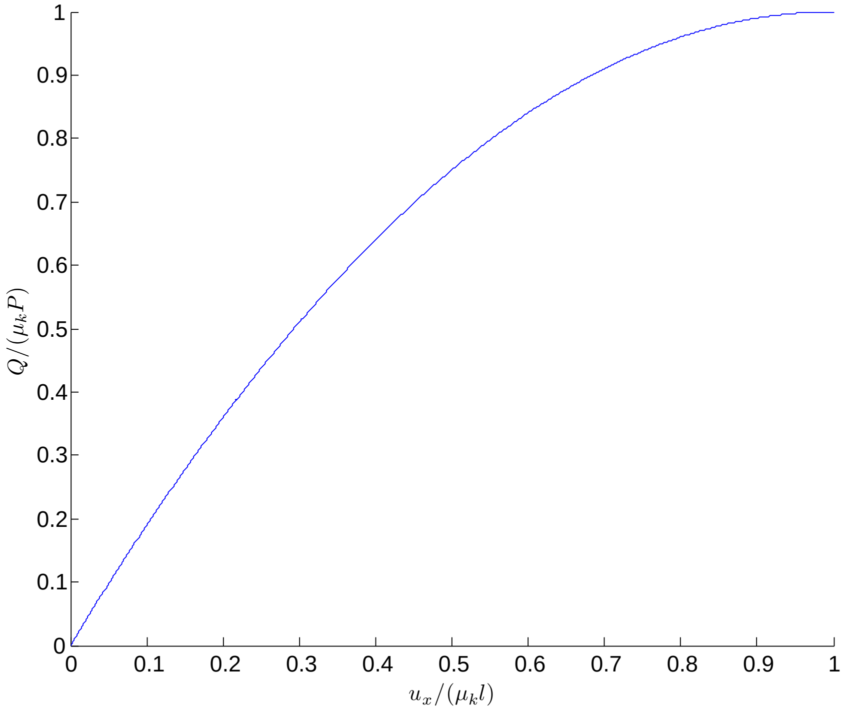

Figure 7.1: *Analytical prediction of tangential load* Q *scaled with the normal load* P *and the friction coefficient* μ_k *as a function of the displacement* $u_x/(\mu_k l)$ *assuming a linear relation between the global compression* δ *and the normal load* P*.*

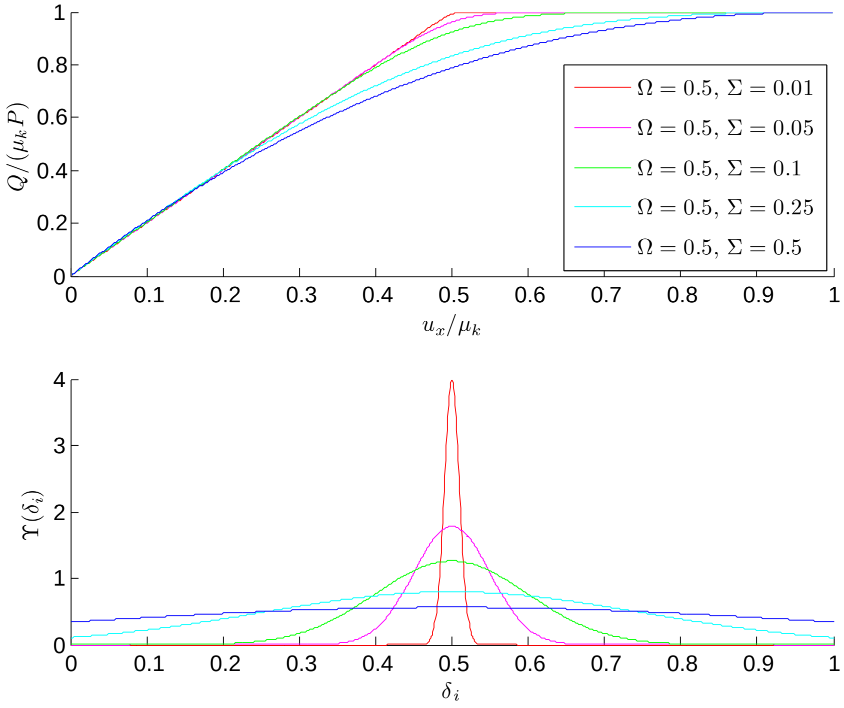

Figure 7.2: *The tangential loading curve* $Q/(\mu_k P)$ *of a surface (top) that is rough on a single length scale for different distributions of compressions (bottom). The integrals are evaluated numerically with* $\beta = 1.31$*.*

We further use the scaling relation between the pressure and the compression (equation (6.7))

$$P_i = \alpha \delta_i^{\beta}, \tag{7.4}$$

where α is a constant, and $\beta = 1.31$. This gives

$$Q_i = \begin{cases} \frac{u_x}{\alpha l}(\frac{1}{\delta_i})^{1-\beta} & u_x < u_{c,i} \\ \mu_k \alpha \delta_i^{\beta} & u_x \geq u_{c,i}. \end{cases} \tag{7.5}$$

We further assume a surface that is rough at a single length scale (i.e. l is a constant), where the micro-contacts are elastically independent. The problem then reduces to integrating Q_i over a compression distribution $\Upsilon(\delta_i)$. Equation (7.5) is difficult to integrate because $u_{c,i}$ is a function of the compression. We rewrite the expression as [1]

$$Q_i = \lim_{\gamma\to\infty} \alpha\delta_i^{\beta}\left(\frac{\arctan(\gamma(u_x - \mu_k l\delta_i)) + \pi/2}{\pi}\left(\mu_k - \frac{u_x}{l\delta_i}\right) + \frac{u_x}{l\delta_i}\right), \tag{7.6}$$

We further assume that we have some distribution of compressions $\Upsilon(\delta_i)$, so that the behavior of the global Q is

$$Q = \lim_{\gamma\to\infty} \frac{\int_{\delta_i} \alpha\delta_i^{\beta}\left(\frac{\arctan(\gamma(u_x-\mu_k L\delta_i))+\pi/2}{\pi}\left(\mu_k - \frac{u_x}{l\delta_i}\right) + \frac{u_x}{l\delta_i}\right)\Upsilon(\delta_i)d\delta_i}{\int_{\delta_i}\Upsilon(\delta_i)d\delta_i}. \tag{7.7}$$

This integral can be evaluated analytically if $\beta = 1$ and $\Upsilon(\delta_i) = 1$ for $\delta_i \in (0, 1)$ which gives

$$\begin{aligned} Q = \frac{\alpha}{4l^2\mu_k}\Bigg(l\mu_k\Bigg(l\mu_k - \sqrt{(u_x - l\mu_k)^2}\Bigg) + u_x\Bigg(\mu_k\Bigg(\sqrt{u_x^2} - \sqrt{(u_x - l\mu_k)^2}\Bigg) \\ +2\Bigg(- \sqrt{u_x^2} + L\mu_k + \sqrt{(u_x - L\mu_k)^2}\Bigg)\Bigg)\Bigg). \end{aligned} \tag{7.8}$$

It can be evaluated numerically for any distribution $\Upsilon(\delta_i)$ and any β. In order to scale the Q-axis, the total normal load of the system is needed. Since the compression distribution is uniform, the pressure is linear, and

$$P = \int_0^1 \alpha P_i dP_i = \frac{\alpha}{2}. \tag{7.9}$$

We arrive at

$$\begin{aligned} \frac{Q}{P} = \frac{1}{2l^2\mu_k}\Bigg(l\mu_k\Bigg(l\mu_k - \sqrt{(u_x - l\mu_k)^2}\Bigg) + u_x\Bigg(\mu_k\Bigg(\sqrt{u_x^2} - \sqrt{(u_x - l\mu_k)^2}\Bigg) \\ +2\Bigg(- \sqrt{u_x^2} + l\mu_k + \sqrt{(u_x - l\mu_k)^2}\Bigg)\Bigg)\Bigg). \end{aligned} \tag{7.10}$$

Note that α vanishes when scaling with the normal load. The curve also scales with μ_k as shown in figure(7.1). The shape of the curve is determined by the compression distribution. The micro-contacts reach full slip at different u_x, hence the curvature. Equation (7.7) can be solved numerically for any compression distribution $\Upsilon(\delta_i)$, and

---

[1] $\lim_{\gamma\to\infty}\arctan(\gamma x)$ is a step function. Moving the limit outside of the integral enables us to solve the integral analytically.

for any value of β. A numerical evaluation of the integral will hopefully give a scaling behavior of a rough surface as a function of the compression distribution. We introduce the Gaussian distribution

$$\Upsilon(\delta_i) = \frac{1}{\sqrt{2\pi\Sigma^2}} e^{-\frac{(\delta_i-\Omega)^2}{2\Sigma^2}}, \tag{7.11}$$

where Σ is the standard deviation and Ω is the mean. The tangential loading curves for Gaussian distributions with different Ω and Σ are shown in figures (7.2), (7.3) and (7.4). The compression distribution is not necesserily Gaussian. It may be on the form

$$\Upsilon(\delta_i) \sim \left(e^{-\frac{(\delta_i-\xi_1)^2}{\xi_2}} - e^{-\frac{(\delta_i+\xi_1)^2}{\xi_2}} \right), \tag{7.12}$$

where ξ_1 and ξ_2 are functions of the roughness and the magnification (this is Persson's predictions for the height distribution for the whole surface topography [37]. The reader should note that we want a distribution of the compression of asperities, which is not necesserily equal.) The resulting loading curves show that the underlying compression distribution of contacts is important, and that it will be difficult to find a good scaling behavior if this distribution changes with the normal load.

What seems to govern the shear stiffness of a surface is the fact that asperities reach full slip at different displacements u_x. As asperities slip, the shear stiffness is weakening, until full slip is obtained when the region with the highest normal load slips. The developed theory does not assume a small displacement, and should be valid for all u_x. It does however assume that the elastic interactions between asperities is negligible, and that all asperities can be modeled as semi-circles in contact with a plane. Results will be different if rough on rough contact is assumed. In addition, a constant asperity size l is assumed. A probability distribution in l could be introduced instead. However, this has not been investigated.

In order to test the theory, we use the discrete element method to model a rough surface. There are many different ways to model a surface. We will focus on two types of surfaces. A self-affine surface defined by the Hurst exponent H and the cutoff length l between asperities, and a fractal surface with complex overhangs defined by the fractal dimension D.

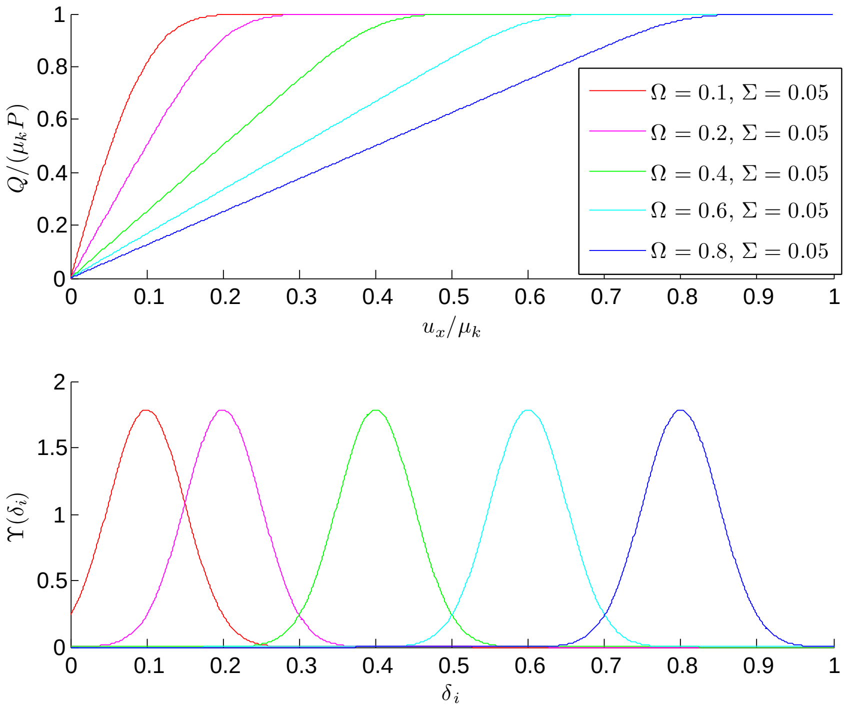

Figure 7.3: *The tangential loading curve of a surface (top) that is rough on a single length scale for different distributions of compressions (bottom). The integrals are evaluated numerically with* $\beta = 1.31$.

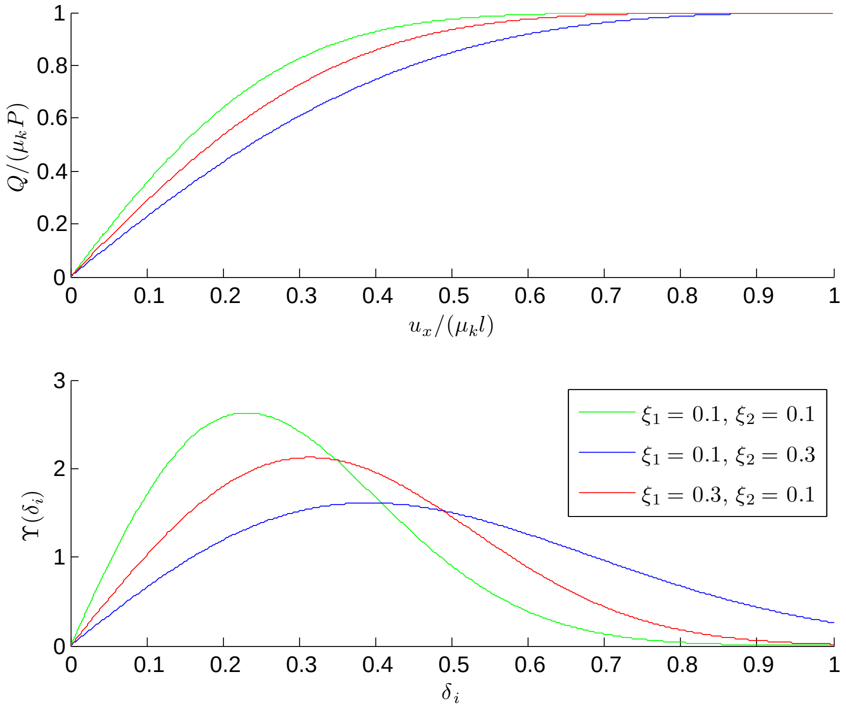

Figure 7.4: *The tangential loading curve (top) of a surface that is rough on a single length scale for different distributions of compressions by equation (7.12) (bottom). The integrals are evaluated numerically with* $\beta = 1.31$.

7.2 Self-affine roughness

To classify self-affine roughness of a surface, one can use the Hurst exponent H. The root mean square value of the change in height $\mathrm{d}h$ over a surface distance x scales as a power law [56], where the exponent is the Hurst exponent.

$$\mathrm{d}h \sim x^H. \tag{7.13}$$

7.2.1 Initializing self-affine roughness

Random surfaces with a given Hurst exponent can be generated using several methods. We use a random midpoint displacement method, which is an iterative method [65]. The outline of the method is shown in figure (7.5). The height of the midpoint and the end points are selected using a random function

$$\mathrm{d}h_1 = a_0(\mathrm{d}x_1)^H \times ran \in (-0.5, 0.5), \tag{7.14}$$

where $\mathrm{d}h$ is the change in height, and $\mathrm{d}x$ is the distance from the previously calculated end points

$$\mathrm{d}x_i = \left(\frac{1}{2}\right)^i. \tag{7.15}$$

The heights of the next points are found by linear interpolation. A random number

$$\mathrm{d}h_2 = a_0(\mathrm{d}x_2)^H \times ran \in (-0.5, 0.5) \tag{7.16}$$

is added to the height. The iteration continues until all points are found.

$$\mathrm{d}h_i = a_0(\mathrm{d}x_i)^H \times ran \in (-0.5, 0.5). \tag{7.17}$$

Three different surfaces generated by the random midpoint displacement method are plotted in figure (7.6)

An additional length scale l, that represents the characteristic asperity size is introduced.

$$l = \frac{L}{2^{n_{\text{peak}}}}, \tag{7.18}$$

where n_{peak} is the number of peaks at length L. In the following calculation $n_{\text{peak}} = 4$. The triangular lattice is not continuous, so the final surface used is a best fit to the calculated surface using the random drop method. Nodes are placed at the surface positions and at random positions in the bulk. Iterations with $\varepsilon = 10^{-2}$ and gives the final surface (the surface nodes are not moving during these iterations).

7.2.2 Measuring the Hurst exponent

The Hurst exponent can be measured using the height difference correlation function [66]. If a surface is given by a function $y(x)$, we calculate

$$C_2(x) = \sqrt{\frac{\sum_{i=1}^{N-x}(y(i) - y(i+x))^2}{N - x}} \tag{7.19}$$

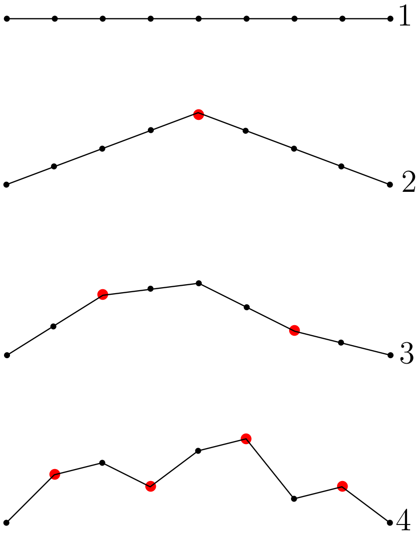

Figure 7.5: *Scheme showing the random midpoint displacement method. A rough surface is generated from an array of N_x points separated by the lattice spacing a_0. Iteratively, the midpoints (large red dots) of an interval, that decreases at every step, are moved according to equation (7.13).*

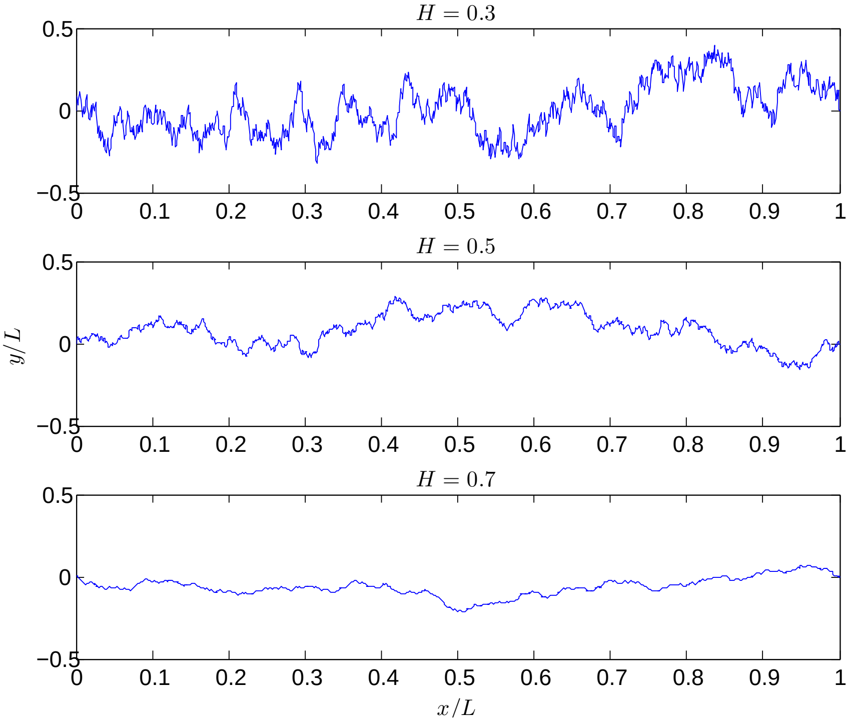

Figure 7.6: *self-affine surfaces generated with Hurst exponents* 0.3 *(top),* 0.5 *(middle) and* 0.7 *(bottom) with* $l = L$ *(*$n_{peak} = 0$*), and* $Nx = 2^{10}$.

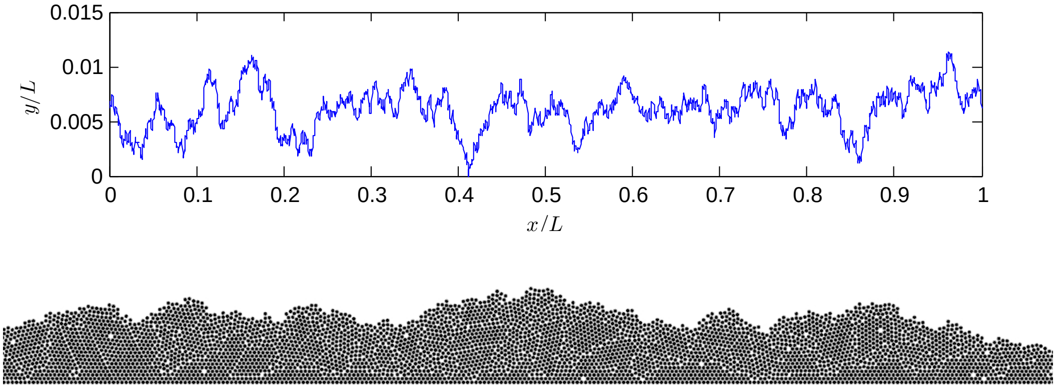

Figure 7.7: *Top: The surface profile of a material initialized with* $H = 0.5$ *and* $l = \frac{L}{2^4}$*. Bottom: Part of the same surface generated with the random drop method.*

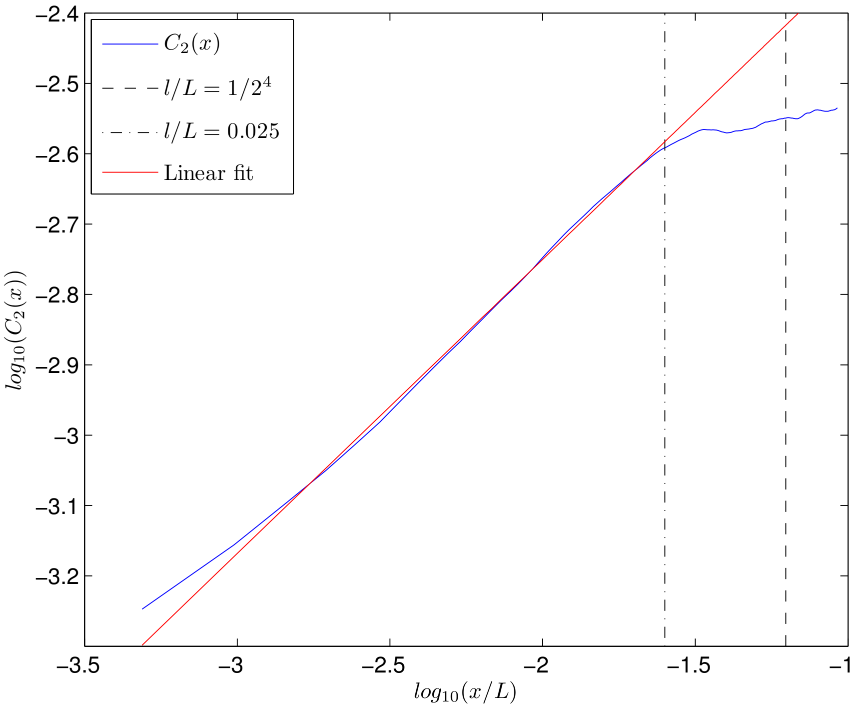

Figure 7.8: *Plot of the heigth correlation function* $C_2(x)$ *used to measure the Hurst exponent of the surface shown in figure (7.7). The exponent is estimated to be* 0.42*. The obtained cutoff length is also different from the initialized. We find* $l/L \approx 10^{-1.6}$*.*

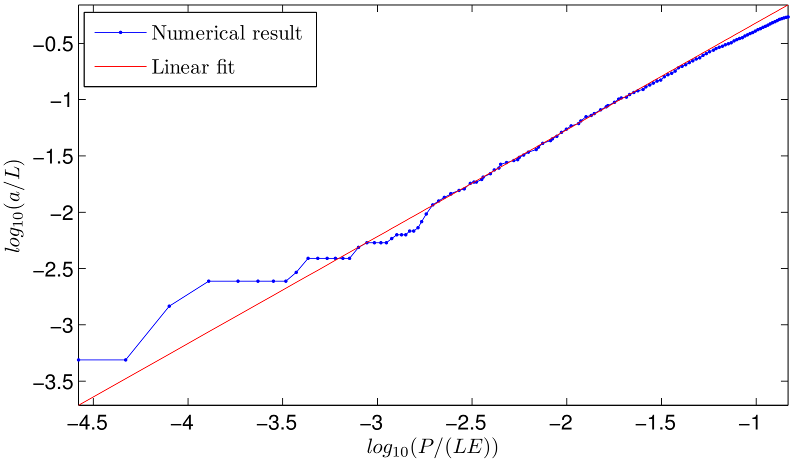

Figure 7.9: *The contact area as a function of the applied pressure. The behavior is close to linear (a power law with an exponent 0.95). Initially there are some discretization effects due to few contact points. This is due to a finite system size.*

which scales as equation (7.13). A logarithmic plot of $C_2(x)$ gives the Hurst exponent of the surface as the slope of the plot. When introducing a second length scale l the differences between the initial and measured value of the Hurst exponent increase. This is due to the increased discretization effects a second length scale introduces and the limitations of a finite sized system. An alternative measure frequently used to determine the roughness of a surface is the power spectrum [1].

7.2.3 Numerical results

Figure (7.7) shows the surface generated with a Hurst exponent $H = 0.5$ and $l/L = 1/2^4 = 0.0625$, while the height correlation function $C_2(x)$ is shown in figure(7.8). The measured Hurst exponent is $H \approx 0.42$. The exponent is difficult to measure precisely due to the characteristic length scale l, which partly explains the deviation from the initial value of 0.5. The measured characteristic asperity size is $l/L \approx 10^{-1.6} = 0.0251$, which is also different from the initialization value.

The boundary conditions are as follows: The bottom of the material is glued to a rigid body. The compression is made using a potential surface with $k_{\text{pot}} = 1000k$. Friction coefficients $\mu_s = \mu_k = 0.5$ apply both during normal and shear loading. The simulations are done with a small bulk ten nodes thick.

Frictional indentation

The contact area as a function of the total normal load is plotted in figure (7.9). The plot shows a power law with an exponent of 0.95. For very large areas, the power law breaks down, since the contact area fraction can never be larger than 1. This is consistent with experimental results [16].

We measure the total normal load P on the surface and the contact area, a, as functions

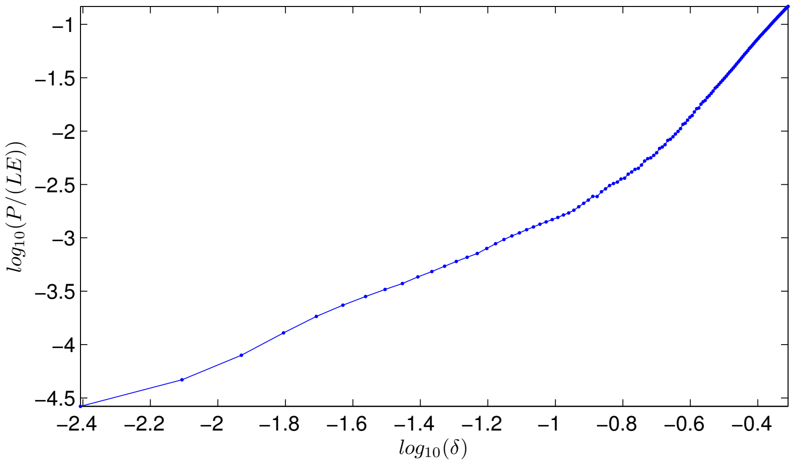

Figure 7.10: *The pressure as a function of the compression δ for a self-affine surface. The obtained result is neither an exponential function (predicted by Persson), nor a power law (predicted by Roux-Schmittbuhl).*

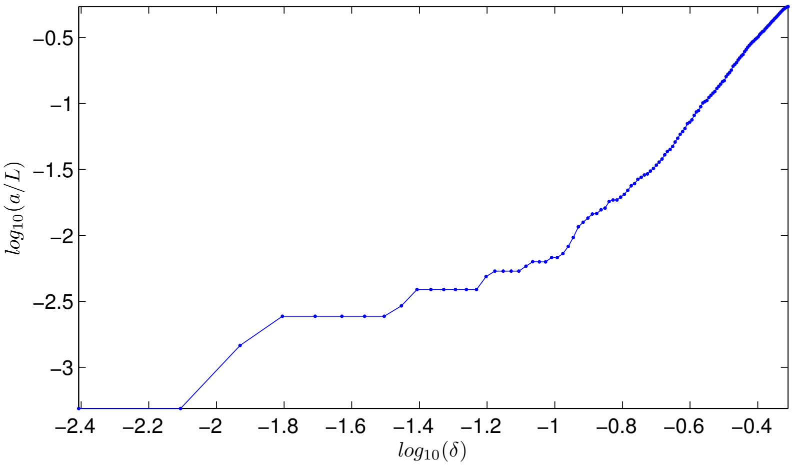

Figure 7.11: *The contact area as a function of the compression δ. Since the area scales linearly with the pressure, the trend in the curve is equal to that of the pressure versus the indentation, with a small difference due to some discretization effects in the calculations of the contact area.*

of the surface compression δ. This is shown in figures (7.10) and (7.11). The theory of Roux and Schmittbuhl predicts a power law with an exponent of exactly 1 for small indentations. The observed exponent for small compressions is larger than 1 (approximately 1.30). In this regime contacts keep forming while the elastic deformations of the surface layer remain small. For larger values of δ, the system enters a regime where the elastic response of the system is important, and the theory of Roux and Schmittbuhl breaks down.

Persson theory predicts that the normal load versus compression is an exponential function [37]. This is not observed. It may be that a three-dimensional system is necessary to observe an exponential behaviour.

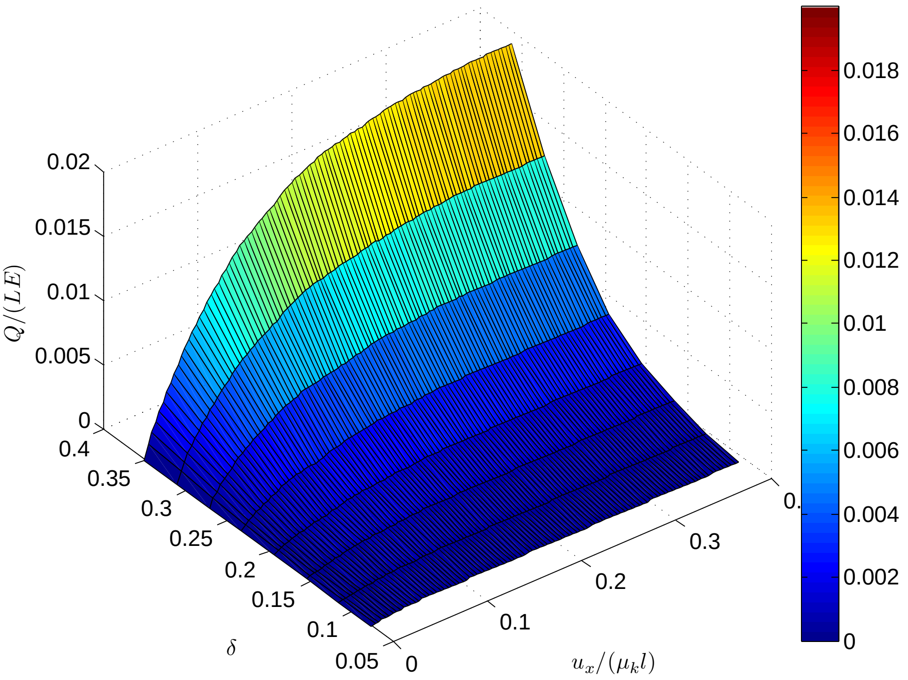

Figure 7.12: *The tangential loading curve of a self-affine surface for different compressions δ.*

For this particular sample, neither of the theories seem fit with the numerical observations. This might be due to various effects. A finite system size is used, and the number of contacts may be too small to obtain the analytical scaling predictions. The shape of the curve and the two different regimes may suggest that an exponential scaling behavior is not that far from what is observed. The regime of very few contact points may be an unphysical regime that will give results with large discretization effects. To test this further a larger number of samples for different values of H should be used. Unfortunately, I did not have time to pursue this further, and it is considered as a possible future project.

Due to the linear scaling behavior of the contact area versus the pressure, the relation between the contact area and the compression is equal to that of the pressure and the compression. This is shown in figure (7.11). For small δ the discretization effects are large because the number of contacts is small.

Shear

The sample is further subjected to a tangential displacement u_x resulting in a tangential load Q. The friction coefficients are $\mu_s = \mu_k = 0.5$. Figure (7.12) shows the tangential load as a function of the displacement for different surface compressions δ. We attempt to scale the tangential loading curve with μ_k and δ. Figure (7.13) shows the attempted scaling, which is identical to the scaling of a single asperity. A full data collapse is however not achieved. From the theory developed in section 7.1 the underlying compression distribution is important to the global behavior of Q/P.

At the length scale l, the surface is generated by a uniform random distribution. Noting this, we assume a uniform compression distribution $\Upsilon(\delta)$ at the length scale $l = 0.025$ which was measured in figure (7.8). Using the power law exponent $\beta = 1.3$ obtained in chapter 6 relating the total normal load P to the compression δ, we can use the theory developed in section 7.1. Figure (7.14) shows this fit. The global theoretical and numerical behaviors are similar, but the details are quite different. The rescaling of the compression distribution imposes equal initial and final points of the numerical and theoretical loading curves. The curve also has to be convex because more and more asperities are slipping. The quality of the fit then relies on the details of the tangential loading curve, which are rather different.

In addition, the bottom layer boundary conditions prohibits long range elastic interactions, which are also neglected in the Boitnott theory. It is not clear at this point whether these interactions are actually important.

The fit is better for small values of the compression, and the error increases as the compression increases. There may be several reasons for this. One is that the distribution of contact compressions is not uniform when the global compression is that large. Studies of the shear stiffness of a single asperity at large compressions were not carried out, and the assumptions made when developing the theory may not be valid. In addition, the shape of a single asperity is actually not a semi-circle. The geometry might be important. It may also be that the assumption of roughness at a single length scale is not very good, and that a distribution of contact sizes l should be included when estimating Q.

Further studies should be carried out to test this scaling behavior for different Hurst exponents. It may be that the shape of the asperities is important, and that we were lucky with the choice of $H = 0.5$. The effects of long range elastic interactions should also be further tested. A third aspect is the dimensionality of this problem. In three dimensions, the estimation of Q_i made in section 7.1 is no longer valid, and has a different functional form. Using the shape of a single asperity, the same arguments can easily be followed. An analytical prediction might be difficult to find, but numerical integration can be carried out.

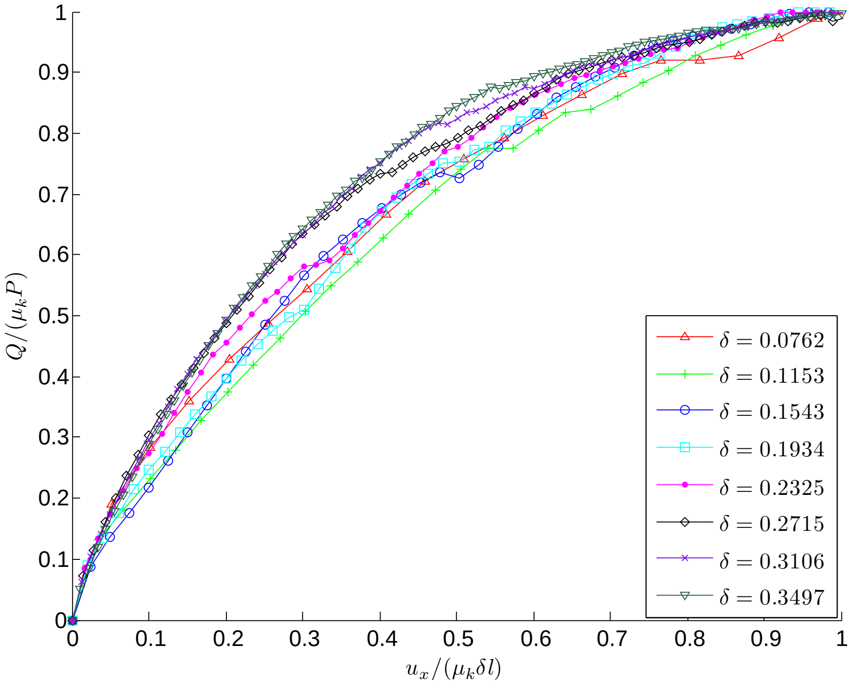

Figure 7.13: *Linear scaling attempt of the shear stiffness with the applied pressure* P *and the dynamic friction coefficient* μ_k*.*

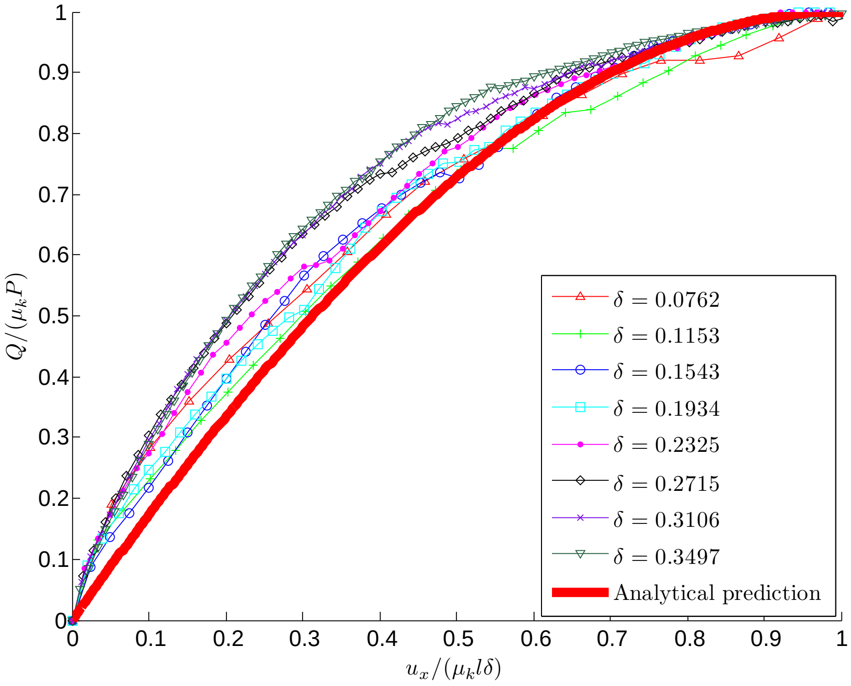

Figure 7.14: *Linear scaling attempt of the shear stiffness with the applied pressure* P *and the dynamic friction coefficient* μ_k*. The predictions are made for a uniform compression distribution and for* $\beta = 1.30$*.*

Measuring the compression distribution

In order to test the theory further, we measure the compression distribution of micro-contacts. This proves to be difficult because we cannot interpret neighbor nodes as individual asperities. The solution is a detour measuring the contact area. Figure (7.15) shows the algorithm sketch. We take the surface plotted in figure (7.7) and overlap it with a plane. The result is a distribution of contact zones. The area of these contact zones are measured. In chapter 6 we found that the surface area was related to the indentation as

$$a \sim \delta^{\beta/2}. \tag{7.20}$$

Using the geometrical relation from Roux-Schmittbuhl theory [34] leads to $\beta = 1$. When the distribution of contact areas is found, the equivalent distribution of compressions is calculated using this relation. In addition we note that the maximum local compression is given by the global compression parameter δ. We divide by the maximum compression to scale the compression axis to 1. Figure (7.16) shows the compression distribution for three different indentations. The distribution is changed as the indentation increases.

Figure (7.17) demonstrates that the underlying compression distribution found from the surface profile is very important to shape of the tangential loading curve. The variation in the distributions is not very large, still the curvature is quite different. The theory does not give a perfect fit, but it gives useful insight to which parameters are important to the shear stiffness of a surface layer. These results predict that the compression distribution, and hence also the surface profile, is important. It is worth noting that the shear stiffness can be predicted from the behavior of one contact and the surface profile, both found without applying a tangential load. In addition the friction coefficient is needed.

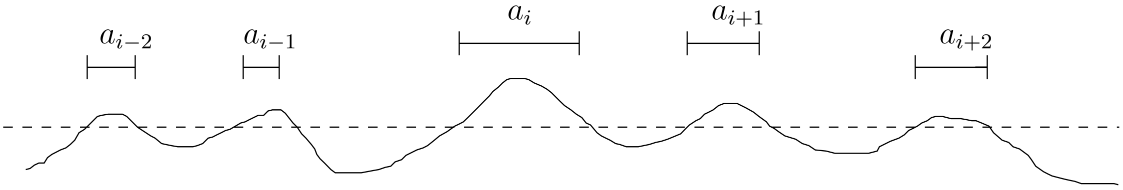

Figure 7.15: *Local contact area measurements are used to estimate the compression distribution with the power law relation between the compression and the contact area.*

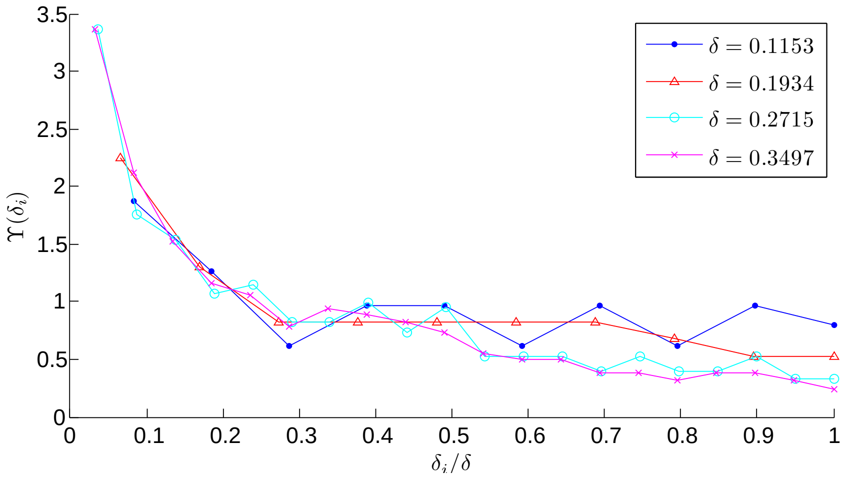

Figure 7.16: *The micro-contact compression distribution for three different indentations of a plane on a self-affine surface.*

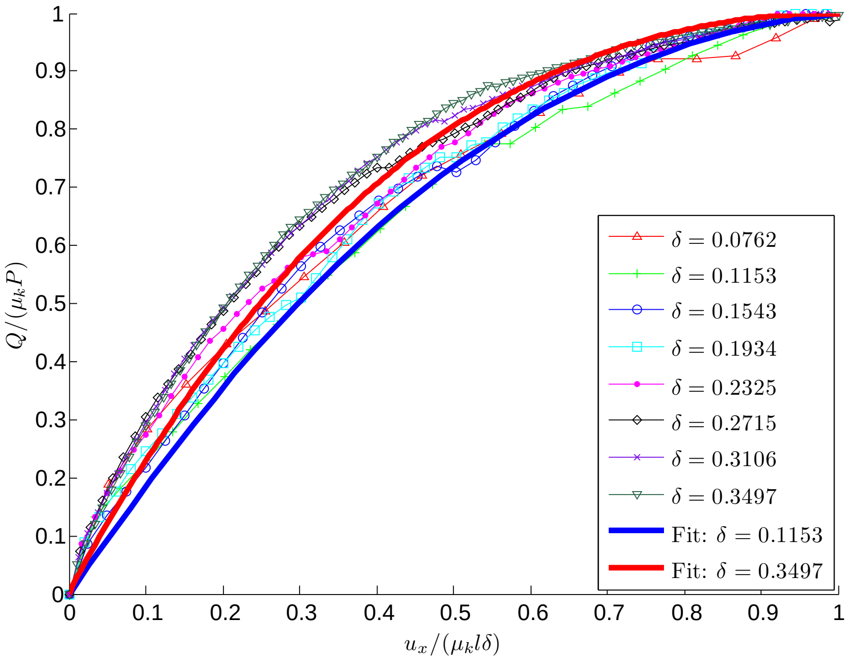

Figure 7.17: *The tangential loading curve of a self-affine surface fitted with theory from the measured compression distribution.*

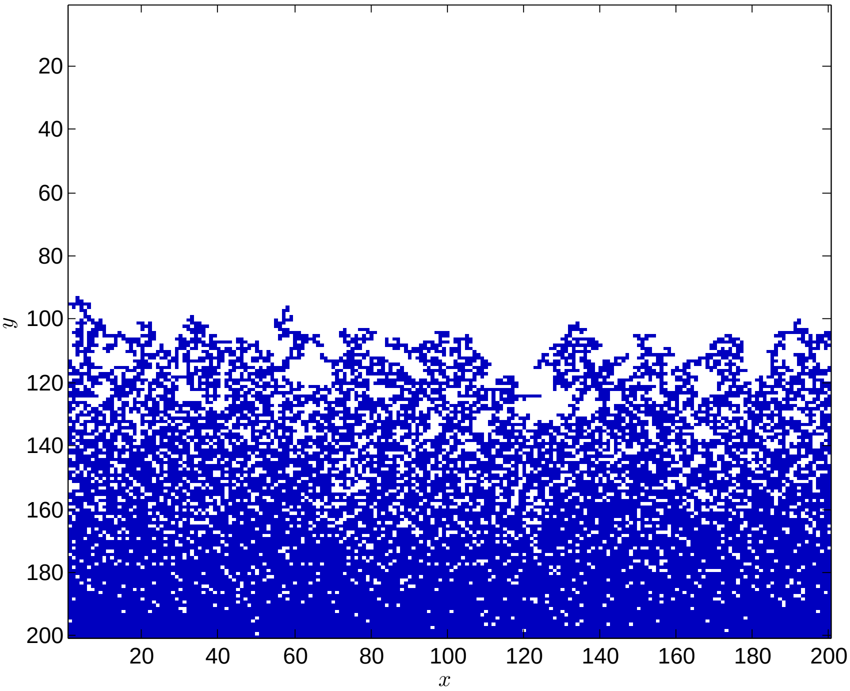

Figure 7.18: *Example of a spanning cluster generated by linear gradient percolation.*

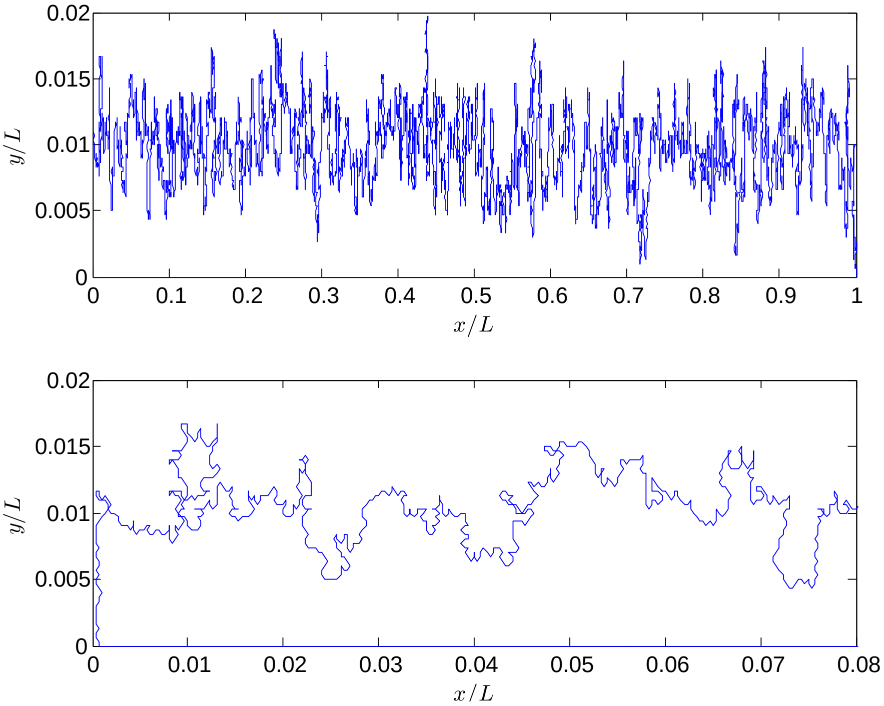

Figure 7.19: *Surface generated by linear gradient percolation. The full surface is plotted in the top figure, while a small part of the surface is plotted in the bottom figure.*

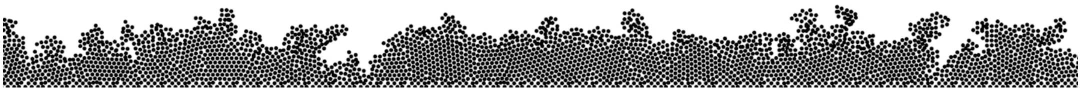

Figure 7.20: *Final surface created by linear gradient percolation and the random drop method with* $\zeta = 1/3$.

7.3 Gradient percolation

We now investigate a second surface type; the fractal surface. This surface includes overhangs and is not easily defined by the Hurst exponent, even though attempts have been made [46]. These surfaces are typically generated through surface growth processes or corrosion. Our model can treat complex overhanging surfaces. The method used to create these surfaces is the gradient percolation method.

We introduce a matrix $M_\Upsilon(x, y)$ of probabilities $\Upsilon(y)$, where

$$\Upsilon(y) = \frac{y_{max} - y}{y_{max}}. \tag{7.21}$$

The position (x, y) is occupied with a probability given by M_Υ, which is added to a occupation matrix $O_\Upsilon(x, y)$. O_Υ now contains multiple clusters, and we need to remove the ones that are not part of the spanning cluster (the cluster spanning the x-direction). Since we use gradient percolation, the bottom layer is always part of the spanning cluster. By iterating from the bottom, and labeling all the sites in contact, the cluster is found. Figure (7.18) shows a spanning cluster generated by gradient percolation. It contains holes and defects that are removed when the final surface is generated.

We further introduce a magnification factor ζ. The lattice points in the gradient percolation matrix used for initializations has nodes with radius r_Υ. Nodes with radius $r \leq r_\Upsilon$ are placed on the percolation matrix, giving the magnification

$$\zeta = \frac{r_\Upsilon}{r}. \tag{7.22}$$

$\zeta = 1$ is the maximum possible magnification. When initializing the surface with the random drop method, nodes with only two neighbors may appear. This is a problem since these nodes will have zero stiffness. The problem is solved by adding a second layer of nodes as an additional surface layer. Note that this may slightly change the fractal dimension D.

7.3.1 Measuring the fractal dimension

A surface generated by gradient percolation is defined by the fractal dimension, which is well described in the percolation theory [56]. The fractal dimension of a surface can be measured using the box counting algorithm. The surface structure is covered by boxes of size $(r_b \times r_b)$. If N_b is the number of boxes needed to cover the structure and L is the surface length, we have that

$$N_b(r_b) = B_1 \left(\frac{r_b}{L}\right)^{-D} + B_2 \left(\frac{r_b}{L}\right)^{-1}, \tag{7.23}$$

where B_1 and B_2 are constants, and D is the fractal dimension of the surface. D can be measured using a linear fit with logarithmic axes.

7.3.2 Numerical results

The boundary conditions are equal to those of the self-affine surface. Figure (7.19) shows the realization of the surface, while figure (7.20) shows a part of the surface initialized

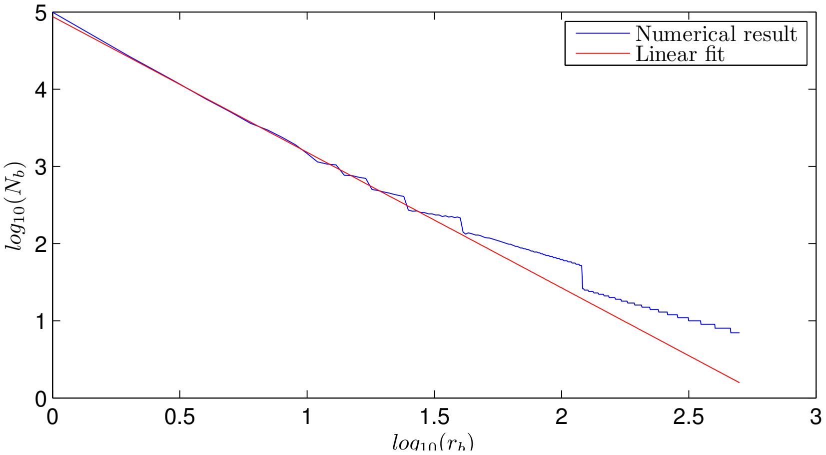

Figure 7.21: *Measuring the fractal dimension of the gradient percolation surface. It was estimated through a linear fit to be* $D \approx 1.75$.

with the random drop method and $\zeta = 1/3$. The fractal dimension is measured to be $D \approx 1.75$ using the box counting algorithm. The measure is shown in figure (7.21). Note that the fractal dimension is difficult to measure with high precision.

Frictional indentation

The surface is compressed under a friction law with $\mu_s = \mu_k = 0.5$. The contact area as a function of the pressure is plotted in figure (7.22). For the gradient percolation surface the contact area is no longer linear in the pressure, but has a power law behavior with an exponent estimated to 0.81. This is quite different from the scaling theories of self-affine surfaces where $a \sim P$.

The relation between the pressure and the indentation is also investigated. This is shown in figure (7.23). The scaling behavior of fractal surface is not clear. It is neither an exponential function nor a simple power law. This might be due to discretization effects and should be investigated further for larger systems. When the deformation of the surface layer is large, the initial form of the surface should not be important to the change in pressure. For that reason the behavior for large deformations is similar for the self-affine surface and the gradient percolation surface. However, at high compressions, the elastic interactions between the asperities become increasingly important, as well as the interaction with the bulk layer that is assumed to be infinitely stiff.

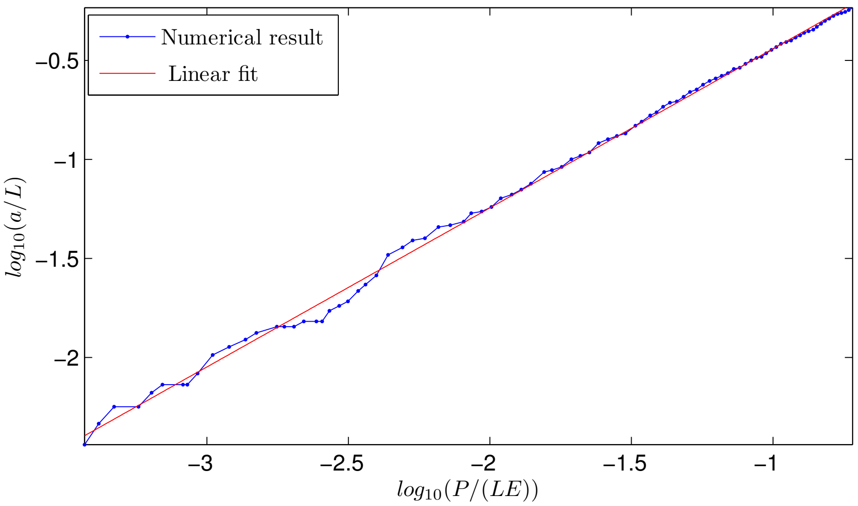

Figure 7.22: *The contact area as a function of the pressure for a gradient percolation surface. The surface area scales as* $P^{0.81}$.

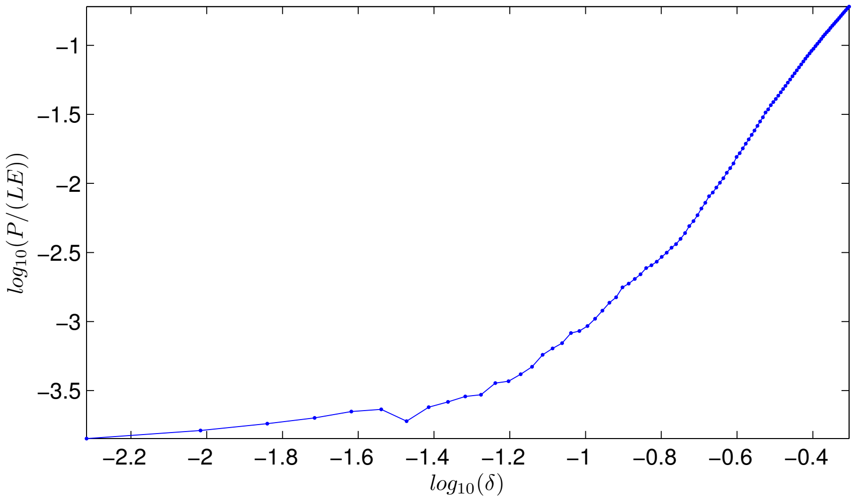

Figure 7.23: *The change in total normal load of the system as a function of the compression.*

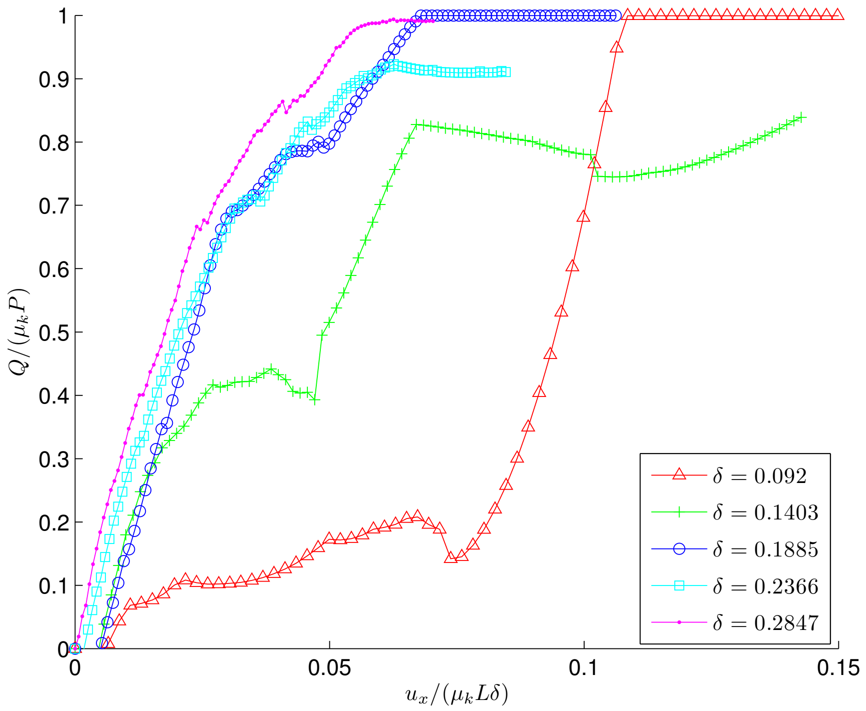

Figure 7.24: *Q as a function of the displacement for different values of the compression. The curves are scaled with the compression and the total normal load.*

Shear

The total tangential load Q as a function of the displacement u_x is measured, and the scaling with the compression is plotted in figure (7.24). The behavior of the gradient percolation surface when imposing a shear displacement is not trivial. For small compressions the discretization effects are large because the number of contacts is small. The contacts may bend, and the pressure may change significantly during the shearing. This effect may average out when the number of micro-asperities in contact with the potential surface is large.

A problem that arises is the scaling with the asperity size l. For the self-affine surface this distance is well defined. In this case it is not, and the displacement axis does not scale to 1. Due to the friction indentation and the overall complexity of the surface, the total tangential load is even slightly negative in the beginning of the process. The reason for this is not clear. Asperities bend and overlap during the indentation, and that affects the tangential loading curve. For large compressions the shear stiffness is similar to the self-affine surface, but no attempt to fit this with the theory has been made. Simulations for larger magnifications ζ and larger system sizes N_x should be carried out before any rigorous conclusions can be made.

7.4 Discussion

The theory developed for the shear stiffness of a surface layer, based on the behavior of single asperities modeled as semi-circles, explains the qualitative behaviour of the tangential loading curve for a self-affine surface with a Hurst exponent $H = 0.5$. Simulations for different values of H and for different system sizes L should be carried out in order to test the theory further, and to test the robustness of the results. It may be that the surface generated is closer to the assumptions made than what is normally the case. The asperities are assumed to be semi-circles, and for large H that might not be the case.

Elastic independence between asperities is also assumed. Because the surface and a small bulk consisting of ten blocks is glued to a rigid body, long range elastic interactions are neglected. In addition, asperities modeled as semi-spheres in three dimensions will have a different shear stiffness than the semi-circle in two dimensions. This will change the theory slightly, and it may not be possible to find an analytical solution. Numerical integration should however still be possible. The effects of the long range elastic interactions should also be investigated further.

For the gradient percolation surfaces, further investigations have to be carried out before any conclusions can be made. At this point, the behavior is not understood.

Part IV

DISCUSSION

Chapter 8

Discussions and conclusions

Starting with a one-dimensional mesoscopic friction model, we saw that two-dimensional effects are too important to be neglected in order to reproduce some of the features of recent friction experiments. We also found that predictions for the length and time of the next precursor event in the model can be predicted.

Some of the assumptions in the mesoscopic model are actually results that can be measured in a microscopic model. In order to test the assumptions, the results from the spring block model was used when developing a microscopic two-dimensional spring block model with an equilibrium solver using a quasi-static integrator along the surface. The model produced results in agreement with Hertz theory and Cattaneo-Mindlin theory. A single asperity was modeled as a semi-circle. These results were further used to develop a theory for the shear stiffness of a rough surface constituted by multiple semi-circular asperities.

8.1 Discussions

8.1.1 The mesoscopic model

The one-dimensional mesoscopic model was introduced in order to understand the dynamics of recent friction experiments. The precursor lengths measured in the model were not quantitative agreement with the experiments, and adding a torque parameter made the differences even larger.

Better agreement with experimental observations was achieved by including the two-dimensional Poisson effect in the initial shear force distribution. In addition, the normal force distribution at the bottom of a two-dimensional block is not uniform even if the loading on top is uniform. To account for these effects a two-dimensional model should be introduced. A two-dimensional spring block model with Amontons-Coulomb friction was studied by Jørgen Trømborg [51]. The effects of adding a second dimension also led to a research article on the transistion from static to dynamic friction [53].

What we have learned from the model is a qualitative understanding of the mechanisms that govern the transition from static to dynamic friction. It was shown that the precursor lengths are very sensitive to the initial shear force distribution. A different study by David Skålid Amundsen shows that the shear force distribution is also important in the description of rupture velocities [50].

Predictions for the time and length of the precursor events can be made assuming that the driving spring is soft, and that simple Amontons-Coulomb friction applies. An important question is if this is still possible to make these predictions when the friction law is modified (e.g rate and state friction laws). The introduction of a slip-weakening friction coefficient resulted in a different system behavior, and predictions may be difficult to obtain because the stress peak at the edge of the crack may not be negligible. It also demonstrated that the spring block model is quite sensitive to the details of the friction law.

8.1.2 The microscopic model

In the mesoscopic model, microscopic effects are included through a local friction law that applies between the individual blocks and the surface they slide on. In order to investigate the validity of the local friction law, a two-dimensional microscopic model was introduced. The model was compared with Hertz and Cattaneo-Mindlin theory for a plane on cylinder contact in two dimensions. The contact area as a function of the normal load, and the size of the stick region in the center of the contact as a function of the tangential load were in good agreement with theory. An asymmetry in stick region not predicted by the theory was also observed.

The Cattaneo-Mindlin theory does not consider friction during normal loading. The observed asymmetry of the stick region is too large to be neglected. Frictionless normal loading results in full slip along the whole contact interface (because of the Poisson effect), and the traction distribution vanishes. Accounting for the effects of friction during the normal loading results in an anti-symmetric traction distribution, and micro-slips at the edges of the contact travelling in opposite directions. When the system is further subjected to a tangential displacement, instant slip occurs at the leading edge giving rise to a large asymmetry in the stick region. The tangential loading curve was not largely affected by this asymmetry.

The introduction of static friction

In addition to a dynamic friction coefficient (which is the only friction coefficient in the Cattaneo-Mindlin theory) a static friction coefficient was introduced. Tests were carried out to ensure that the equilibrium scheme converged forward in time. Since there is no time in the integration scheme, the driving can be interpreted as infinitely slow. This might affect the results. If an asperity is modeled as a semi-circle in two dimensions, the pressure at the edges of the contact region is small, and in practice we will always have micro-slips if the driving speed is finite. Even though the stop fronts observed in the microscopic model are also obtained in the mesoscopic one-dimensional model, a time integration scheme should be used in order to validate the introduction of a static friction coefficient in the quasi-static model.

Rough surfaces and the validity of the Boitnott theory

A scaling relation for the tangential loading curve of a single asperity with μ_k, u_x, L and δ was obtained, where μ_k, u_x, l and δ are, respectively, the friction coefficient, the displacement of the surface layer, the asperity size, and the compression. This relation was used to develop a theory for the shear stiffness of a rough surface in two dimensions assuming elastic independence of contacts. The result depends on the characteristic asperity size and the compression distribution of contacts. The compression distribution is obtained from the surface topography using the contact area - compression relation determined for single asperities.

In order to test the theory, the microscopic model was used to simulate plane on rough contacts. The rough contact was a self affine surface defined by the Hurst exponent H. An overall agreement between the numerical result and the analytical prediction for plane on rough contact was obtained, but the detailed behavior was rather different. The validity of the model might change if a rough on rough contact is used. Assuming a rough on plane contact, new contacts do not form during the tangential loading and the theory is exact in the limit of full slip. This is not the case if a rough on rough contact is assumed.

A different aspect that should be considered is the long range elastic interactions between the asperities. This is neglected in the Boitnott theory. These interactions are also neglected in the numerical model by assuming an infinitely stiff bulk. The elastic interactions may be important to the global behavior of the surface layer, and the effects of implementing them should be studied. What the model does give, is a valuable insight into the mechanisms that govern the global behavior of the tangential loading curve of a surface layer. The distribution of asperity heights gives rise to large local variations in the normal load, and the shear stiffness of the surface layer is governed by these local variations. Local contact points on a multi-contact interface will have different friction tresholds, and hence reach full slip at different surface displacements. This results in a weakening of the shear stiffness as the displacement increases. This behavior is consistent with experimental and analytical results of Biegel and Boitnott [40, 58], but detailed comparison with experiments have not been made. It is therefore unclear how well the tangential loading curve obtained with the microscopic model compares to experimental results.

The surface compression as a function of the normal load is far from any theoretical predictions. Schmittbuhl theory predicts a linear relation between the compression and the load, but assumes no elastic deformations. However, since the surface layer, in the microscopic model, is soft, this assumption is not valid. Persson predicts an exponential behaviour which is not observed.

A problem also arises when introducing the magnification ζ. The magnification is a measure of the scale of which the system is sampled. Changing the magnification changes voth the resolution along the contact interface and the real area of contact. The asperity concept is then not well defined since it depends on the magnification. For large magnifications the asperity picture breaks down, and molecular dynamics or quantum mechanics applies. Unfortunately, shear stiffness calculations for different magnifications has not yet been carried out because of shortage of time. It is still unclear how the gap between these different regimes can be bridged, and at which scale the asperity picture breaks down. This should be investigated further.

In modeling the surfaces only two dimensions were used. The third dimension might be important, and is needed in order to compare numerical results directly to experimental observations.

The theory of Boitnott [40] in three dimensions is similar to the two-dimensional theory developed in this theses. This suggests that the slip mechanism governing the behavior of a three-dimensional tangential loading curve is also the governing mechanism in two dimensions. However, the tangential loading curve of a single asperity is different since it depends on the shape of the asperity.

A more complicated surface generated by a gradient percolation algorithm was also introduced. However, the results for the tangential loading curve were rather inconclusive. In case of overhangs, the asperities may bend and elastic contact between different asperities can no longer be neglected. In addition, this type of surface may give rise to large variations in the normal force as a tangential load is applied. The theory developed in chapter 7 for the shear stiffness of a surface layer did not fit very well with the numerical results. One of the reasons may be that the discretization effects are simply too large, and that the global system behavior is too sensitive to local effects. Increasing the system size might average these effects out. Unfortunately, increasing the system size will also increase the computational cost which is already high.

Different studies of shear stiffness

The elastic model with Amontons-Coulomb friction presented in this thesis does not explain phenomena such as junction growth, which suggests that it is governed by physical effects not included in the elastic model. The assumption of a purely elastic medium with an Amontons-Coulomb friction law has its limitations. Many effects that are believed to be important to the frictional behavior of a system are not included. Among them are temperature and plasticity. In addition, effects of interactions at the atomic scale are neglected. Further studies should be carried out to investigate the importance of these effects. However, some valuable insight into the mechanisms that govern the shear stiffness has been gained.

Molecular dynamics simulations were recently carried out by Akarapu et. al [39], and their approach might be better suited for the problem since it involves interactions at the atomic scale. A problem with molecular dynamics is the computational cost, which is high if full time-integration has to be performed. The system sizes that can be investigated with molecular dynamics are much smaller than the ones presented in this thesis.

8.1.3 Coupling of the microscopic and the mesoscopic scale

From what we found in the surface calculations, the shear stiffness of the surface layer is not modeled sufficiently in the mesoscopic model. An important question to ask is how to introduce the effects of the shear stiffness in a mesoscopic model.

The tangential loading curve of the surface layer determines the behavior of a local block in the mesoscopic model. This can be modeled through the local friction law. One way to do this is to introduce a Braun [31] type of model where the friction force is modeled as springs breaking and reforming. This way of implementing the local friction law is close to what we found in the microscopic model. A surface consisting of asperities with different friction thresholds behave in a similar way. Slow fronts were also observed in the Braun model, and it might be that it is an effect of the tangential loading curve of the surface layer. This should be investigated further.

Other changes in the local friction law migth also account for these microscopic effects. Effects included in molecular dynamics simulations (e.g atomic interactions) may be too important to be neglected. This should also be investigated further.

8.2 Conclusions

The one-dimensional spring block model is not sufficient to reproduce details of recent experimental results. It does, however, give some qualitative understanding of some of the governing mechanisms. The shear and normal force distributions are important, and they are also sensitive to the choice of boundary conditions. Predictions of the precursor length and the time of the next event can be made accurately assuming Amontons-Coulomb friction and a soft driving spring. A more complicated model including a second dimension and a different local friction law is needed to gain more detailed knowledge about the mechanisms at play.

The tangential loading curve of a single asperity in two dimensions was found to have a simple scaling behavior with δ and μ_k. The tangential loading curve is governed by micro-asperities reaching full slip at different displacements u_x because they have different friction thresholds. The friction treshold is an effect of the distribution of asperity heights that give local variations in the stress field. The Boitnott theory shows the same qualitative behavior, but the details of the theory are different from the numerical results.

8.3 Choice of numerical model

In this thesis, a two-dimensional discrete element method (DEM) was developed. This model was used mainly for historical reasons. The one-dimensional model was inspired by the work of Maegawa et al. [15], of which the two-dimensional quasi-static model is a natural extension. In appendix C, a finite element method (FEM) was used to verify the results from the DEM solver. At this point I believe that the FEM solver is better at solving the types of problems discussed in this thesis. It is much faster (a typical cylinder on plane simulation takes a few minutes, versus an hour with DEM (depending on the resolution of nodes), and there is no need to do an ensemble average to get rid of discretization effects. This could also have been solved with a varying block size in DEM. The numerical cost in the DEM solver can be decreased by introducing e.g a Hessian matrix approach, or a region relaxing algorithm. A commercial FEM solver is easy to use, and has a good graphical interface. This is lost when writing your own code. However, what is gained is a better insight to the integration algorithm. Using a commercial package one will often not gain the same insight.

The initialization of rough surfaces is easily implemented in the spring block system. It may be that this is an advantage of the DEM solver.

8.4 What could have been done differently if starting from scratch again?

Introducing a spring block model with the friction modeled as springs detaching and reattaching may be closer to the asperity picture than the simple Amontons-Coulomb friction. If starting from scratch, I would probably have introduced this type of model. In addition, I would have modeled the system in two dimensions.

In the microscopic two-dimensional model I would have spent less time on the Cattaneo-Mindlin discussion and more on the rough surfaces. I would not have spent time implementing the conjugate gradient method because it turns out it is difficult to implement it with a friction law. Instead, I should have tried to decrease the computational cost of the successive over-relaxation algorithm. The time spent on the one-dimensional model also limited the time I could spend studying rough surfaces. Effects that could be implemented are long range elastic interactions and different magnifications. I also used much time developing a theory for the shear stiffness of a rough surface, only to later discover that it already been done in three dimensions. This could have been avoided with better research up front.

8.5 Future studies

Throughout this thesis I have barely scratched the surface of friction studies. Even though this is only a small fraction of possible friction studies, many questions are yet to be answered. Some of these questions can be the base for future studies. In the one-dimensional mesoscopic model some of the possible future projects are:

- How can effects of the different friction laws be quantified?
- Can the strength (energy output) of the next event be predicted?
- Can predictions be made for a more complex system with a decent accuracy?

In two-dimensional model there are also questions yet to be answered. The Cattaneo-Mindlin theory for two different friction coefficients is one of them:

- Can further investigations of μ_s in the Cattaneo-Mindlin theory be made by moving away from the stick slip assumption with an equilibrium integration scheme?

On the studies of rough surfaces, much work still remains. The parameter space is yet to be studied extensively, and the effects of different roughnesses and magnifications are not known. Questions that may be answered in future studies are:

- What are the effects of the long range elastic interactions?
- How will the tangential loading curve be altered if the contact is rough on rough?
- What is the effect of changing the Hurst exponent/fractal dimension?

- Can a complicated rough surface easily be implemented in commercial FEM solvers?
- What is the effect of the surface shear strength if implemented in a deterministic spring block model?
- How can the gap between the microscopic and macroscopic scale be bridged?

Part V

APPENDICES

Appendix A

Parameter space in the 1D spring block model

Simulations to test the scaling behavior with N and μ_s in the side driven model were carried out. Figure (A.1) shows how the number of precursors in the model depends on N. The scaling is far from good. Figure (A.2) shows the dependence on μ_s. The number of precursors decreases as μ_s increases.

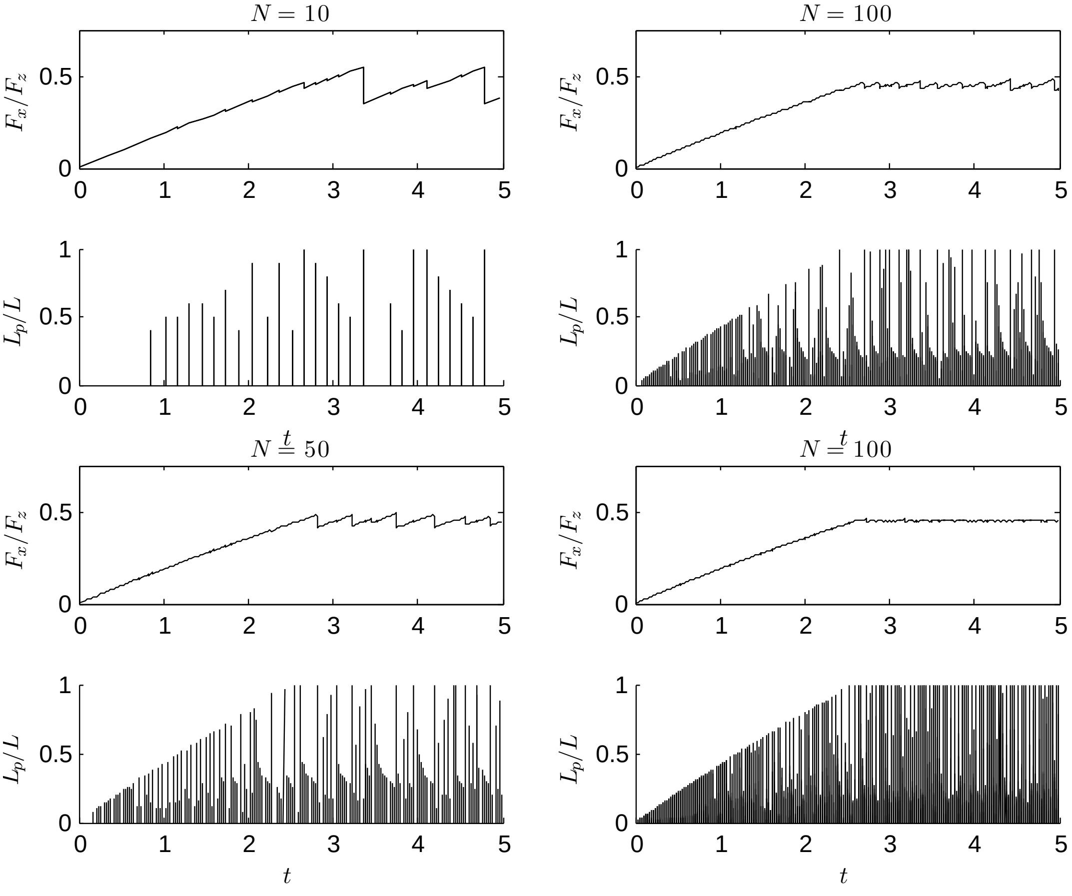

Figure A.1: *Side driven spring block model with parameters from table (3.1) for different N.*

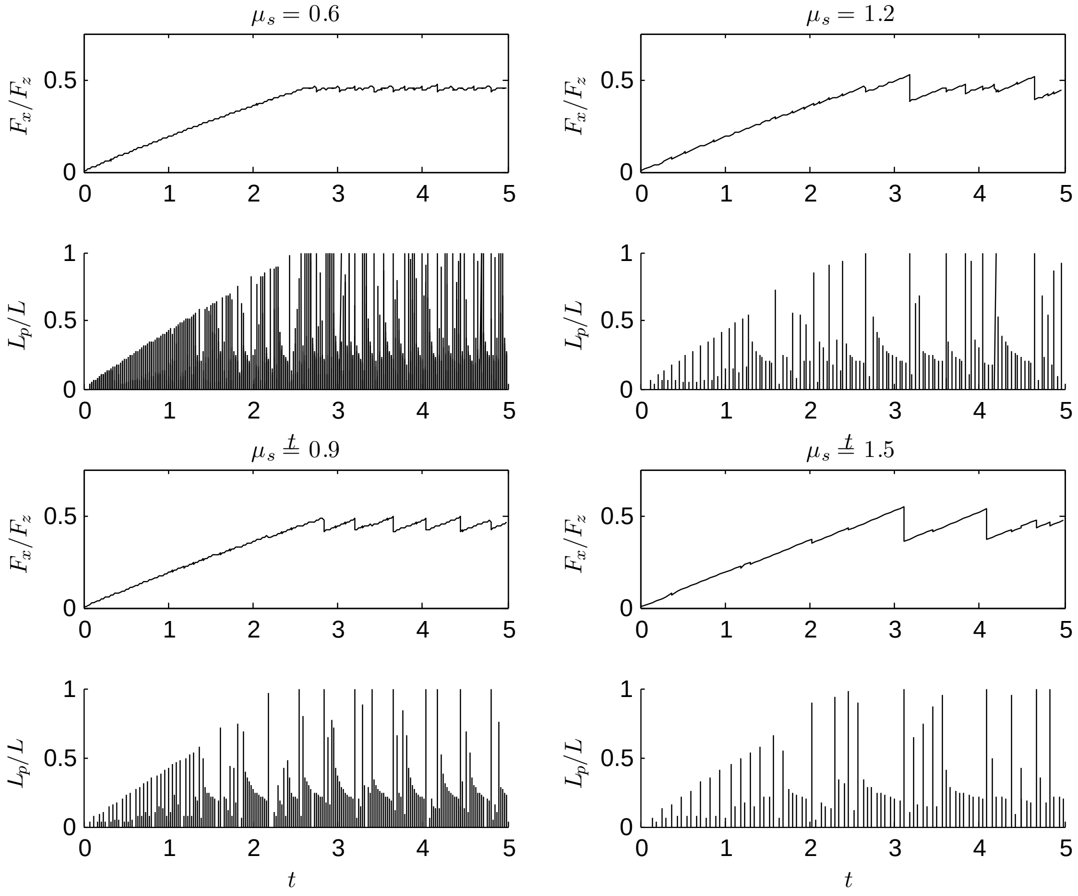

Figure A.2: *Side driven spring block model with parameters from table (3.1) for different* μ_s.

Appendix B

Software used in the thesis

Most of the coding was done in C++, while Matlab was used for visualization. Some visualization was done using VMD [67]. The finite element implementations was made using Abaqus. The random generator and the conjugate gradient method were taken from Numerical Recipes [49].

Appendix C

Plane cylinder contact in FEM

To verify results of the developed discrete element method, the semi-circle in contact with a plane surface was studied using a commercial finite element solver. This was done in order to verify the results from the discrete element method. A semi-circle is compressed by $\delta = 0.1$ using a plane with a Youngs modulus 1000 times higher than the semi-circle. Frictionless boundary conditions are used at the contact interface during the normal loading. The bottom layers of the plane and the semi-circle are glued to a rigid body. A friction law with a single friction coefficient $\mu_k = 0.5$ is then applied, and the system is subjected to a shear force imposed by moving the plane.

Solution technique

Abaqus solves the elastic equations (chapter 4) on each element finding the global equilibrium state. The solution technique used was Newton's method for nonlinear elastic problems with an instantaneous load variation during the steps. The mesh used is shown in figure (C.1). Along the contact surface square elements with a fine resolution are used, while low resolution triangular elements are used elsewhere. The fine resolution at the contact interface is required for precise measurements of the stick region in order to compare results with both analytical Cattaneo-Mindlin results, and to the developed discrete element method. Figure (C.2) shows an example output of the total pressure distribution in the two materials. Abaqus has multiple output options, and we will have a look at the contact stiffness, the size of the stick region, and the asymmetry produced in the stick region. The results in the discrete element method were discussed in chapter 6.

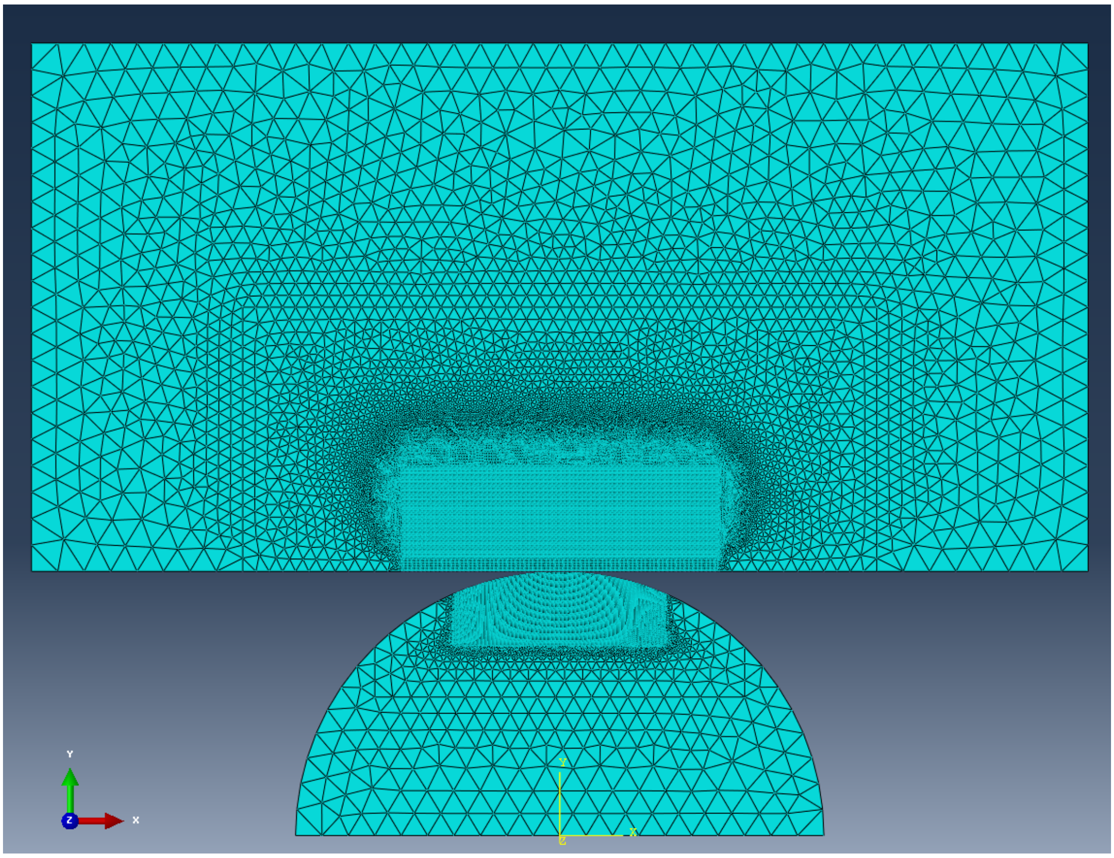

Figure C.1: *Mesh setup in the FEM model.*

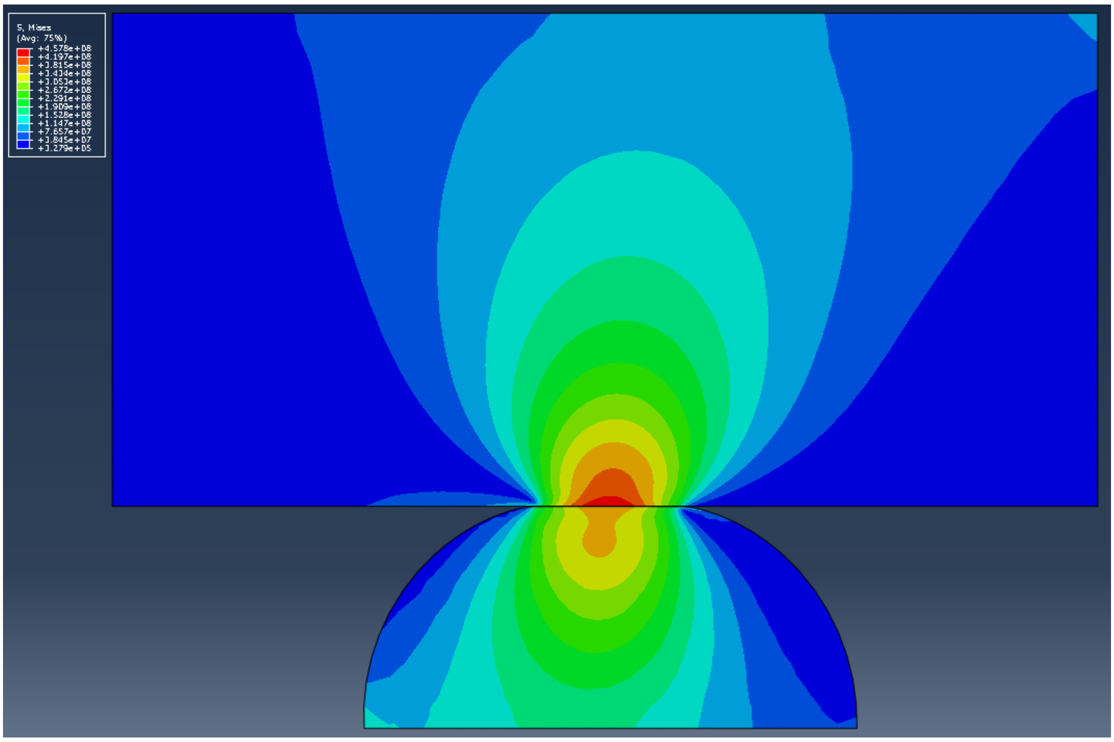

Figure C.2: *Pressure distribution in the FEM model*

Shear stiffness

The first thing we wish to verify is the imposed displacement. In order to do this we use the stiffness of a cylinder compressed by $\delta = 0.1$, and then impose a displacement u_x/L.

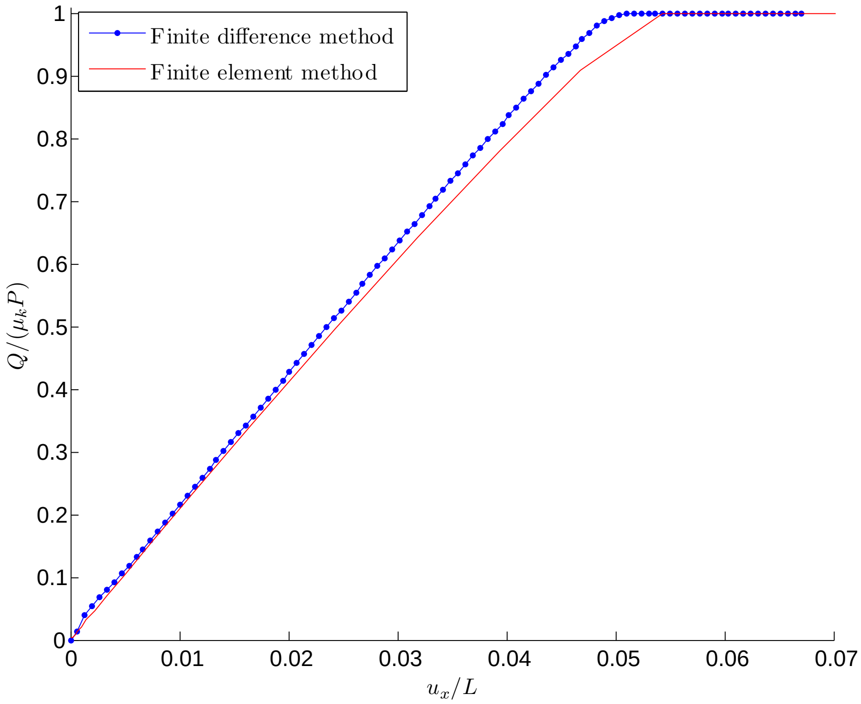

Figure C.3: *The tangential loading of a semi-circle compressed by* $\delta = 0.1$ *with a single friction coefficient* $\mu_k = \mu_s = 0.5$. *The dotted line is the discrete element result, while the simple line is the Abaqus result.*

Stick region

The size of the stick region can also be measured. Figure(C.4) shows the obtained size and the prediction by Cattaneo-Mindlin theory. Figure(C.5) shows the produced asymmetry in the stick region. Results are consistent with the discrete element method with equal friction coefficients, but the discretization effects are larger in the discrete element method.

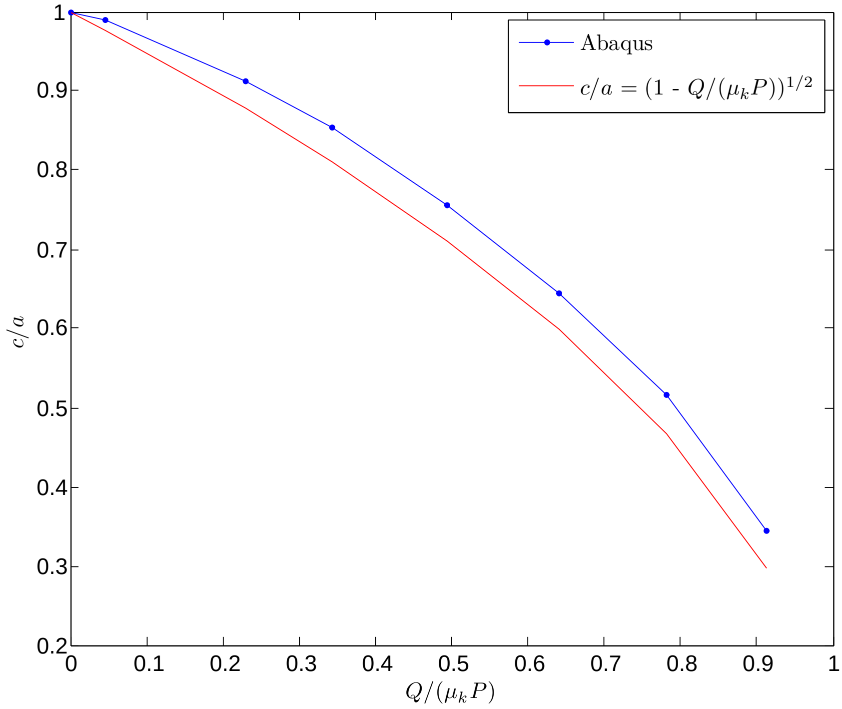

Figure C.4: *The size of the stick regions of a semi-circle compressed by* 10% *with a single friction coefficient* $\mu_k = \mu_s = 0.5$*. The dotted line is the Abaqus result, while the simple line is the analytical prediction by Cattaneo-Mindlin theory.*

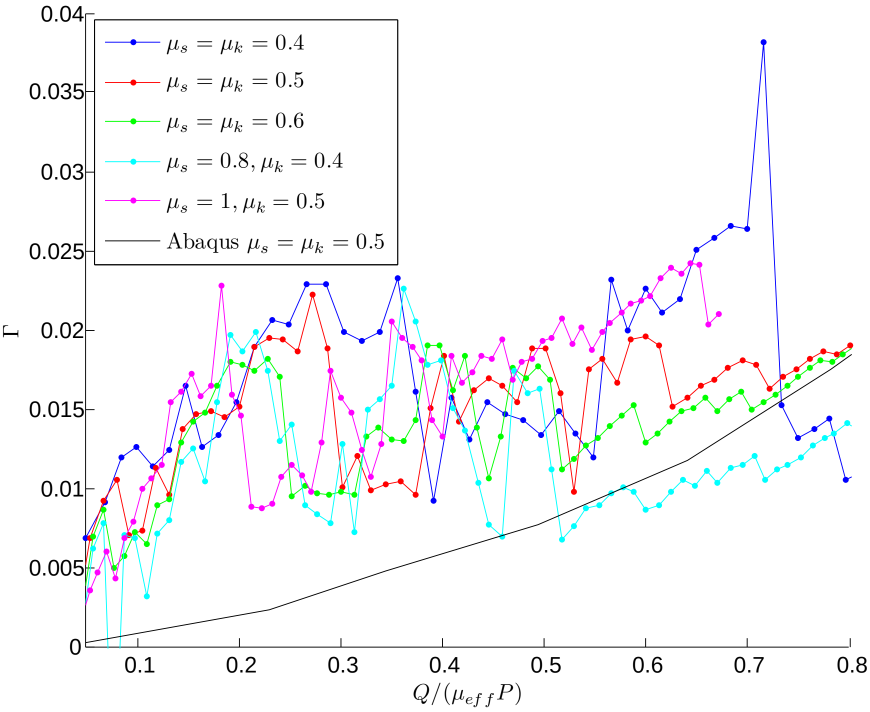

Figure C.5: *The asymmetry in the stick zone. Cattaneo-Mindlin theory does not predict this result.*

Bibliography

[1] B. N. J. Persson, *Sliding Friction.* Berlin: Springer, 1998.

[2] W. F. Brace and J. D. Byerlee, "Stick-slip as a mechanism for earthquakes," *Science*, vol. 153, no. 3739, pp. pp. 990–992, 1966.

[3] D. Dowson, *History of Tribology.* Professional Enginering Publishing Limited, 2nd ed., 1998.

[4] K. Johnson, *Contact Mechanics.* Cambridge: Cambridge University Press, 1985.

[5] T. Baumberger and C. Caroli, "Solid friction from stick–slip down to pinning and aging," *Advances in Physics*, vol. 55, no. 3, pp. 279–348, 2006.

[6] F. P. Bowden and D. Tabor, *The Friction and Lubrication of Solids.* Oxford: Clarendon Press, 1950. Published in the Oxford Classic Series 2001.

[7] J. A. Greenwood and J. B. P. Williamson, "Contact of nominally flat surfaces," *Proceedings of the Royal Society of London. Series A, Mathematical and Physical Sciences*, vol. 295, no. 1442, pp. pp. 300–319, 1966.

[8] C. H. Scholz, *The Mechanics of Earthquakes and Faulting.* Cambridge University Press, 2nd ed., 2002.

[9] P. Berthoud, T. Baumberger, C. G'Sell, and J.-M. Hiver, "Physical analysis of the state- and rate-dependent friction law: Static friction," *Physical Review B*, vol. 59, pp. 14313–14327, Jun 1999.

[10] T. Baumberger, P. Berthoud, and C. Caroli, "Physical analysis of the state- and rate-dependent friction law. II. dynamic friction," *Physical Review Letters B*, vol. 60, pp. 3928–3939, Aug 1999.

[11] C. Marone, "Laboratory-derived friction laws and their application to seismic faulting," *Annual Review of Earth and Planetary Sciences*, vol. 26, pp. 643–696, 1998.

[12] M. Urbakh and E. Meyer, "The renaissance of friction," *Nature Materials*, vol. 9, 2010.

[13] R. Graves, T. Jordan, S. Callaghan, E. Deelman, E. Field, G. Juve, C. Kesselman, P. Maechling, G. Mehta, K. Milner, D. Okaya, P. Small, and K. Vahi, "Cybershake: A physics-based seismic hazard model for southern california," *Pure and Applied Geophysics*, vol. 168, pp. 367–381, 2011. 10.1007/s00024-010-0161-6.

[14] R. Buzio, C. Boragno, F. Biscarini, F. B. D. Mongeot, and U. Valbusa, "The contact mechanics of fractal surfaces," *Nature Materials*, vol. 2, no. 4, pp. 233–236, 2003.

[15] S. Maegawa, A. Suzuki, and K. Nakano, "Precursors of global slip in a longitudinal line contact under non-uniform normal loading," *Tribology Letters*, vol. 38, no. 3, 2010.

[16] S. M. Rubinstein, G. Cohen, and J. Fineberg, "Detachment fronts and the onset of dynamic friction," *Nature*, vol. 430, pp. 1005–1009, Aug 2004.

[17] S. M. Rubinstein, M. Shay, G. Cohen, and J. Fineberg, "Crack-like processes governing the onset of frictional slip," *International Journal of Fracture*, vol. 140, pp. 201–212, 2006. 10.1007/s10704-006-0049-8.

[18] S. M. Rubinstein, G. Cohen, and J. Fineberg, "Dynamics of precursors to frictional sliding," *Physical Review Letters*, vol. 98, p. 226103, Jun 2007.

[19] O. Ben-David, S. M. Rubinstein, and J. Fineberg, "Slip-stick and the evolution of frictional strength," *Nature*, vol. 463, pp. 76–79, Jan 2010.

[20] O. Ben-David, G. Cohen, and J. Fineberg, "Short-time dynamics of frictional strength in dry friction," *Tribology Letters*, vol. 39, pp. 235–245, 2010. 10.1007/s11249-010-9601-9.

[21] O. Ben-David, G. Cohen, and J. Fineberg, "The Dynamics of the Onset of Frictional Slip," *Science*, vol. 330, no. 6001, pp. 211–214, 2010.

[22] O. Ben-David and J. Fineberg, "The dependence of the dry friction threshold on rupture dynamics," *arXiv:1104.5479v1*, 2011.

[23] T. Baumberger, C. Caroli, and O. Ronsin, "Self-healing slip pulses along a gel/glass interface," *Physical Review Letters*, vol. 88, p. 075509, Feb 2002.

[24] R. Bennewitz, J. David, C.-F. de Lannoy, B. Drevniok, P. Hubbard-Davis, T. Miura, and O. Trichtchenko, "Dynamic strain measurements in a sliding microstructured contact," *Journal of Physics: Condensed Matter*, vol. 20, no. 1, p. 015004, 2008.

[25] O. M. Braun and M. Peyrard, "Modeling friction on a mesoscale: Master equation for the earthquakelike model," *Physical Review Letters*, vol. 100, p. 125501, Mar 2008.

[26] O. M. Braun and M. Peyrard, "Master equation approach to friction at the mesoscale," *Physical Review E*, vol. 82, SEP 28 2010.

[27] O. M. Braun and M. Peyrard, "Dependence of kinetic friction on velocity: Master equation approach," *Physical Review E*, vol. 83, APR 28 2011.

[28] J. Scheibert and D. K. Dysthe, "Role of friction-induced torque in stick-slip motion," *EPL (Europhysics Letters)*, vol. 92, no. 5, p. 54001, 2010.

[29] R. Burridge and L. Knopoff, "Model and theoretical seismicity," *Bulletin of the Seismological Society of America*, vol. 57, no. 3, pp. 341–371, 1967.

[30] J. M. Carlson, J. S. Langer, B. E. Shaw, and C. Tang, “Intrinsic properties of a Burridge–Knopoff model of an earthquake fault,” *Phys. Rev. A*, vol. 44, pp. 884–897, July 1991.

[31] O. M. Braun, I. Barel, and M. Urbakh, “Dynamics of trantision from static to kinetic friction,” *Physical Review Letters*, vol. 103, no. 19, 2009.

[32] E. Bouchbinder, E. A. Brener, I. Barel, and M. Urbakh, “Cracklike dynamics at the onset of frictional sliding,” *arXiv:1103.3942v1*, 2011.

[33] J. A. Greenwood and J. B. P. Williamson, “Contact of nominally flat surfaces,” *Proceedings of the Royal Society of London. Series A. Mathematical and Physical Sciences*, vol. 295, no. 1442, pp. 300–319, 1966.

[34] S. Roux, J. Schmittbuhl, J.-P. Vilotte, and A. Hansen, “Some physical properties of self-affine rough surfaces,” *EPL (Europhysics Letters)*, vol. 23, no. 4, p. 277, 1993.

[35] B. N. J. Persson, O. Albohr, U. Tartaglino, A. I. Volokitin, and E. Tosatti, “On the nature of surface roughness with application to contact mechanics, sealing, rubber friction and adhesion,” *Journal of Physics: Condensed Matter*, vol. 17, no. 1, p. R1, 2005.

[36] B. N. J. Persson, “Relation between interfacial separation and load: A general theory of contact mechanics,” *Physical Review Letters*, vol. 99, p. 125502, Sep 2007.

[37] A. Almqvist, C. Campana, N. Prodanov, and B. Persson, “Interfacial separation between elastic solids with randomly rough surfaces: comparison between theory and numerical techniques,” *arXiv:1102.5412v1*, 2011.

[38] C. Campañá, M. H. Müser, and M. O. Robbins, “Elastic contact between self-affine surfaces: comparison of numerical stress and contact correlation functions with analytic predictions,” *Journal of Physics: Condensed Matter*, vol. 20, no. 35, p. 354013, 2008.

[39] S. Akarapu, T. Sharp, and M. O. Robbins, “Stiffness of contacts between rough surfaces,” *Physical Review Letters*, vol. 106, p. 204301, May 2011.

[40] G. N. Boitnott, R. L. Biegel, C. H. Scholz, N. Yoshioka, and W. Wang, “Micromechanics of rock friction 2: Quantitative modeling of initial friction with contact theory,” *J. Geophys. Res.*, vol. 97, no. B6, pp. 8965–8978, 1992.

[41] G. G. Batrouni, A. Hansen, and J. Schmittbuhl, “Elastic response of rough surfaces in partial contact,” *EPL (Europhysics Letters)*, vol. 60, no. 5, p. 724, 2002.

[42] S. Santucci, K. J. Måløy, A. Delaplace, J. Mathiesen, A. Hansen, J. O. Haavig Bakke, J. Schmittbuhl, L. Vanel, and P. Ray, “Statistics of fracture surfaces,” *Physical Review E*, vol. 75, p. 016104, Jan 2007.

[43] S. Santucci, M. Grob, R. Toussaint, J. Schmittbuhl, A. Hansen, and K. J. Maløy, “Fracture roughness scaling: A case study on planar cracks,” *EPL (Europhysics Letters)*, vol. 92, no. 4, p. 44001, 2010.

[44] J. Schmittbuhl, A. Hansen, and G. G. Batrouni, “Roughness of interfacial crack fronts: Stress-weighted percolation in the damage zone,” *Physical Review Letters*, vol. 90, p. 045505, Jan 2003.

[45] R. Buzio, K. Malyska, Z. Rymuza, C. Boragno, F. Biscarini, F. D. Mongeot, and U.Valbusa, “Experimental investigation of the contact mechanics of rough fractal surfaces,” *NanoBioscience, IEEE Transactions on*, vol. 3, no. 1, pp. 27 –31, 2004.

[46] A. Hansen, G. G. Batrouni, T. Ramstad, and J. Schmittbuhl, “Self-affinity in the gradient percolation problem,” *Physical Review E*, vol. 75, p. 030102, Mar 2007.

[47] L. Knopoff and X. X. Ni, “Numerical Instability at the Edge of a Dynamic Fracture,” *Geophysical Journal International*, vol. 147, no. 3, pp. 1–6, 2001.

[48] J. M. Carlson, “Two-dimensional model of a fault,” *Physical Review A*, vol. 44, pp. 6226–6232, Nov 1991.

[49] W. H. Press, S. A. Teukolsky, W. T. Vetterling, and B. P. Flannery, *Numerical Recipes.* Cambridge University Press, third ed., 2007.

[50] D. S. Amundsen, “Modelling the onset of dynamic friction: A study of rupture velocities,” Master’s thesis, University of Oslo, Oslo, 2011.

[51] J. Trømborg, “Modelling the onset of dynamic friction: Importance of the vertical dimension,” Master’s thesis, University of Oslo, Oslo, 2011.

[52] O. Ben-David, S. M. Rubinstein, and J. Fineberg, “Slip-stick and the evolution of frictional strength,” *Nature*, vol. 463, pp. 76–79, Jan 2010.

[53] J. Trømborg, J. Scheibert, D. S. Amundsen, K. Thøgersen, and A. Malthe-Sørenssen, “Transition from static to kinetic friction: insights from a 2D model,” *arXiv/1105.3325*, 2011.

[54] S. Timoshenko and J. N. Goodier, *Theory of Elasticity - 3rd ed.* Stanford: McGraw-Hill international editions, 1970.

[55] D. Nowell, D. Hills, and A. Sackfield, “Contact of dissimilar elastic cylinders under normal and tangential loading,” *Journal of the Mechanics and Physics of Solids*, vol. 36, no. 1, pp. 59 – 75, 1988.

[56] A. A. J. Feder, *Fractals in Physics.* Amsterdam: North-Holland, 1990.

[57] C. Yang and B. N. J. Persson, “Contact mechanics: contact area and interfacial separation from small contact to full contact,” *Journal of Physics: Condensed Matter*, vol. 20, no. 21, p. 215214, 2008.

[58] R. L. Biegel, W. Wang, C. H. Scholz, G. N. Boitnott, and N. Yoshioka, “Micromechanics of rock friction 1. effects of surface roughness on initial friction and slip hardening in westerly granite,” *J. Geophys. Res.*, vol. 97, no. B6, pp. 8951–8964, 1992.

[59] L. Monette and M. P. Anderson, “Elastic and fracture properties of the two-dimensional triangular and square lattices,” *Modelling and Simulation in Materials Science and Engineering*, vol. 2, no. 1, p. 53, 1994.

[60] C. Kittel, *Introduction to Solid State Physics - 8th ed.* Berkeley: John Wiley and Sons, Inc, 2005.

[61] D. Allen, *Relaxation Methods.* Toronto: McGraw-Hill, 1954.

[62] E. L. Hinrichsen, J. Feder, and T. Jøssang, "Geometry of random sequential adsorption," *Journal of Statistical Physics*, vol. 44, pp. 793–827, 1986. 10.1007/BF01011908.

[63] I. Etsion, "Revisiting the cattaneo-mindlin concept of interfacial slip in tangentially loaded compliant bodies," *ASME Conference Proceedings*, vol. 2009, no. 48951, pp. 297–299, 2009.

[64] J.-F. Lin, T.-H. Fang, C.-D. Wu, and K.-H. Houng, "Contact and frictional behavior of rough surfaces using molecular dynamics combined with fractal theory," *Computational Materials Science*, vol. 40, no. 4, pp. 480 – 484, 2007.

[65] R. F. Voss, "Characterization and measurement of random fractals," *Physica Scripta*, vol. 1986, no. T13, p. 27, 1986.

[66] P. Meakin, *Fractals, scaling and growth far from equilibrium.* Cambridge: Cambridge University Press, 1998.

[67] W. Humphrey, A. Dalke, and K. Schulten, "VMD: Visual molecular dynamics," *Journal of Molecular Graphics*, vol. 14, no. 1, pp. 33 – 38, 1996.